Electrospun fibers for high performance anodes in microbial fuel cells: optimizing materials and architecture

Dissertation

Zur

Erlangung des Doktorgrades der Naturwissenschaften

(Dr. rer. nat)

dem Fachbereich Chemie

der Philipps-Universität Marburg

Vorgelegt von

Shuiliang Chen

aus Jiangxi V. R. China

Marburg/Lahn

April 2010

der Philipps-Universität Marburg als disertation am

angenommen.

Erstgutachter Prof. Dr. Andreas Greiner

Zweitgutachter PD Dr. Seema Agarwal

Tag der mündlichen Prüfung am

To my wife Cuiyun Zeng and my lovely son Yu Chen, for their love and support

Outline

List of symbols and abbreviations

ATP	adenosine triphosphate
BOD	biological oxygen demand
C_N, C_T	Concentration of Nomex® and TPU solution
2D-ECFM	two-dimensional electrospun carbon fiber mat
3D-ECFM	three-dimensional electrospun carbon fiber mat
DET	direct electron transfer
DMA	dynamic mechanical analysis
DMAc	N,N,- dimethylacetamide
DMF	N,N,-dimethylformamide
DMSO	dimethylsulfoxide
E’	storage modulus
E’’	loss modulus
E.coli	*Escherichia coli*
EDX	Energy Dispersive X-ray analysis
EM	emeraldine (an oxidized state of polyaniline)
E_{emf}	electromotive force potential
E_{an}	potential of anode
E_{cat}	potential of cathode
F	Faraday’s constant
FTIR	fourier transformation infrared spectroscopy
GE-spinning	gas-assisted electrospinning
GF	graphite felt
LBL	layer-by-layer
m	mass of sample
MB	methylene blue
MET	mediated electron transfer
MFCs	microbial fuel cells
MECs	microbial electrolysis cells
M_w	weight average molecular weight
nanoPANi	nanostructured polyaniline
NC	natural cellulose
Nomex®	poly(m-phenylene isophthalamide)
[η]	intrinsic viscosity
OCV	open circuit voltage
OD	optical density
OPM	optical microscope
PA	polyamide
PAN	polyacrylonitrile
PANIB	poly(acrylonitrile-co-itaconic acid-co-butyl acrylate)
PANi	polyaniline

PI	porous index $(\frac{V_T}{V_S}$ or $\frac{\delta_T}{\delta_S})$
PLA	polylactide
PSA	polysulfonamide
PCNM	porous conducting nanofiber mat
ρ	material density
ρ_T	total or bulk density of fiber mat
ρ_a	average material density
φ_N and φ_T	weight percent of Nomex® and TPU
R	gas constant (8.314472 $J \cdot K^{-1} \cdot mol^{-1}$)
RVC	reticulated vitreous carbon
SEM	scanning electron microscope
SHE	standard hydrogen electrode
SMFCs	sediment microbial fuel cells
T	temperature
tanδ	loss tangent
TEM	transmission electron microscope
T_g	glass transition temperature
TGA	thermogravimetric analysis
THF	tetrahydrofuran
TPU	thermoplastic elastomer polyurethane
TSB	Tryptic Soy Broth substrate
wt%	weight percentage
XRD	X-ray diffraction
V_S	solid volume fiber mat
V_V	void-space volume
V_T	total volume of fiber mat
S	surface area
δ_m or δ_T	measured or total thickness
δ_C or δ_S	calculated or solid thickness
σ	electrical conductivity
ε	electrical resistivity
ϕ	porosity

1. Introduction and aim of this work

Microbial fuel cells (MFCs) are a promising technology for conversion of energy from organic matter to electricity. [3, 8, 9] The versatility of microbial catalysis (metabolism) allows direct use of organic compounds from natural hydrocarbons to domestic and industrial wastes as the anode fuel. However, the lower current density and poor long-term stability limits some of its practical applications. A number of factors can affect a MFC performance, [10] such as anode, [1, 11] cathode, [12-14] membrane, [15] inoculum species, [16, 17] environmental parameters and so on. Among these factors, the performance of the anode which is related to microorganisms growth plays a crucial role on the performance of MFC. The requirements for the high performance anode are 1) high conductivity for easy electron transfer, 2) high specific surface area (area per gram) for growth of as many microorganisms as possible, 3) high porosity and large pore size for easy mass transfer and microorganism passing through, 4) inexpensive and easy to make in large scale production.

The electrospinning technique, a fascinating technology of producing fibers with diameter ranging from several nanometers to several micrometers,[5] attracted more and more attentions in the past few years. The electrospun fiber mat with its various advantages like being easy to make, controllable fiber diameter in a wide range, high specific surface area, controllable porosity and pore size, has shown a number of applications in many fields. [5, 18-20]

Not only the high specific surface area, but also the extremely high porosity is the key to anodic performance in MFCs. The porosity, which describes the fraction of void space in the material, is of utmost importance, since it not only lowers the amount of material to a minimum but also maximizes the penetration of the material by the microorganisms and the diffusional substrate supply. So, the aim of this work is the preparation of a high efficiency anode with high specific surface area and high porosity for MFCs by electrospinning.

The work consists of three parts:

The first part is the preparation of porous conducting nanofiber mats (PCNMs) with nanostructured polyaniline (nanoPANi) on the fiber surface. In this part, PCNMs are prepared by growth of nanoPANi on electrospun polyamide (PA) nanofibers. This PA/PANi composite nanofiber mat is found to exhibit excellent properties, but its conductivity too low for an application as anode in MFCs.

The second part consists of the preparation of three-dimensional (3D) electrospun carbon fiber mat that could serve as anode in microbial fuel cells (MFCs). Two kinds of 3D carbon fiber mats are prepared by electrospinning and subsequent carbonization. The first one is prepared by gas-assisted electrospinning (GE-spinning); the second one is prepared by layer-by-layer electrospinning (LBL- electrospinning). These two 3D carbon fiber mats are used as anodes in MFCs and their electricity generation properties are investigated. The results display that both 3D carbon fiber mats show good anodic performance in MFCs.

The third part is about anode architecture design for MFCs. Nanosprings, which is a novel three-dimensional (3D) anode structure, is processed by bi-component electrospinning for MFCs. The spring-shaped nanofibers are successfully produced by bi-component electrospinning. Three kinds of bi-component electrospinning techniques, coaxial electrospinning, off-centered electrospinning and side-by-side electrospinning, are used to produce spring-shaped nanofibers. The nanospring structure makes the nanofiber mat much more porous, and will be a potential architecture for anode in MFCs.

2. Introduction

2.1 Background of microbial fuel cells

The global energy crisis and climate problem are being aggravated in recent years due to the increasing demand of fossil fuels, especially oil, coal, and natural gas. Renewable bioenergy is viewed as one of the ways to alleviate these problems. Major effort is devoted to develop alternative electricity production methods. New electricity production from renewable resources without net carbon dioxide emission is much desired. Microbial fuel cells (MFCs) as one renewable bioenergy resource for the conversion of energy from organic matter to electricity [3, 8, 9] attracts more and more attentions.

2.1.1 Definition of MFCs

Since 1911, with the discovery of an electromotoric force between electrodes immersed in bacterial or yeast cultures and in sterile medium in a battery type setup, [21] MFCs have generated considerable interest in academic research in recent years. [3, 22, 23] A MFC is an electrochemical device that uses microorganisms to oxidize organic matter and generate electricity. [3, 6, 24] It consists of anode, cathode and a membrane through which protons are allowed to pass through. A schematic diagram of an MFC system is shown in **Fig 2.1.1.1**. In the anode, microorganisms oxidize (degrade) small organic molecules, such as monosaccharide, acetate derivatives, alcohols and others, produce electrons that travel through a series of respiratory enzymes in the cell and make energy in the form of adenosine triphosphate (ATP), and release protons, as well as carbon dioxide. The electrons then transfer from inside of microorganisms to the anode and flow through the outer circuit to the cathode, and the protons go through the membrane to the cathode. In the cathode, the electrons are released to a terminal electron acceptor which accepts electrons and becomes reduced. A great number of chemicals can serve as electron acceptors, such as oxygen, nitrate, sulfate and so on.

Using acetate as an example substrate and oxygen as electron acceptor, the reactions of MFCs are:

In the anode:

$$2HCO_3^- + 9H^+ + 8e^- \rightarrow CH_3COO^- + 4H_2O \quad (1)$$

In the cathode:

$$O_2 + 4H^+ + 4e^- \rightarrow 2H_2O \quad (2)$$

MFCs are a kind of green energy source, because most fuels for the MFC can be derived from photosynthesis of plants. Plants absorb carbon dioxide and convert the solar energy into bioenergy (chemical energy) by photosynthesis. While in MFC, the bioenergy is converted into electricity and carbon dioxide is released. There is no net release of carbon dioxide during the carbon circle.

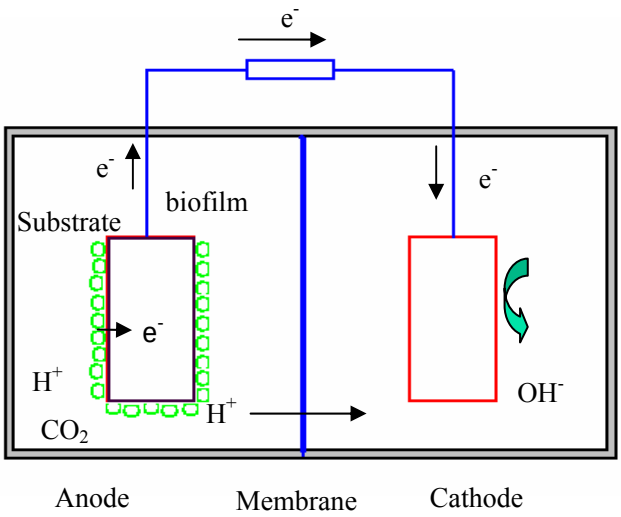

Fig 2.1.1.1 Schematic diagram of the basic components of a microbial fuel cell

2.1.2 Fundamentals of voltage generation in MFCs

Similar to most fuel cells, for calculations voltage generation in MFCs, it is more convenient to evaluate the reaction in terms of the overall cell electromotive electric force (emf), E_{emf} (V), defined as the potential difference between the cathode and anode. [2, 24]

$$E_{emf} = E_{emf}^0 - \frac{RT}{nF}\ln(\Pi) \quad (3)$$

Where E^0_{emf} is the standard cell electromotive force, n is the number of electron per mol reaction, F is the Faraday's constant (9.64853×10^4 C·mol^{-1}). The reactions occurring in the MFCs can be analyzed in terms of the half cell reactions, or as separate reactions occurring at the anode and the cathode. According to the IUPAC convention, standard potentials (at 298 K, 1 bar, 1 M) are reported as a reduction potential, i.e., the reaction is written as consuming electrons. Using acetate as example substrate, its oxidation in the anode by microorganisms can be written by Eq. (1). The standard potentials are reported relative to the normal hydrogen electrode (NHE), which has a potential of zero at standard conditions (298 K, pH_2 1 bar, [H^+] 1 M). To obtain the theoretical anode potential, E_{An}, under specific conditions, we use Eq. (3), with the activities of the different species assumed to be equal to their concentrations. For acetate oxidation, we therefore have

$$E_{An} = E^0_{An} - \frac{RT}{8F}\ln\left(\frac{\left[CH_3COO^-\right]}{\left[HCO_3^-\right]^2\left[H^+\right]^9}\right) \tag{4}$$

For the theoretical cathode potential, E_{cat}, if we consider the case where oxygen is used as the electron acceptor for the reaction, as written by Eq. (2).

So

$$E_{Cat} = E^0_{Cat} - \frac{RT}{4F}\ln\left(\frac{1}{pO_2\left[H^+\right]^4}\right) \tag{5}$$

A variety of catholytes have been used, and for each of these the cell voltage varies. For example, manganese oxide [25] and ferricyanide [11] have been used as alternatives to oxygen. The pH of the cathode solution can also vary, affecting the overall cathode potential. Using Eq. (5) and tabulated standard potentials available for inorganic compounds under several different conditions, as shown in **Table 2.1.1**, it can be seen that the theoretical cathode potential for these different catholytes range from 0.361 to 0.805 V. The cell E_{emf} is calculated as

$$E_{emf} = E_{cat} - E_{an} \tag{6}$$

where the minus sign is a result of the definition of the anode potential as reduction

reaction (although an oxidation reaction is occurring). It should be noted that the result using Eq. (6) equals that of Eq. (3) only if the pH at the anode and the cathode are equal. Eq. (6) demonstrates that using the same anode in a system with different cathode conditions as listed in **Table 2.1.1** would produce significantly different cell voltages, and thus different levels of power output. The power produced by an MFC therefore depends on the choice of the cathode, and this should be taken into account when comparing power densities achieved by different MFCs.

Table 2.1.1 Standard potential of redox couples in biology [6]

Redox couples [3, 6, 7]	Standard potential (V) *
$HCO_3^- + H^+ + e^- \rightarrow (formate) HCOO^- + H_2O$	-0.43
$C_6H_{12}O_6 + 6H_2O \rightarrow 6C\,O_2 + 24H^+ + 24e^-$	-0.43
$2H^+ + 2e^- \rightarrow H_2$	-0.42
ferredoxin $(Fe^{3+}) + e^- \rightarrow$ ferredoxin(Fe^{2+})	-0.42
$NAD(P)^+ + H^+ + 2e^- \rightarrow NAD(P)H$	-0.32
$S + 2H^+ + 2e^- \rightarrow H_2S$	-0.274
$CH_3CHO + e^- \rightarrow CH_3CH_2OH$	-0.197
$2HCO_3^- + 9H^+ + 8e^- \rightarrow CH_3COO^- + 4H_2O$	0.187
$Fe(CN)_6^{3-} + e^- \rightarrow Fe(CN)_6^{4-}$	0.361
$NO_3^- + 2H^+ + 2e^- \rightarrow NO_2^- + H_2O$	0.421
$MnO_2 + 4H^+ + 2e^- \rightarrow Mn^{2+} + 2H_2O$	0.695
$Fe^{3+} + e^- \rightarrow Fe^{2+}$	0.771
$O_2 + 4H^+ + 4e^- \rightarrow 2H_2O$	0.815

* the redox potential at pH=7.0

The cell E_{emf} is a thermodynamic value that does not take into account internal losses. The open circuit voltage (OCV) is the cell voltage that can be measured after some time in the absence of current. Theoretically, OCV should approach the cell E_{emf}. In practice, however, OCV is substantially lower than the cell E_{emf}, due to various potential losses. For example, a typical measured potential of a cathode using oxygen at pH=7 is about 0.2 V. This is clearly lower than the expected value of 0.805 V, indicates that the large energy loss occurs at the cathode. This energy loss is often referred to as overpotential, or the differences between the potential under equilibrium conditions and the actual potential, which for this case is 0.605 V (0.805 V-0.2 V). This illustrates that the main application of thermodynamic calculations is to identify the size and nature of energy losses.

2.1.3 History of MFCs development

The earliest MFC concept was demonstrated by Potter in 1910, who detected electromotive force in living cultures of *Escherichia coli* or *Saccharomyces* by using platinum electrodes, [21] and he concluded that the electric energy can be liberated from the metabolism of microbes. But, this didn't attract much interest due to the extremely low voltage and current. It was not until the 1980s when H. Peter Nenetto discovered that current density and the power output could be greatly enhanced by the aid of artificial electron mediators. [26-29] Then MFCs were able to produce electricity at a consistent rate. But the toxicity and instability of synthetic mediators limited their applications in MFCs. The latest and most remarkable research on MFCs began at the end of 20th century, which was driven by the growing awareness of crisis of energy and environment and necessity to develop technology for a sustainable handling of our environment and resource on Earth. MFCs as one of potential sustainable energy source started to arouse extensive attention. It was found by Lovley et al. that some microbes can use naturally occurring compounds including microbial metabolites (Endogenous mediators) as mediators. Humic acids, anthraquinone, the oxyanions of sulphur (sulphate and thiosulphate) all have the ability to play the role of mediators and transfer electrons from inside the cell membrane to the anode. [30, 31] A real breakthrough was made when some microbes were found to transfer electrons directly to the anode,[32, 33] such as *Shewanella putrefaciens*, [34] *Geobacteraceae sulferreducens*, [35] *Geobacter metallireducens*, [36] *Rhodoferax ferrireducens* [33] and so on. They are all bioelectrochemically active and able to form a stable biofilm on the anode surface and transfer electrons directly by conductance through the membranes or nanowires. These microbes are rich in the environment, e.g. in wastewater, and operationally stable and can yield high Coulombic efficiency [33, 37] and high current density [23, 34, 38]. Furthermore, researchers have focused on understanding the electron transfer process from microorganism to the electrode. [1, 35, 39-41] The rapid development of MFCs is reflected by the sky rocketing numbers of scientific publications and patents, and also the power density increases over four

orders of magnitude, as shown in **Fig 2.1.3.1**.

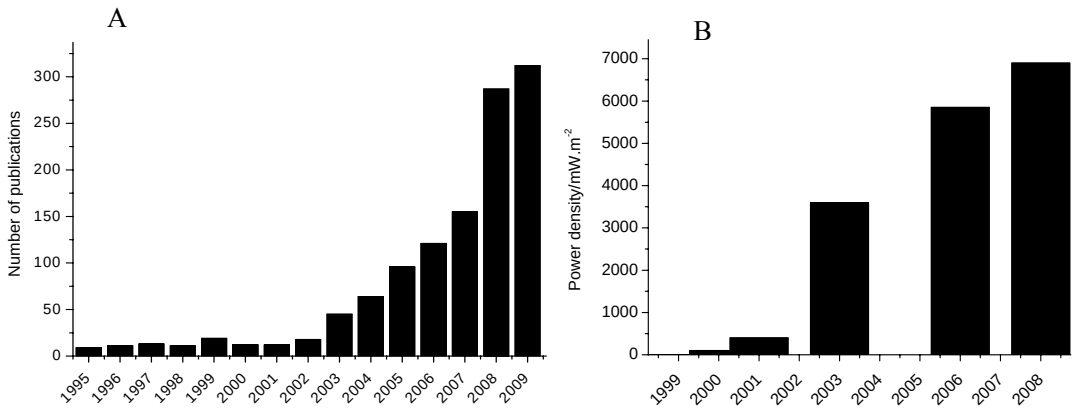

Fig 2.1.3.1 A) Number (n) of scientific publications and patents per year (1995–2009) combined the searching results with the keyword "microbial fuel cell" and "microbial fuel cells" (source: SciFinder Scholar) B) Energy output of MFCs in the past ten years [1, 3, 4]

2.1.4 Electron transfer ways in MFCs

How do the electrons transfer from inside of microorganism to the anode of MFCs? Different mechanisms and concepts of electrons ways have been proposed, [1, 6, 24] which mainly include the following three ways.

2.1.4.1 Direct electron transfer

The direct electron transfer (DET) way is that in which the electrons are transferred to the anode of MFCs via physical contact of electrically conducting outer membrane cytochromes or membrane organelle such as nanowires (pili) (**Fig 2.1.4.1a, b**). [41] In the outer membrane contact, such as cytochromes, in which only the microorganisms in the first monolayer at the anode surface are electrochemically active, which limit the MFC performance and lead to very low current density, i.e., lower than 6.5μA·cm^{-2}. [33-35] Some bacterial species, such as *Geobacter, Rhodoferax*, *Shewanella*, can evolve electrically conducting nanowires that can reach and utilize the solid electron acceptors at more distant. [41] The formation of such nanowires may allow growth of thicker electrochemically active biofilms and thus lead to ten-fold higher

anodic performances. [42]

2.1.4.2 Mediated electron transfer

The mediated electron transfer (MET) way is that in which the electrons are transferred by electron shuttles (mediators), including artificial and self-produced mediators (metabolites). The mediators accept the electrons and get reduced inside the bacteria, and then are moved outside and give electrons to the anode and get oxidized, see in **Fig 2.1.4.1c**. A large number of compounds, the majority being based on phenazines, phenothiazines, phenoxazines and quinines, have been investigated as mediators in MFCs. [26, 28, 43-45] They are normally soluble in water and with conjugated structure and low redox potential (reversible). [46] The mediators can be artificial redox mediators or secondary metabolites. The greatest disadvantage of the use of artificial redox mediators is, beside the usually low current densities (10–100 $\mu A \cdot cm^{-2}$), that there is a necessity of regular addition of the exogenous compound, which is technologically unfeasible and environmentally questionable. The secondary metabolites are synthesized by the microorganism themselves during metabolism. [47] The production of small amounts of these compounds which directly stay in the anodic biofilms and enable transfer of electrons at efficiently high rate, especially in batch model. [48, 49]

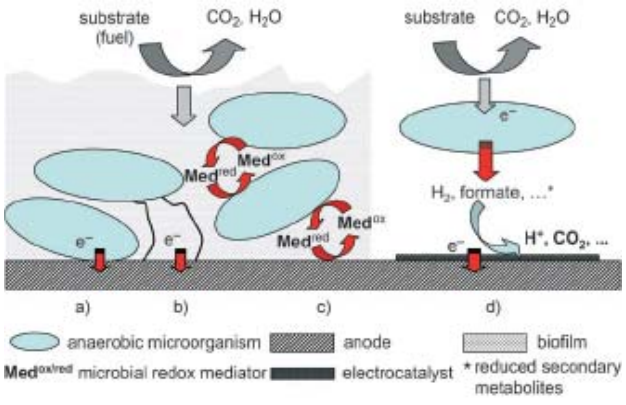

Fig 2.1.4.1 Electron transfer ways in MFCs. Electron transfer via a) cell-membrane-bound cytochromes, b) electrically conductive pili (nanowires), c) microbial redox mediators, and d) oxidation of fermentation products [1, 2]

2.1.4.3 Direct oxidation of fermentative product

A large variety of fermentative and photo-heterotrophic processes result in the production of energy-rich reduced metabolites such as hydrogen, ethanol or formate or others, which are shown in **Fig 2.1.4.1d**. These compounds can be oxidized directly in the microbial medium and generate electrons in the presence of catalysts, such as platinum, [11, 50] tungsten carbide [1] which produce very high current density of 1.5 $mA \cdot cm^{-2}$ and 3 $mA \cdot cm^{-2}$, respectively. Complex natural products, such as starch [51] and cellulose [52] can be split into small organic molecules by fermentation for electricity generation in MFCs.

There are no satisfactory answers on which electron transfer way is the best for higher electricity generation. Much efforts now are being put on to improve the performance of the anode by enriching of mixed cultures in which combination and interaction of different electron transfer mechanisms occur, [53] for example, for wastewater treatment. Because, a multiple of microorganisms that exist in wastewater [54] can be directly used for production of electricity.

2.1.5 Potential applications for MFCs

2.1.5.1 Wastewater treatment

There is plenty of organic matter contained in the wastewater. The traditional wastewater treatment way is the use of microorganisms to degrade and break up the organic matter into carbon dioxide and release energy into the environment in the form of heat. The most popular methods for traditional wastewater treatment are activated sludge and biofilm. Both methods need sufficient aeration to facilitate the break-down of organic matter, because the major electron acceptor for the metabolism of microorganisms is oxygen. The aeration needs a huge amount of electric energy. When MFCs are applied to wastewater treatment, the microorganisms consume the waste organic matter and release electrons to the anode, the electrons flow out to the air cathode. So, the use of MFC for removal of waste organic matter does not need

aeration, it not only saves energy to power the aeration, but also transfers waste energy into electricity. Several MFCs designs, such as continuous flow, single-compartment and membrane-less, have been reported for concerning of scale-up wastewater treatment. [55, 56] The sanitary waste, food processing waste water and swine wastewater all are suitable for MFCs due to their richness in organic matter. [36, 57-59] Up to 80% of chemical oxygen demand (COD) can be removed in some cases [36, 57] and a Coulombic efficiency as high as 80% [60] has been reported .

2.1.5.2 Microbial electrolysis for hydrogen production

MFCs can be readily modified to microbial electrolysis cells (MECs) which produce hydrogen. [53, 61, 62] Traditionally, hydrogen is produced by electrolysis of water. This includes two steps, a) separation of the proton and oxygen and b) removal of oxygen from the anode. Both steps are thermodynamically unfavorable and need an external potential of 1210 mV, theoretically, [53] at neutral pH of 7. In MFCs, in contrast, the organic matter is split into protons and carbon dioxide by microorganisms in the anode. This process is thermodynamically favorable, and enables to approach a potential of -300mV. A potential of -414mV is needed to remove hydrogen from the cathode. So the cell voltage for a system that could produce hydrogen at the cathode is 114 mV [$E = E_{Cat} - E_{An} = (-414) - (-300) = -114$ mV], much lower than 1210 mV for electrolysis of water. Moreover, the hydrogen production in MECs, oxygen is no longer needed in the cathodic chamber, and the effect of oxygen leak on the MFCs performance is eliminated

2.1.5.3 Conversion of bioenergy from biomass into electricity

Thousands and thousands of tons of biomass are produced each year on the earth in the form of by-products of crops such as rice and wheat straws, waste from animals and so on. MFCs are able to convert the bioenergy stored in biomass into electricity with the aid of microorganisms. The biomass is firstly broken up into monosaccharide and other small organic molecules by fermentation, then they can serve as fuels in

MFCs and get converted into electricity. The theoretical conversion efficiency can be achieved to over 70% like conventional fuel cells. High electron recovery of 80% [33] and 89% [63] have been reported. An extremely high Coulombic efficiency of 97% has been reported during oxidation of formate with catalysis of Pt black. [64]

2.1.5.4 Biosensor

MFCs technology is also used as sensor for pollution analysis and *in situ* process monitoring and control which was reported by Chang et al. [65, 66] The proportional correlation between the Coulombic yield of MFCs and the strength of the wastewater makes MFCs are possible for biological oxygen demand (BOD) sensors. [65, 67, 68] MFC-type of BOD sensors are superior to other types of BOD sensors due to their excellent operational stability, good reproducibility and accuracy, and they can be kept operational for over five years without maintenance. [67]

2.1.5.5 Bioremediation

In an MFC, the microorganisms donate electrons to the anode using mediators or nanowires, but it can also be reversible, i.e., the microorganisms can accept electrons form the electrode. This is the basis of biocathode, in which a biofilm catalyzes the reduction of oxygen and improves the performance of cathode. [13, 69] This biocathode is capable of in-situ bioremediation to reduce nitrate or Uranium (VI) and be removed from water. [70, 71]

2.1.5.6 Sediment MFC for remote power

In sediment MFC (SMFC), the anode is placed into the anaerobic sediment and the cathode is placed into the overlying water containing dissolved oxygen. SMFC can be used as power source for devices that are operated in under-water environment. [72, 73]

2.2 Background of electrospinning

Electrospinning is an effective and fascinating method for the preparation of continuous ultra-thin fibers with diameter ranging from several micrometers to several nanometers. [5, 74] So far, submicro- and nano-scaled polymer fibers have been electrospun from a wide range of polymers, including conventional polymers, biocompatible and biodegradable polymers, proteins, peptides, which have been presented in reviews. [5, 75-77] Also, it is possible to incorporate carbon nanotubes, [78-80] electronic, magnetic, optical, biological materials, even bacteria [81, 82] and virus [81, 83] into the polymer matrix to obtain multifunctional nanofibers. Various modified electrospinning techniques for special fibers or tubes have been reported in the literature, such as silk, [84, 85] carbon/graphite, ceramic, [86] metal [87] or other inorganic [88] nanofibers, and polymer, carbon/graphite [89] and ceramic [90] hollow nanofibers. Also, diverse nanofiber assembling techniques have been reported to fabricate electrospun nanofibers with manifold shapes and orientations for a variety of applications, such as continuous nanofiber yarn, [78, 91-93] uniaxial aligned nanofiber mats [94-97] of belts, [98] aligned array nanofiber mats, [99-101] nanofiber conduit [102, 103] and so on.

The electrospun fibers can be applied to a wide range of field, which have been summarized in a large number of reviews, [5, 18, 19, 77, 104, 105] such as electrospun polymer nanofibers for high efficient air and liquid filtrations, [106-108] electrospun metal and metal oxide nanofibers for application in solar cells,[109-111] electrospun carbon nanofibers for electrode of fuel cells [112] and batteries [113-115], for supercapacitors [116-119] and hydrogen storage, [120, 121] electrospun biopolymer and degradable polymer nanofibers for applications in tissue engineering [122-125]and drug release [126-130] and many others.

2.2.1 Electrospinning techniques

Electrospinning can be defined as spinning in an electrostatic field, which is an

effective technique of producing continuous polymer ultra-thin fibers. [5] The setup for electrospinning is shown in **Fig 2.2.1**. In this technique, a polymer solution or melt is passed through a spinneret and a collector is placed opposite to the spinneret. A potential (in kV) is applied between the spinneret and a collector; both are electrically conducting and separated by an optimum distance. The interactions of the electrical charges in the polymer fluid with the external electric field causes the pendant droplet to deform into a conical structure called the "Taylor cone" and a critical voltage is attained. When the applied voltage surpasses the critical value at which repulsive electrostatic forces overcome the surface tension, a fine charged jet is ejected from the tip of the Taylor cone. These charged jets undergo a whipping motion and elongate continuously via electrostatic repulsion until they are deposited onto a grounded collector; resulting in the formation of fine fibers. [131] Instability can occur if the applied external electrostatic field is not above the critical value, which would cause the jet to break up into droplets. [132, 133] Such phenomenon is called Rayleigh instability. Therefore, the formation of nanofibers is a function of operating parameters like applied voltage, solution feeding rate and solution properties such like conductivity, viscosity and surface tension. Consequently, these electrospinning process parameters can be tuned to produce a wide range of fiber diameters.

By modifying the single spinneret design, different electrospinning speed can be obtained and different properties can be introduced to the nanofibers. Modifying the single spinneret with number of channels/capillaries, it leads to bi-component and triple or multi-component electrospinning. For bi-component electrospinning, controlling the location of two channels/capillaries with coaxial and side-by-side way then resulted in coaxial and side-by-side electrospun fibers. Moreover, coaxial electrospinning becomes gas-jacketed/assisted electrospinning after replacing one polymer solution by gas in the outer tube. Also multi-jet and needle-less electrospinning are designed for mass production of electrospun nanofibers. Summaries of electrospinning designs are shown in **table 2.2.1** and **table 2.2.2**

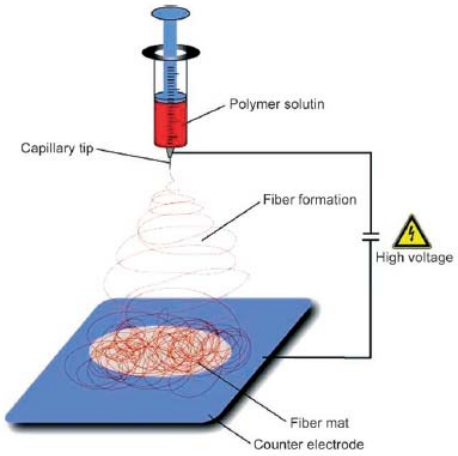

Fig 2.2.1 Schematic diagram of setup for electrospinning [5]

2.2.2 Double channel electrospinning

2.2.2.1 Coaxial electrospinning

The most popular bi-component electrospinning is coaxial electrospinning. In coaxial electrospinning, two polymer solutions are delivered through a spinneret which contains two concentrically aligned channels/capillaries (**table 2.2.1. 2**). The same voltage is applied to both capillaries, and it deforms the compound droplet. A jet is generated on the tip of the deformed droplet. In an ideal case, a nanofiber with core/shell structure is created. It is elucidated by experiments and mathematical modeling that the coaxial electrospinning involves a set of intricate physical processes. [134] During the process of fiber formation, the outer droplet can be transformed into a jet, while the inner droplet can not because there are no surface charges on inner droplet. So the deformation of the inner droplet into the core fiber is left to viscous forces alone. It also has been illustrated by a mathematical model that the formation of core/shell jets and nanofibers via coaxial electrospinning in the considered range of parameters is greatly facilitated when the core tube protrudes outside the shell tube by around 0.5 of its radius. [134]

It has been shown by Yarin et al. that miscible and immiscible solvents, even identical solvents, can be used for an uninterrupted coaxial electrospinning, while in as-pun fibers, the core/shell boundary is sharper when solvents are immiscible. [135] Experiments show that if the appropriate technical parameters are chosen, core/shell fibers can be fabricated with high precision from a wide variety of materials by coaxial electrospinning. Non-spinnable materials such as oligomers, metal salts, enzymes, and liquids can also be immobilized in fibers to make functional nanofibers by coaxial electrospinning. [136]

Coaxial electrospinning is not limited to the production of core/shell fibers with straight core. Systems with buckling, [89] drop-shape inclusions inside a continuous shell can also be generated by controlling the viscosity of core and shell solutions. Turbostatic channels would be formed after removal of the buckling core. This structure provided extremely high confinement volumes and showed potential application for hydrogen storage. The drop-shape core morphology is of interest for inclusion of biological objects, such as for storage and controlled release of drugs.

Coaxial electrospinning shows great function for production of hollow and non-spinnable material nanofibers by selective removal of the core or shell. There are some solutions which can not be electrospun perhaps due to high solution viscosity and high surface tension. In this case, the solution can be extruded through the inner capillary while the spinnable solution is extruded through the outer capillary. During electrospinning, the solution at the shell would carry the inner solution as its core. When the outer polymer is removed, the desired inner nanofiber is retained. Silk, [84, 85] metal, [87] and inorganic nanofibers, [86, 88, 137] can be made by this way.

Using a similar concept, the inner component can be removed instead of the outer polymer after electrospinning which give rise to hollow nanofibers. This has been adapted to make ceramic, [90] titanium dioxide, [138] carbon [89] hollow nanofibers and silica nanochannels. [139]

2.2.2.2 Gas-jacketed/assisted electrospinning

Gas-jacketed/assisted electrospinning is derived from the melt-blowing method which is used to make sub-micro fibers. It can be used to reduce the clogging of the spinneret when volatile solution is used in electrospinning. [140] By making use of coaxial design, the solution is delivered from the inner tube while the outer tube is used to blow a jacket of gas saturated with the corresponding solvent of the solution to be electrospun, as shown in **table 2.2.1. 3**. Morphologies from smooth fibers to beaded fibers or particles can be controlled by the blowing rate without varying the voltage.

Another application of gas-assisted electrospinning is that under the assistance of hot blowing air, the unusually highly viscous hyaluronic acid (HA) solution can be easily electrospun into nanofibers with low voltage. [141, 142] The advantages of hot blowing might be that it 1) decreased the viscosity of solution, 2) enhanced the evaporation of solvent and 3) stretched the jet. The blowing air also can be applied on multi-jets electrospinning for mass production of nanofibers. [76, 143] This part will be described in multi-jets electrospinning section.

2.2.2.3 Side-by-side electrospinning

Similarly, the spinneret can be designed with two capillaries in a side-by-side way as shown in **table 2.2.1. 4**. Bi-component nanofibers with side-by-side structure can be produced by using this design. A possible application for this bi-component fiber is to produce functional composite nanofiber that shows both properties. [144] For example, one of the sides is able to absorb chemicals while the other side is electrically conducting or serve as high strength substrate. Moreover, the different shrinkage of the two sides would cause bending fibers. [145] even helical or spring shape nanofibers. [146]

2.2.3 Triple and multi channel electrospinning

Lallave et al [147] reported a triple electrospinning method for generation of Alcell lignin hollow nanofibers. In this method, a tri-axial configuration design was used, in **table 2.2.1. 5.**, a sheath flow of ethanol to avoid solidification of the Taylor cone, the innermost needle supplies glycerine as a template fluid, the middle tube delivers the lignin solution to form Alcell lignin hollow nanofibers.

A novel bio-mimic multichannel microtube fabricated by a multi-fluidic compound jet electrospinning technique was reported by Zhao et al, [148] **table 2.2.1. 6.** The microtubes with two to five channels were produced successfully. It is a promising candidate for a wide range of applications, such as for bio-mimic super lightweight thermoinsulated textiles, vessels for macro/nanofluidic devices, multi component drug delivery and high efficient catalysts.

2.2.4 Multi-jet electrospinning for mass production of nanofibers

2.2.4.1 Multiple needles electrospinning

A well known limitation of the electrospinning process is the level of fiber production, which is much lower than that of current fiber spinning technology. A straightforward method of increasing the productivity of electrospinning is by increasing the number of spinnerets used in the process, [149] see in **table 2.2.2. 1**. However, the presence of nearby spinnerets has an undesirable influence on the electrospinning jets. The distribution of the fiber diameter may be very wide as a result of the fluctuation of the electric field between the spinnerets and the collector. Moreover, the rapid evaporation of solvents would cause the clogging of the needles during electrospinning. These two disadvantages blocked the mass production of electrospun nanofibers by only increasing the number of needles.

2.2.4.2 Multiple spikes upward electrospinning

To eliminate the problem with clogging of the needles during multiple needles electrospinning, Yarin et al [150] devised a setup that used spikes to facilitate the spinning process rather than the extrusion of solution through needles, (**table 2.2.2. 3)**. Magnetic fluids were prepared using magnetite powder in silicone oil. Under the influence of a magnetic field, numerous spikes were formed on the free surface of magnetic fluids. A polymer solution was carefully added on the surface of magnetic fluids and formed a layer. An electrode was submerged in the polymer solution and high voltage was applied. When a grounded piece of metal was used as counter electrode, thousands of jets erupted from the surface of solution and the fibers were deposited on to the metal saw. [150]

2.2.4.3 Porous electrospinning

Dosunmu et al [151] demonstrated an innovative method of using a porous tube to significantly increase the electrospinning rate, as shown in **table 2.2.2. 2**. The polymer solution was first placed into the porous cylindrical tube where an electrode was inserted into. By applying air pressure, the solution was forced through the numerous pores in the tube. An electrode was used to charge the solution such that as the solution approached the outer surface of the tube spinning of numerous jets generated and the fibers were deposited on the inner surface cylindrical collector that enclosed the porous cylindrical tube. [151]

2.2.4.4 Blowing-assisted multi-jet electrospinning

A blowing-assisted multi-jet electrospinning (multi-jet electro-blowing) apparatus was developed by Stonybrook Technology and Applied Research (STAR). [76] The prototype of the device contained a spinneret assembled with a linear density of 25 spinnerets per inch which was the most critical part. The spinneret was made of high-strength steel, as shown in **table 2.2.2. 4**. The diameter of each spinneret hole

was approximately 0.35 mm. The compressed air was introduced from the side of spinneret block. The polymer solution was introduced into the inlet through a constant-flow pump. The spinneret block and the air knifes were assembled in an enclosure so that the air could be uniformly blown out of the split. The temperature of blowing air can be controlled ranging from room temperature to 150 ℃. This method combined the electric force of high voltage with shearing force of blowing air together and applied on the solution jets to make nanofibers. Three major problems exist: 1) Relatively large fiber diameter (500-1000 nm), 2) yield per spinneret was low, about same as that of single-jet electrospinning, 3) solvent recovery was difficult.

Table 2.2.1 Summary of electrospinning techniques

Electrospinning techniques	Advantage
1. Normal electrospinning 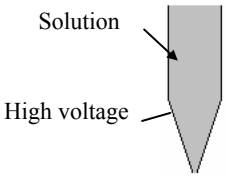	
2. Coaxial electrospinning 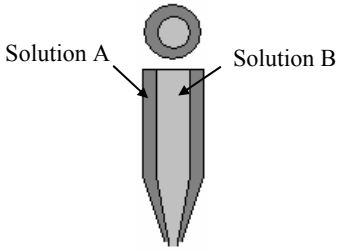	Core/shell nanofiber can be electrospun; [135, 136, 152] Hollow nanofibers can be fabricated by removing core material; [89, 90] Non-electrospun material can be made into nanofibers by using an electrospinnable material [84-86, 88, 137]
3. Gas jacket electrospinning 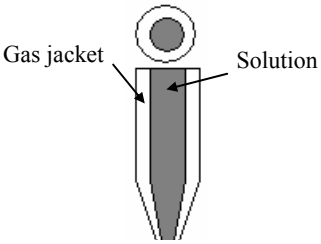	No clogging at the spinneret; The temperature and humidity of gas can be easily controlled; Electrospinning of high viscous solution is possible. [140-142]
4. Side-by-side electrospining 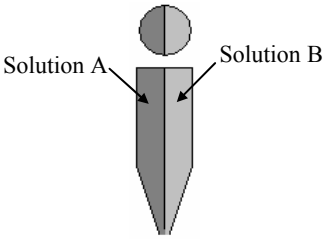	Bi-component nanofibers with side-by-side structure can be produced. [144, 145]
5. Tri-axial electrospinning 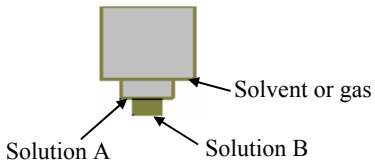	No clogging at the spinneret; Core/shell, hollow and non-electrospun material fibers can be obtained. [147]
6. Multi-channel electrospinning 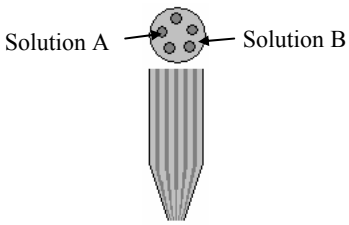	Multi-channel fibers can be fabricated. [153]

Table 2.2.2 Summary of Multi-jet electrospinning for mass production of electrospun fibers

Mass production electrospun techniques	Advantages
1. Multiple spinnerets 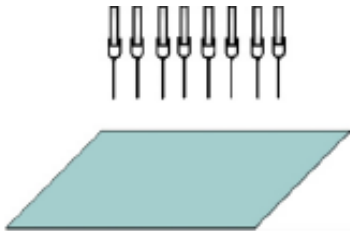	Simple setup; Able to mix fibers of different materials of desired ratio. [149, 154]
2. Porous electrospinning source 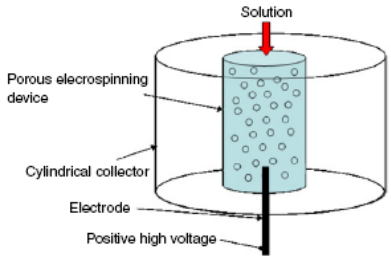	High production of nanofibers. [151]
3. Multiple spikes electrospinning source 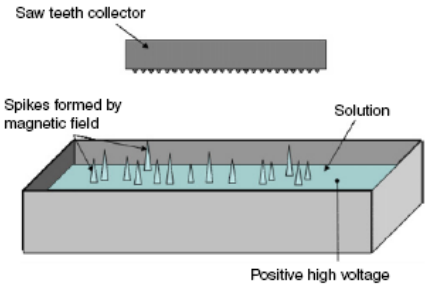	No clogging of solution at source High production of fibers. [150]
4. Gas blown multiple-jet spinneret 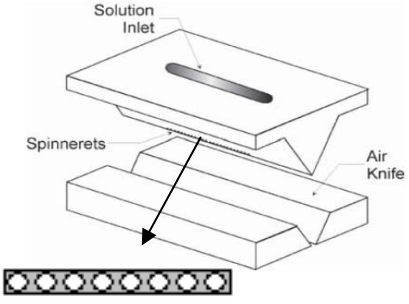	High productivity of fibers No clogging of solution. [76]

3. Conducting porous nanofiber mat with nanostructured fiber surface

Shuiliang Chen, Seema Agarwal, Andreas Greiner, *European Patent* 09153057.6.

Shuiliang Chen, Haoqing Hou, Seema Agarwal, Andreas Greiner*, Preparation of Porous Conducting Electrospun Fiber Mats, *Macromolecules*, 2010, submitted.

Shuiliang Chen, Haoqing Hou, Andreas Greiner, Novel Conductive Biocompatible Electrospun Nanofibers for Application in Microbial Fuel Cells, *Poster in 2009 MRS fall meeting*, Boston, USA.

3.1 Introduction

There is growing interest in the production of porous conducting nanofiber mat (PCNM) for applications, such as electrode in batteries and supercapacitors, [155, 156] sensors, [157, 158] actuators, [159, 160] electrochromic devices, [161] tissue engineering. [162] In this part, PCNMs are prepared that aimed to be used as anode in MFCs. There are several methods reported for preparation of PCNMs, a) directly electrospinning of blends containing high molecular weight polymer and conducting polymer or carbon nanotubes, [162-165] b) adsorption of carbon nanotubes on electrospun nanofibers, [166] and c) vapor phase deposition/polymerization of conducting polymer on electrospun nanofibers. [167] However, the PCNMs prepared by these methods showed disadvantages of low electrical conductivity, low mechanical properties or containing oxidant containment in the fibers, which greatly limited their applications.

In this part, we introduce an extremely simple method to make PCNMs with nanostructured fiber surface. A stable nanostructured polyaniline (nanoPANi) layer is successfully grown on the surface of electrospun polyamide (PA) and forms a core/shell structure by simple chemical oxidative polymerization. The un-reacted chemicals are easily removed by simple water wash. A piece of PCNM sample with nanoPANi surface is shown in **Fig 3.1.1** with a size of 10.5×23 cm^2, the green color of the uniform nanofiber mat demonstrates that the PANi is in the highly conductive

emeraldine salt state.

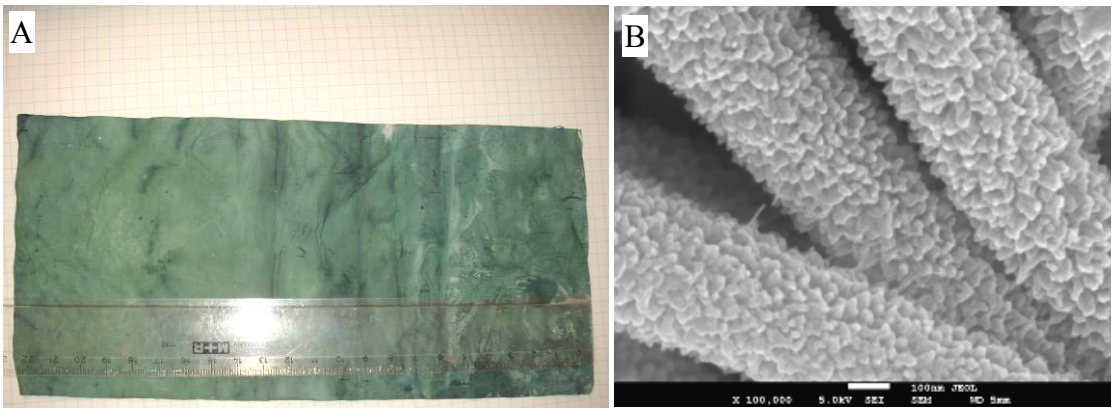

Fig 3.1.1 A) Digital picture of a piece of PA electrospun nanofiber mats grown with nano-fibillar PANi, with size of 10.5×23 cm^2, B) SEM image of composite fibers, scale bar is 100 nm.

It is well known that PANi is unique among the family of conducting polymer, due to the simple way of synthesis, environmental stability and reversible doping/de-doping chemistry. [168] The nanoPANi surface is essential for the applications as electrodes or sensors, due to its high specific surface area. Several approaches have been reported to make nanoPANi, such as chemical oxidative polymerization, including interfacial polymerization, [157] nanofiber seeding, [169] oligomer-assisted polymerization, [170] surfactant-assisted polymerization [171] and non-template polymerization, [172, 173] electrochemical polymerization and electrospinning.

The novel PCNM presented here combines both advantages of electrospun nanofiber mat and nanoPANi, which make the PA/PANi composite nanofibers exhibit more than five excellent properties. The behavior of nanoPANi on electrospun mat and properties of this novel PCNM are investigated systematically, also the feasibility of this PCNM for anode in MFCs is investigated.

3.2 Results and discussion

3.2.1 Growth of nanoPANi on PA electrospun nanofibers by oxidative polymerization

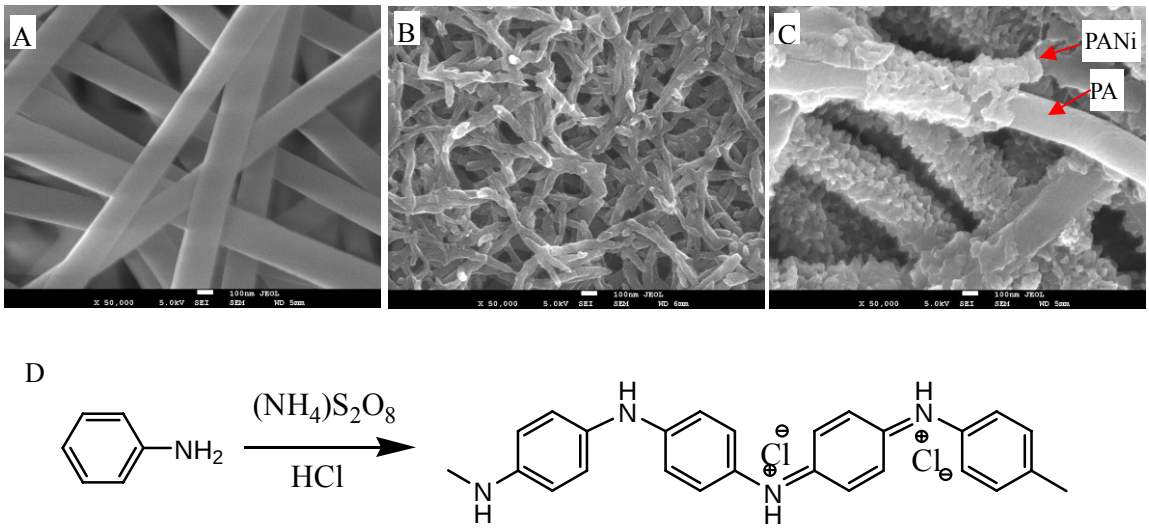

Fig 3.2.1 SEM images of A) PA nanofibers, B) PANi nanofibers, C) PA/PANi core/shell nanofibers with broken shell. Scale bars are 100 nm. D) Reaction equation of oxidative polymerization of aniline

Polyaniline in highly conductive emeraldine salt state (green color) can be obtained easily by simple oxidative polymerization in aqueous solution in the presence of aniline, oxidant and doping acid; [168] the equation of oxidative polymerization of aniline is shown in **Fig 3.2.1D**. Generally, nano-fibrillar PANi with diameter of 35 nm is obtained when the oxidant and aniline solutions are mixed rapidly, as shown in **Fig 3.2.1B**. A piece of electrospun PA nanofiber with white color was put into the mixed solution swiftly. After about 30 min, both the white mat and the solution turned to green color. After further reaction of about 2 h, the green mat was taken out from the solution, washed and dried up, and observed under scanning electron microscope (SEM). It is found from SEM images that the nanoPANi is spontaneously grown on the surface of electrospun PA nanofiber. As shown in **Fig 3.2.1A** the smooth surface of PA nanofibers is uniformly covered by a layer of PANi nanowires and showed

toothed-club morphology, and the pores among the nanofiber mat are still preserved. The SEM image of broken composite nanofiber surface, as shown in **Fig 3.2.1C**, nicely illustrates that the composite nanofibers are core/shell structure.

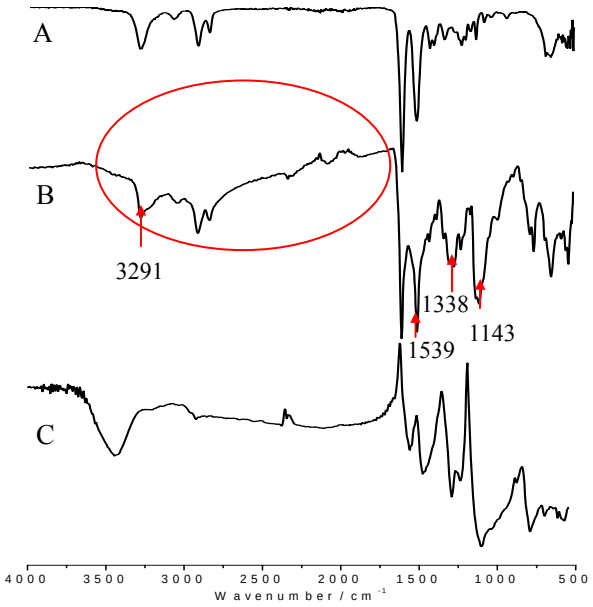

Fig 3.2.2 IR spectra of A) PA nanofibers, B) PA/PANi nanofibers, C) PANi powder (HCl doped)

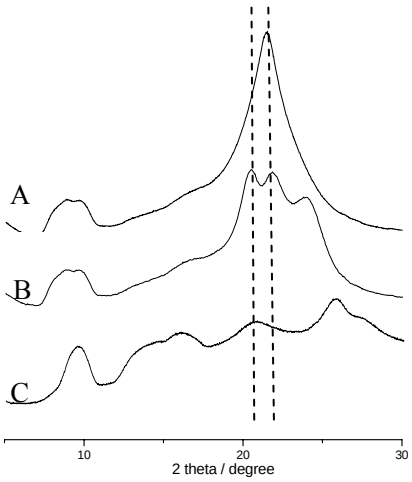

Fig 3.2.3 X-ray diffraction curves of A) PA nanofibers, B) PA/PANi nanofibers, C) PANi powder (HCl doped)

3.2.2 FTIR analysis

Polymerized from the aniline monomer, PANi can be found in different oxidation states. Emeraldine (EM) base is regarded as the most useful form of PANi due to its high stability at room temperature and the fact that upon doping the emeraldine salt form of PANi is highly electrically conducting. The component of composite fiber mat is characterized by fourier transformation infrared spectroscopy (FTIR) analysis. The FTIR spectra of PA nanofibers, PA/PANi PCNM and PANi nanowires are shown in **Fig 3.2.2**. For the FTIR curve of PA/PANi composite PCNM (**Fig 3.2.2B**), the absorption at 3291 cm^{-1} is attributed to the N-H stretch mode, in the case of protonated EM base, it shows broad absorption peak which starts from about 2000

cm^{-1}. While the C=C and C-C stretching and bending mode which relate to the quinonoid unit occur at 1338 and 1307 cm^{-1}, and relate to the benzenoid unit present at 1150 cm^{-1} which have been associated with high electrical conductivity. [168]

3.2.3 XRD analysis

Both the materials of PA and PANi are crystalline polymers, their X-ray diffraction (XRD) spectra are shown in **Fig 3.2.3A, C**, respectively. The XRD pattern of a aligned PA nanofiber belt shows two peaks at 2θ ~9.5 °, 22 °, while the HCl doped PANi power shows four peaks at 2θ ~9.5 °, 15 °, 20.5 ° and 25.7 °, which is consistent with previous report. [174] In the case of PA/PANi composite nanofiber in **Fig 3.2.3B**, four peaks are observed at 2θ ~9.5 °, 20.5 °, 22 ° and 24 °, among them the peak at 20.5 ° is derived from PANi, the peak at 22° is attributed to PA nanofibers, while the peak at 24 ° might be formed by the overlay of the peak at 22 ° of PA aligned nanofibers and the peak at 25.7 ° of PANi. The XRD analysis demonstrates that the composite PCNM is crystalline too.

3.2.4 Control of the morphology and thickness of nanoPANi layers by aniline concentration and temperature

3.2.4.1 Growth of nanoPANi in different concentrations of aniline

The color differences of PCNMs which were prepared in different concentrations of aniline are noteworthy, as shown in **Fig 3.2.4**, the color changes from light green (**a**), green (**b, c**), dark green (**d**), to black (**e, f**). The fiber surface morphology of PA/PANi PCNMs from different aniline concentrations also displays obvious differences, as shown in **Fig 3.2.6**. In low concentration of aniline solution, the nanoPANi wires grown on fibers are relatively long, and lead to a very rough fiber surface (**Fig 3.2.6A, B, C, D**). While in high concentration of aniline, there is a tendency to form short nanoPANi wires which leads to a smooth fiber surface relatively (**Fig 3.2.6E, F**).

Table 3.2.1 Properties of PA/PANi composite nanofibers from different concentration of aniline solution (at temperature of about 20 ℃)

Aniline conc.	Weight percent of PANi / %	Average fiber diameter / nm	Surface area / $m^2 \cdot g^{-1}$
PA nanofibers	0	201	80
0.02 M	2.51	230	132
0.04 M	2.85	288	138
0.08 M	4.1	334	153
0.16 M	8.7	376	160
0.32 M	13.4	419	144
0.64 M	19.11	448	100
PANi nanowires	100	35	61

The properties of PANi/PA PCNMs obtained in different concentration of aniline are summarized in **Table 3.2.1**. The curves of content of PANi and fiber diameter in the PCNMs versus aniline concentration are shown in **Fig 3.2.5a, b**. It can be concluded that, the thickness or content of nanoPANi layer increases with increase of the aniline concentration. The nanoPANi grown on the PA nanofibers shows a very rough fiber surface and lead to high specific surface area. The specific surface area of PCNMs which were derived from solutions with various concentration of aniline is shown in **Fig 3.2.5C**. It increases with an increase of the aniline concentration. This might be caused by increasing amount of nanoPANi on the nanofiber surface. The maximum specific surface area of PCNM is up to 160.08 $m^2 \cdot g^{-1}$, which was obtained in 0.16M aniline solution. This is twice higher than that of pure PA nanofibers (80.2 $m^2.g^{-1}$) and pure PANi powder (60.89 $m^2 \cdot g^{-1}$) consisted by its nanowires. But, further increase of aniline concentration causes the decrease of specific surface area of PCNMs, because the PANi nanowires become shorter (**Fig 3.2.6D, E**). A smooth fiber surface with very thick PANi layer was obtained in high concentration of aniline of 0.64M (**Fig 3.2.6F**).

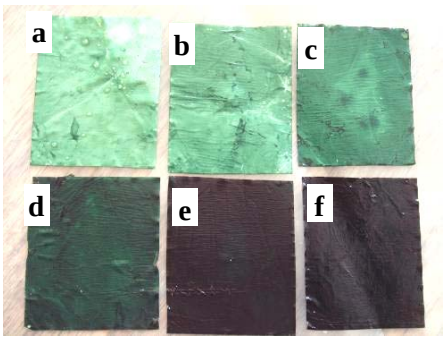

Fig 3.2.4 PA/PANi composite PCNMs from different concentration of aniline, a) 0.02 M, b) 0.04 M, c) 0.08 M, d) 0.16 M, e) 0.32 M and f) 0.64 M.

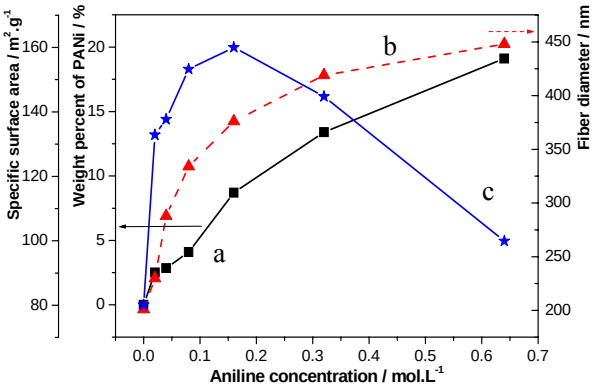

Fig 3.2.5 a) content of PANi, b) fiber diameter, c) specific surface area curves of PA/PANi composite PCNMs vs. concentration of aniline

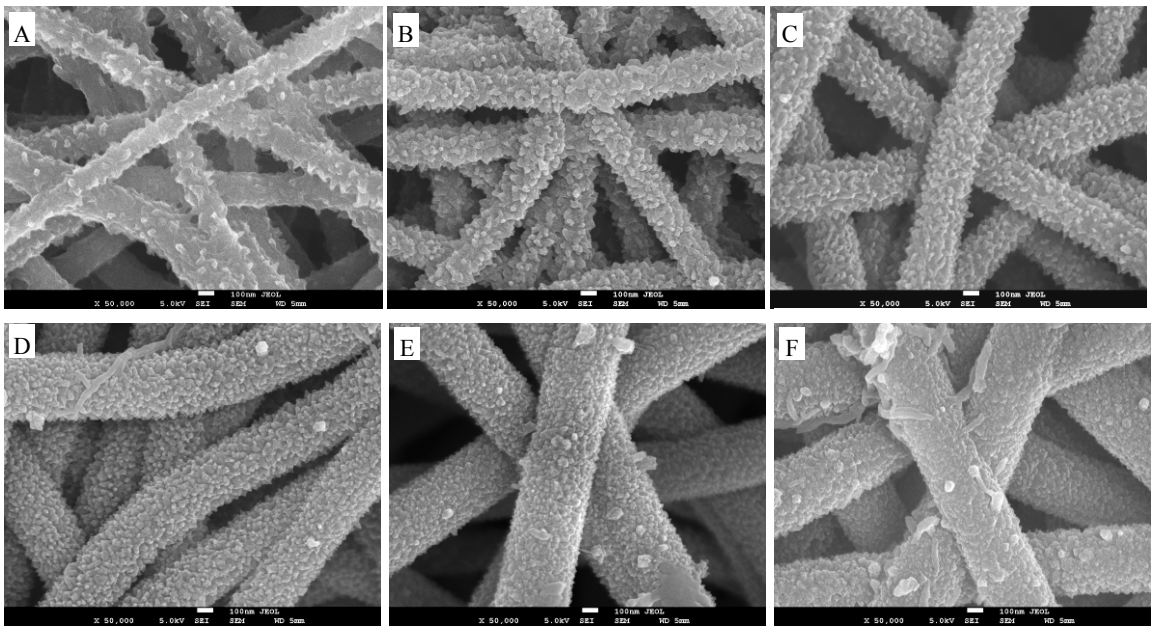

Fig 3.2.6 SEM images of nanoPANi grown on Polyamide nanofibers at different concentration of aniline A) 0.02 M, B) 0.04 M, C) 0.08 M, D) 0.16 M, E) 0.32 M , F) 0.64 M, at room temperature in 1M HCl. Scale bars are 100nm.

3.2.4.2 Growth of nanoPANi at different temperatures

PANi/PA composite PCNMs grown at different temperatures are also investigated systematically. As shown in **Fig 3.2.7**, at low aniline concentration of 0.02 M, at low

temperature (0 °C), a thin layer of PANi with relatively long nanowires is grown on the PA fiber surface (**Fig 3.2.7A**$_1$). The length of the PANi nanowire decreases with raising temperature, while at high temperature of 40 °C, a thin layer of particle-like PANi is grown on the PA fiber surface (**Fig 3.2.7C**$_1$). At high aniline concentration of 0.32 M, at low temperature of 0 °C, a thick PANi layer with very rough surface is grown on the PA nanofiber surface (**Fig 3.2.7A**$_3$), while at high temperature (40 °C), the surface PANi layer become smooth and lots of floating PANi is attached on the fiber surface (**Fig 3.2.7C**$_3$). The content of PANi increases with lowering temperature and increase of aniline concentration, as shown in **Fig 3.2.9**, the highest PANi content in the PCNMs is 17.8 wt%, which is obtained in solution with aniline concentration of 0.32 M at 0 °C.

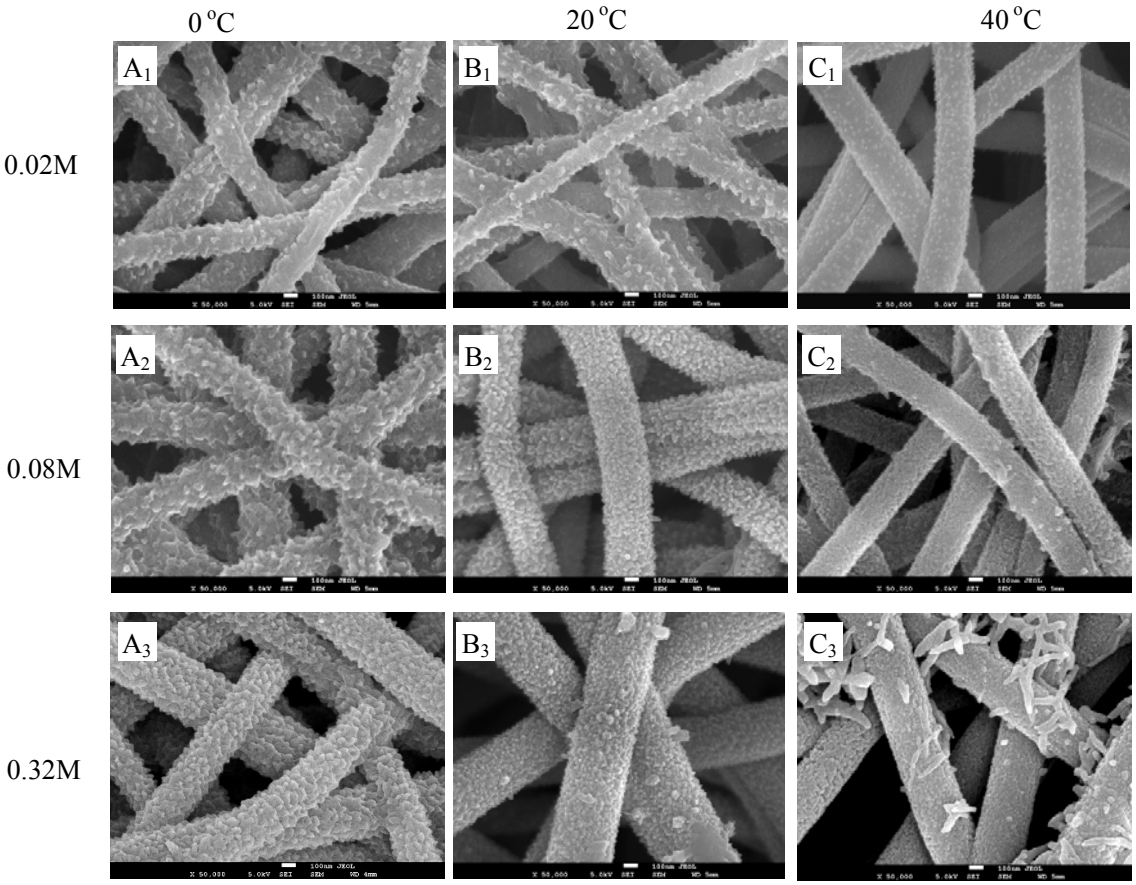

Fig 3.2.7 SEM images of PA/PANi composite PCNMs prepared in different concentration of aniline and at different temperature. Scale bars are 100 nm.

3.2.5 Mechanism of growth of nanoPANi on PA electrospun nanofibers

Previous report showed that the nanoPANi was only able to grow on conducting substrate by electrical polymerization. [175] Later, it was shown that oxidative polymerization of aniline was particularly prone to fibrillar polymer growth in solution. [176-178] The morphology of the resulting PANi was dependent on the experimental steps and concentration of aniline. Nano-fibrillar PANi was obtained when the solutions of oxidant and aniline were mixed rapidly, while granular PANi was obtained when the oxidant was added drop-wise. [176] In dilute aniline solution, it tended to form long PANi nanowires while agglomerative PANi particles are formed in higher concentrated aniline solution. [178] It was also recently reported that nano-fibrillar PANi was able to grow on normal substrates, such as on glass walls, polymer film, during dilute chemical polymerization. [179]

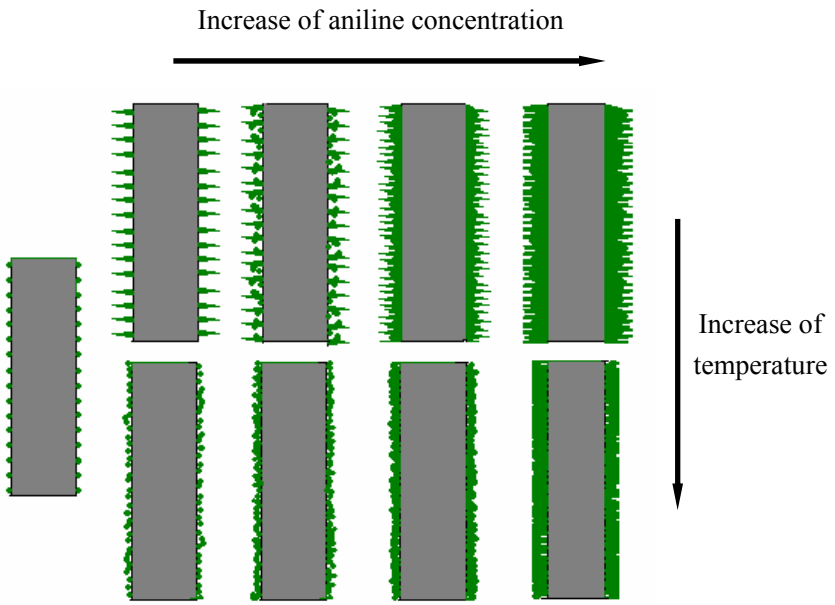

Fig 3.2.8 Schematic illustration of growth of polyaniline on polyamide electrospun fibers at different aniline concentration and temperature

So, according to previous reports and the morphology results which were obtained in different concentration of aniline and at different temperature, the possible mechanism

of growth of nanoPANi on the electrospun nanofiber could be concluded in following as: 1) firstly, PANi is nucleated spontaneously on substrates, and 2) then it continues to nucleate and grow as fibrillar, which is similar to that by electrochemical polymerization. [175] Nucleation and fibrillar growth are two competitive processes in the solution; High temperature favors nucleation, while low temperature favors fibrillar growth, and their speeds are determined by aniline concentration. The schematic illustration of growth of polyaniline on PA nanofibers is shown in **Fig 3.2.8.** At low temperature (0 ^{o}C), the PANi is in favor of fibrillar growth. In dilute aniline solution (0.02 M), the PANi is grown as nano-fibrillar shape (nanowires) on the nanofiber surface. Increase of aniline concentration accelerates the nucleation and leads to more nuclei nucleated on fibers surface, then causes to grow more PANi nanowires. So, a thick nanoPANi layer with very rough surface on PA fibers is formed at aniline concentration of 0.32 M at 0 ^{o}C. At high temperature (40 ^{o}C), the PANI favors nucleation. When aniline concentration is low (0.02 M), a thin layer of nuclei are formed. Increase of aniline concentration, speeds up the nucleation, lots of PANi nuclei are formed in a very short time, then the polymerization is finished quickly due to depletion of aniline, the PANi nuclei even have no time to growth as wire shape. The accumulation of PANi nuclei on fibers leads to a smooth PANi layer on PA fibers surface.

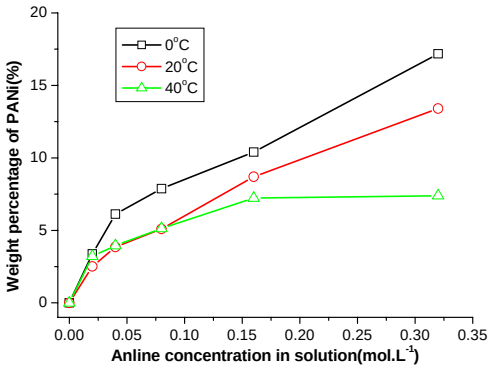

Fig 3.2.9 Weight percentage of PANi in PA/PANi PCNMs prepared at different temperatures in different aniline concentration solution

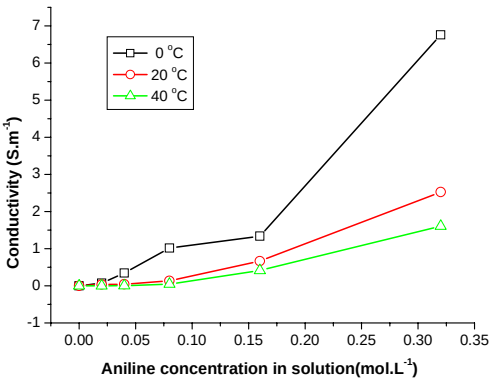

Fig 3.2.10 Conductivity of PA/PANi composite PCNMs prepared at different temperature in different aniline concentration solution

3.2.6 Electrical conductivity of PA/PANi composite fiber mats

Table 3.2.2 Conductivity and PANi content of PA/PANi nanofibers

Aniline conc. (M)	[a] Conductivity σ_c (S·m^{-1})			Weight percent of PANi (wt%)		
	0 °C	20 °C	40 °C	0 °C	20 °C	40 °C
0.02	0.0726	0.0365	8.67E-4	3.37	2.51	3.21
0.04	0.3447	0.0413	0.0017	6.12	3.85	3.95
0.08	1.0163	0.1345	0.045	7.88	5.1	5.13
0.16	1.3385	0.6652	0.413	10.4	8.7	7.23
0.32	6.759	2.5238	1.605	17.18	13.4	7.39

a. Thickness calculated by weight and density

The electrical conductivity of PA/PANi composite fiber mat was measured by four-point method which is presented in **Experimental 6.10**. The content of PANi and electrical conductivity of PA/PANi composite fiber mat is summarized in **table 3.2.2**. The conductivity curves of composite nanofibers prepared at different conditions are shown in **Fig 3.2.10**. In the PA/PANi composite nanofiber mat, PANi is the only conducting component. So, the conductivity of the composite nanofiber mat is dependent on the thickness of the PANi layer or the content of PANi. The higher the content of PANi is, the higher the electrical conductivity of the PCNMs. As shown in **Fig 3.2.9**, the highest content of PANi was obtained from the highest aniline concentration at low temperature of 0 °C. The conductivity of PCNM increases with increase in aniline concentration and decrease in temperature. The maximum conductivity of PCNMs is up to 6.759 S·m^{-1}, which was achieved in 0.32 M aniline solution at 0 °C, it outperforms that of PCNMs produced by direct electrospinning of blends which contained high molecular weight polymer and conducting polymer or carbon nanotubes, [162-164] by adsorption of carbon nanotube on electrospun nanofibers, [166] and by vapor phase deposition/polymerization of conducting polymer on electrospun nanofibers. [167]

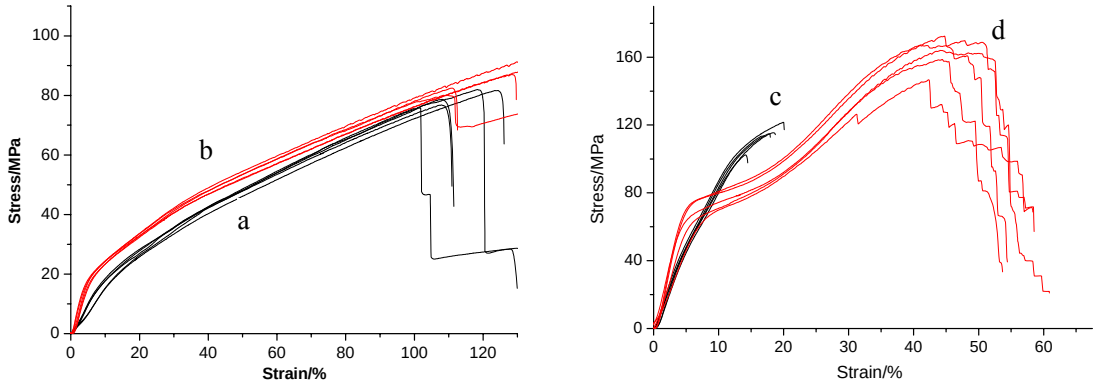

Fig 3.2.11 Stress-strain curves of pure PA nanofibers and PA/PANi composite nanofiber mats and belts; a) non-aligned PA mats; b) non-aligned PA/PANi mats; c) aligned PA belts; d) aligned PA/PANi belts, prepared from 0.02M aniline in 1M HCl solution, at room temperature

Table 3.2.3 Mechanical properties of PANi/PA composite nanofibers

Samples	Thickness /μm	Content of PANi / wt %	Strength /MPa	Modulus /GPa	Elongation to break/%
PA non-aligned fiber mat	15.03	0	77.55	0.23	121.9
PA/PANi non-aligned fiber mats	15.03*	2.85	82.88	0.49	124.8
PA aligned belts	10.28	0	113.61	0.79	17.6
PA/PANi aligned belts	10.28*	2.43	161.75	1.18	58.0

*The thickness of mats and belts after growing with PANi was same as that before growing PANi

3.2.7 Mechanical properties

The mechanical properties of PA/PANi composite PCNMs are investigated, listed in **table 3.2.3**, and the stress-strain curves are shown in **Fig 3.2.11**. After growth of about 2.85 wt% of nanoPANi on PA nanofibers, there are small improvements of 7% and 49% on the tensile strength and modulus of non-aligned mat, respectively, while the elongations are nearly the same. The tensile strength of a highly aligned composite belt with 2.43 wt% of PANi shows a great increase of 42%, from 113.61 MPa of pure PA to 161.75 MPa of the composite nanofiber belt, as well as the

elongation to break increases from 17.6% to 58%, of 241% raise. The improvements on the mechanical properties of PA/PANi composite nanofibers are attributed to the nanoPANi on the fiber surface which enhances the connections between fibers. For non-aligned mat, fibers are assembled randomly, the PANi connections are easy to break under tensile forces, so its mechanical properties show a little improvement. For the highly aligned fiber belt, fibers are aligned in one direction, the PANi connections between fibers are easy to break due to the same directions of the tensile forces and the fiber alignment, so its tensile strength and elongation show a great increase.

3.2.8 Thermal properties and bacterial compatibility

PA and PANi both are thermally stable polymers. So, the composite nanofibers from PA and PANi also show good thermal properties. The 5 % weight loss temperature is up to 415 ^{o}C, as shown in **Fig 3.2.12**.

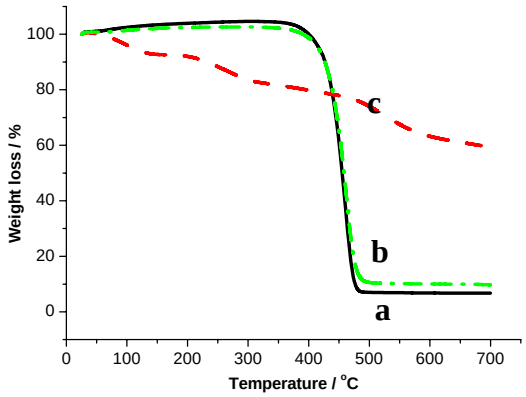

Fig 3.2.12.TGA thermographs of a) PA nanofibers, b) PA/PANi nanofibers, c) PANi powder (HCl doped) in air

More recently, there is a growing interest in conductive polymers for diverse biomedical application. As one of the most studied conducting polymer, PANi is biocompatible and can be used for tissue engineering applications [162] and serve as modifying layer of anode in microbial fuel cells (MFCs). [11, 180] The bacterial compatibility of PANi/PA composite PCNM is tested by qualitative and quantitative

ways, see in **Experiment 6.11**. In a qualitative way, it can be seen from **Fig 3.2.13A** and **B** that, after culture at 37 ^{o}C for 24 hours, the *E.coli* colonized on the PANi/PA nanofiber mats. In a quantitative way, **Fig 3.2.13C** shows that the optical density (OD) values of *E.coli* in the standard culture media with and without PANi/PA nanofiber mat are similar. It means that the PANi/PA nanofiber mat shows no effect on the growth of *E.coli*. Both results demonstrate that the PANi/PA nanofiber mat possesses excellent bacterial compatibility.

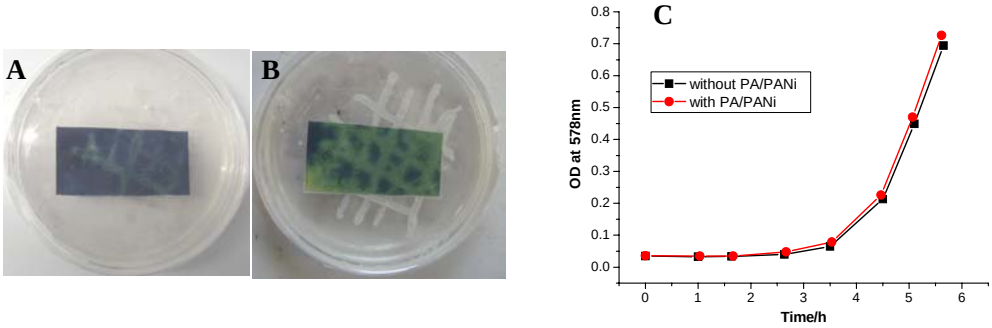

Fig 3.2.13. PA/PANi PCNM on culture medium inoculated with *E.coli*, A) before culture, B) after culture at 37 ℃ for 18 h, C) optical density at 578 nm of *E.coli* culture solutions with and without PA/PANi PCNM.

3.3 Conclusions

A novel conducting PCNM with nanoPANi on the fiber surface was successfully prepared by simple oxidative polymerization. The composite PCNM displays a core/shell structure with highly rough surface. The thickness and the morphology of PANi layer could be controlled by varying aniline concentration and temperature. The combination of the advantages of electrospinning technique and nanostructured PANi, let the PA/PANi composite PCNM possess more than five good properties, i.e. high conductivity of 6.759 $S{\cdot}m^{-1}$, high specific surface area of 160 $m^2{\cdot}g^{-1}$, good strength of 82.88 MPa for nonaligned mat and 161.75 MPa for highly aligned belts, good thermal properties with 5% weight loss temperature up to 415 ^{o}C and excellent biocompatibility.

But, in the PA/PANi composite PCNM, the PANi is the only conducting component,

its conductivity of 6.759 $S \cdot m^{-1}$ which was measured in dry-state, is not enough for application as electrode in fuel cells. Moreover, the conductivity decreases in neutral pH environment due to the de-doping of proton. However, the method of spontaneous growth of nanoPANi on electrospun fiber mats provides an effective method to produce porous electrically conducting electrospun fiber mats. The combined advantages of nanostructured PANi with the electrospun fiber mats, extends the application of PANi and electrospun nanofibers, such as chemical- and bio-sensors, actuators, catalysis, electromagnetic shielding, corrosion protection, separation membranes, electro-optic devices, electrochromic devices, tissue engineering and so on.

4. Three-dimensional electrospun carbon fiber mats as anodes in microbial fuel cells

Shuiliang Chen, Haoqing Hou, Falk Harnisch, Sunil Patil, Alessandro Alfredo Carmona-Martinez, Seema Agarwal, Alexander L. Yarin , Andreas Greiner*, Uwe Schröder*, nanoscale 3D electrode habitat boosts microbial bioelectrocatalysis, *Nat Biotechnol*, 2010, submitted

4.1 Introduction

Biofilms – complex aggregates of microorganisms embedded in their self-produced matrix – are the most abundant life-form of microorganisms on Earth and are formed on virtually every surface. Formation of a biofilm begins with the attachment of free-floating microorganisms to a surface, and is followed by five-stages of development. [181] Considerable attention has recently been caught by the finding that the microbial biofilms that are adapted to extracellular electron transfer can efficiently convert chemical energy into electricity. [3, 8, 9] Key players in such biofilms are electroactive bacteria [182] like *Geobacter* [183] or *Shewanella* [184] species that are often also referred to as electricigens [183], exo-electrogens [185] or anode-respiring bacteria. [186] The use of electrochemically active biofilm in microbial fuel cells (MFCs) or its modified form of sediment microbial fuel cell (SMFC) [22, 187, 188] and microbial electrolysis cells (MECs) [53, 189, 190] for conversion of chemical energy to electricity or hydrogen is a fancy idea, which possesses a great potential in the context of future sustainable energy supply and handling. Diverse organic compounds, such as biomass from farm, even domestic and industrial waste, which are rich in chemical energy, can be transformed and serve as nutrition for biofilm.

The anodes of MFCs in most reports [180, 191-193] are two-dimensional (2D), which only allow biofilms to grow one layer on the surface. Thus, the current density at

high-performing electrochemically active microbial biofilms lies between 0.5-1.2 $mA \cdot cm^{-2}$ – a maximum performance that to a large extent is limited by biofilm density and the kinetics of electron and mass transfer within the biofilm. [194] Although several new materials, such as carbon nanotube/PANi composite,[193] TiO2/PANi composite, [180] mediator mobilized carbon, [191] especially three-dimensional reticulated vitreous carbon (3D-RVC), [56] fiber materials, [33, 195] have been reported to enhance the anodic performance, the resulted current density are still too low to put into large-scale application, e.g. wastewater treatment. The so far only way to significantly increase the anodic performance beyond that level are concepts involving suspended bacterial cultures. [11, 196]

Herein, two kinds of nano-scale 3D anode, *porous electrospun carbon fiber mat (porous 3D-ECFM*) and *layered electrospun carbon fiber mat (layered 3D-ECFM)*, are presented to improve the anodic performance. The anodic performances of these mats are investigated in half-cell and full-cell MFCs systems. Also the microbial biofilms in these mats are investigated by scanning electron microscope (SEM).

4.2 Results and Discussion

4.2.1 Escherichia coli biofilm on 2D carbon fiber mat produced by normal electrospinning

As shown above, the conductivity of PA/PANi composite PCNM (about 6.759 $S \cdot m^{-1}$) is not enough for application as anode in MFCs. So, in this part we turn to electrospun carbon fiber mat (ECFM), which shows good properties of high conductivity and environmental stability. The biofilm behavior on/in two-dimensional ECFM (2D-ECFM) which was prepared by normal electrospinning of polyacrylonitrile (PAN) and carbonization at 1000 ^{o}C, is investigated. The properties of 2D-ECFM are listed in **Table 4.2.1.** The conductivity of 2D-ECFM is about 1.08×10^{4} $S \cdot m^{-1}$, which was measured by the four-point method. It is three orders of magnitude higher than that of PA/PANi composite PCNM. The diameter of the electrospun PAN fiber is about 1μm

(**Fig 4.2.1A**), after carbonization, the fiber is shrunk to about 500 nm in diameter (**Fig 4.2.1B**). The pore size of this ECFM is about 1 μm and the porosity is around 94%. The cross-section view of SEM image **Fig 4.2.1** shows that the thickness of this 2D-ECFM is about 40 μm**.** The 2D-ECFM was glued on the graphite rod and served as anode in *Escherichia coli (E.coli)*-based MFCs. 10 $g \cdot L^{-1}$ glucose in 0.1 M phosphate buffer solution (PH=7.0) with inoculated *E.coli* served as anolyte and 0.1 M potassium ferricyanide ($K_3Fe(CN)_3$) in 0.1 M phosphate buffer solution (PH=7.0) served as catholyte. The anode and cathode were separated by a cation exchange membrane and the distance in between was about 4 cm. 10 $\mu mol \cdot L^{-1}$ of methylene blue (MB) was added as mediator to enhance the electron transfer in the anode chamber. A resistor of 1000 Ω was connected between the anode and cathode.

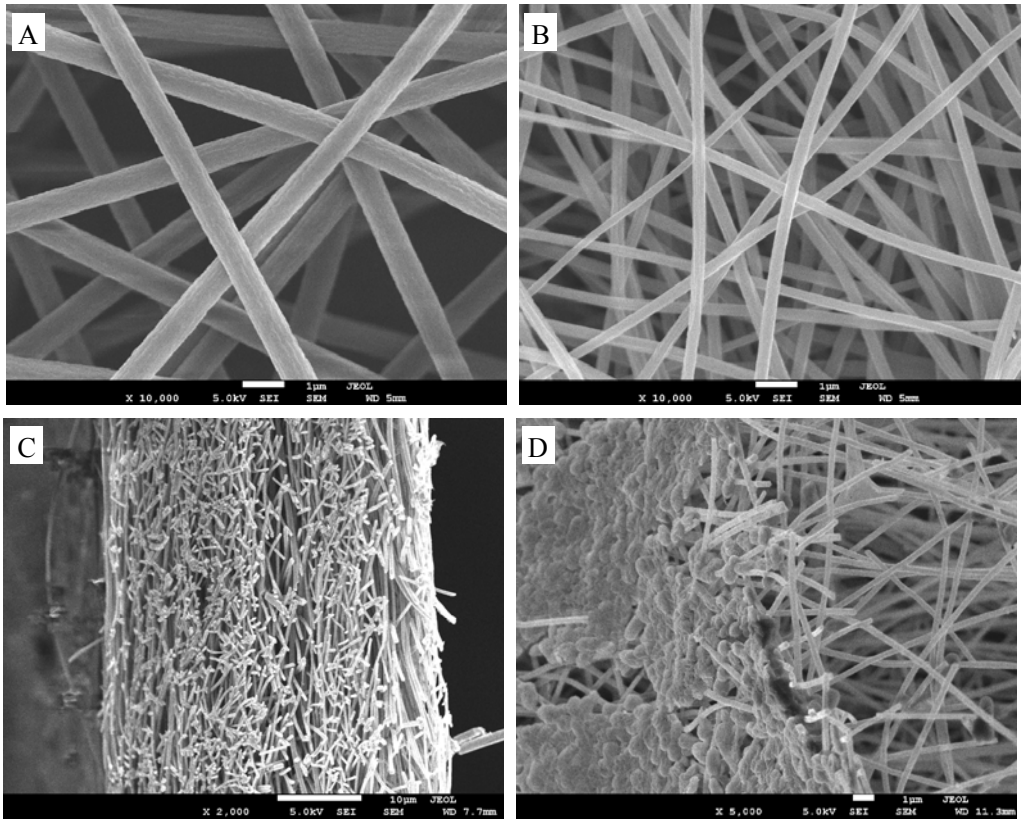

Fig 4.2.1 SEM images of A) electrospun PAN fibers, B) top view and C) cross-sectional view of electrospun PAN-based carbon fibers, D) *E.coli* on electrospun PAN-based carbon fiber mat. Scale bars of A, B and D are 1 μm, C is 10 μm.

After electricity generation for about 96 h, 2D-ECFM anode with *E.coli* biofilm was taken out from the fuel cell. The biofilms on the anode were simply fixed by glutaric dialdehyde and dehydrated by ethanol (following **Experimental 6.19**), and then were observed by SEM to analyze the morphology of the *E.coli* biofilm. As shown in **Fig 4.2.1D**, the *E.coli* biofilms only grew on a layer on the surface of 2D-ECFM, but did not go inside the mat. It could be concluded that the pore size and porosity in the 2D-ECFM which was prepared by normal electrospinning is too small for microorganisms to penetrate inside the mat. So, in order to obtain high current density, three-dimensional (3D) carbon fiber mat with higher porosity and bigger pore size is required for efficient penetration of microorganisms and diffusion of substrate,

Table 4.2.1 Properties of carbon fiber mats by electrospinning

Sample	Mean pore size/μm	Porosity /%	Porous index ($\frac{V_T}{V_S}$ or $\frac{\delta_T}{\delta_S}$)	Density /kg·m^{-3}	Resistivity / Ω·cm^{-1}
Graphite felt	47	95.7	25	100-180	0.15
2D-ECFM	0.6	94	16.6	101	8
Porous 3D-ECFM	5.8	99	100	18	15
Layered 3D-ECFM (10 layers)	2.3	98.5	66.7	76	2.0

4.2.2 Preparation and properties of 3D-ECFM

4.2.2.1 Preparation and properties of porous 3D-ECFM

A novel porous 3D electrospun carbon fiber mat (porous 3D-ECFM) was prepared by a modified electrospinning, gas-assisted electrospinning (GE-spinning). Firstly, copolymer poly(acrylonitrile-co-itaconic acid-co-butyl acrylate) (PANIB) was electrospun into fiber mat by GE-spinning (see **Experimental 6.3.3**); then, the PANIB was carbonized to carbon fiber mat (see **Experimental 6.4**). The PANIB fiber mat

resulted from GE-spinning shows highly porous 3D structure. The possible reason for the formation of highly porous fiber mat in GE-spinning might be due to removal of net charges from the fibers by the airflow. The removal of net charges on the fibers decreased the driving forces toward the collector, and the resulting fibers deposited loosely onto the collector. As shown in **Fig 4.2.2,** after carbonization, the porous 3D structure of the mat is retained, and much void space is left during carbonization process. The mean pore size and porosity of the resulting carbon fiber mat are about 5.8 μm and 99%, respectively, which are much higher than that of the 2D-ECFM with about 0.6 μm and 94% obtained from normal electrospinning, respectively (the porosity and pore size measurements are shown in **Experimental part 6.15 and 6.16**). Comparing SEM images in **Fig 4.2.1C** and **Fig 4.2.2C**, the scale bars and magnifications of both images are 10 μm and 2000x, respectively, the fibers in porous 3D-ECFM (**Fig 4.2.2C**) from GE-spinning are much looser than that in 2D-ECFM (**Fig 4.2.1C**) from normal electrospinning.

Define porous index (PI) as ratio of total volume V_T to solid volume V_S of fiber mat ($\frac{V_T}{V_S}$), which is another way to describe the porosity of fiber mat, see **Experiment 6.15**. The PI of porous 3D-ECFM is 100. It is five times higher than that in 2D-ECFM of about 16.8 which was obtained from normal electrospinning. A piece of porous 3D-ECFM is shown in **Fig 4.2.2A,** the porous structure of this porous mat material is extremely stable, it resists mechanical stress or treatment with water. This might be attributed to the rigidity of the carbon fiber and existence of junctions (**Fig 4.2.2D**) between the fibers. The thickness of porous 3D-ECFM measured from the SEM image of **Fig 4.2.2B**, is around 1.5 mm. Then the density of this mat is calculated following Eq. 6.15-1 in **Experiment 6.15**. This porous 3D-ECFM shows a very low density of only about 18 $kg \cdot m^{-3}$, which is much lower than that of conventional carbon-based materials, such as graphite felt (about 100-180 $kg \cdot m^{-3}$), granular graphite, RVC (>48 $kg \cdot m^{-3}$, Duocel® RVC Foam), and is also much lower than 2D-ECFM (about 101 $kg \cdot m^{-3}$).

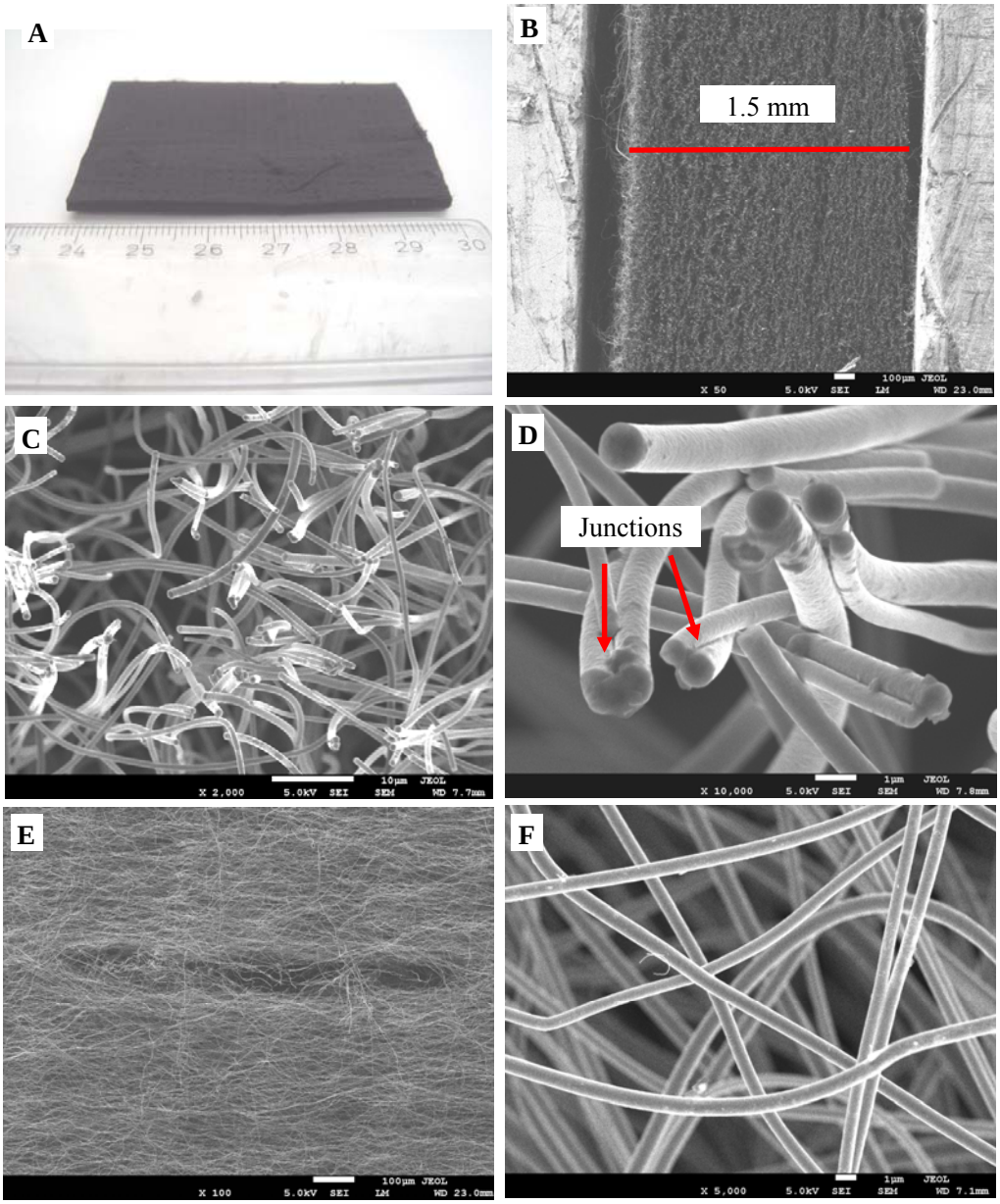

Fig 4.2.2 Digital picture A) and SEM images B, C and D) cross sectional view and E and F) top view, of porous 3D-ECFM by GE-spinning, Scale bars of B and E are 100 µm, C is 10 µm, D and F are 1 µm.

4.2.2.2 Preparation and properties of layered 3D-ECFM

A layered 3D electrospun carbon fiber mat (layered 3D-ECFM) is designed to serve as MFCs anode that let the biofilm grow layer-by-layer (LBL) in the mat. The microorganism and the substrate would pass inside the mat through the space between layers and pores among fibers. Roll paper (*ja! Tissue Toilettenpapier, bought from*

supermarket) made from natural cellulose fibers (NC) is porous with a mean pore size of about 20 μm and with a thin thickness of about 30 μm for each layer (measured from SEM image of **Fig 4.2.3B**). Moreover, it can be carbonized to carbon and shows low electrical resistivity of 7.3±0.1 $\Omega \cdot cm^{-1}$ for each layer. The Energy dispersive X-ray analysis (EDX) spectral, as shown in **Fig 4.2.3C**, shows that the roll paper derived carbon fiber mat contains a very small amount of normal metal element, Na, Al, K, Ca, with form of phosphate or sulfate salts. These elements all have already existed in the artificial wastewater and will show no special effect on the growth of microorganisms.

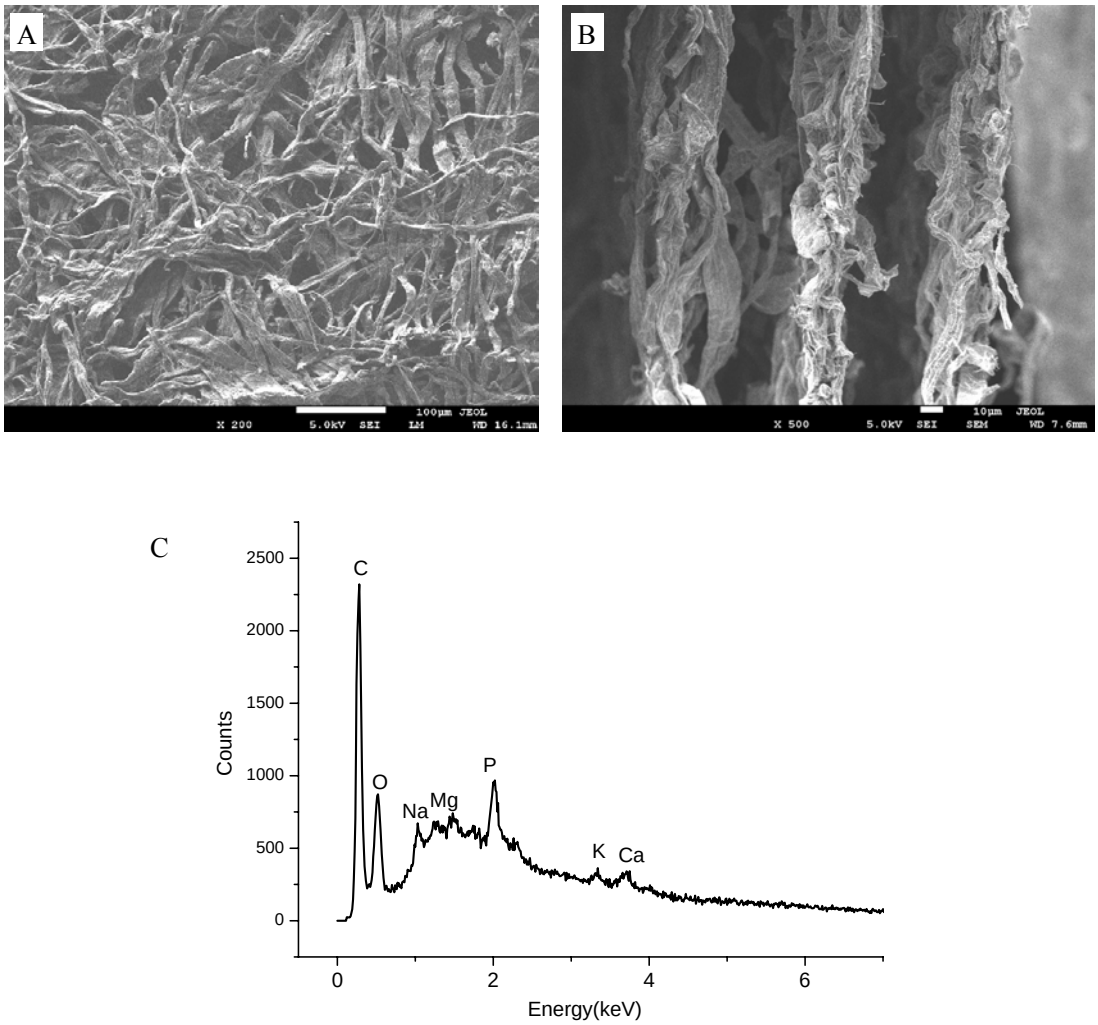

Fig 4.2.3 A) Top view of carbon mat from roll paper, B) Cross-sectional view of carbon mat from roll paper (three layers), the thickness of each layer is about 30 μm. Scale bars of A is 100 μm, B is 10 μm. C) The Energy dispersive X-ray analysis spectra of roll paper derived carbon fiber mat

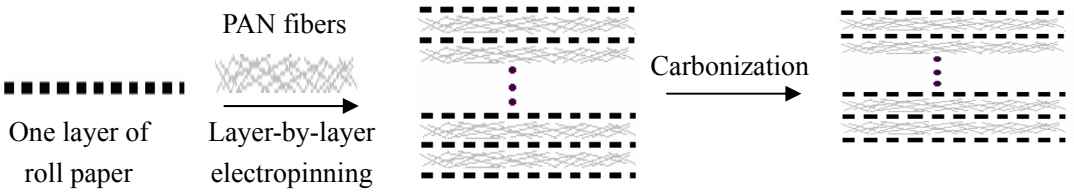

Fig 4.2.4 Schematic diagram of preparation of layered 3D-ECFM by layer-by-layer electrospinning

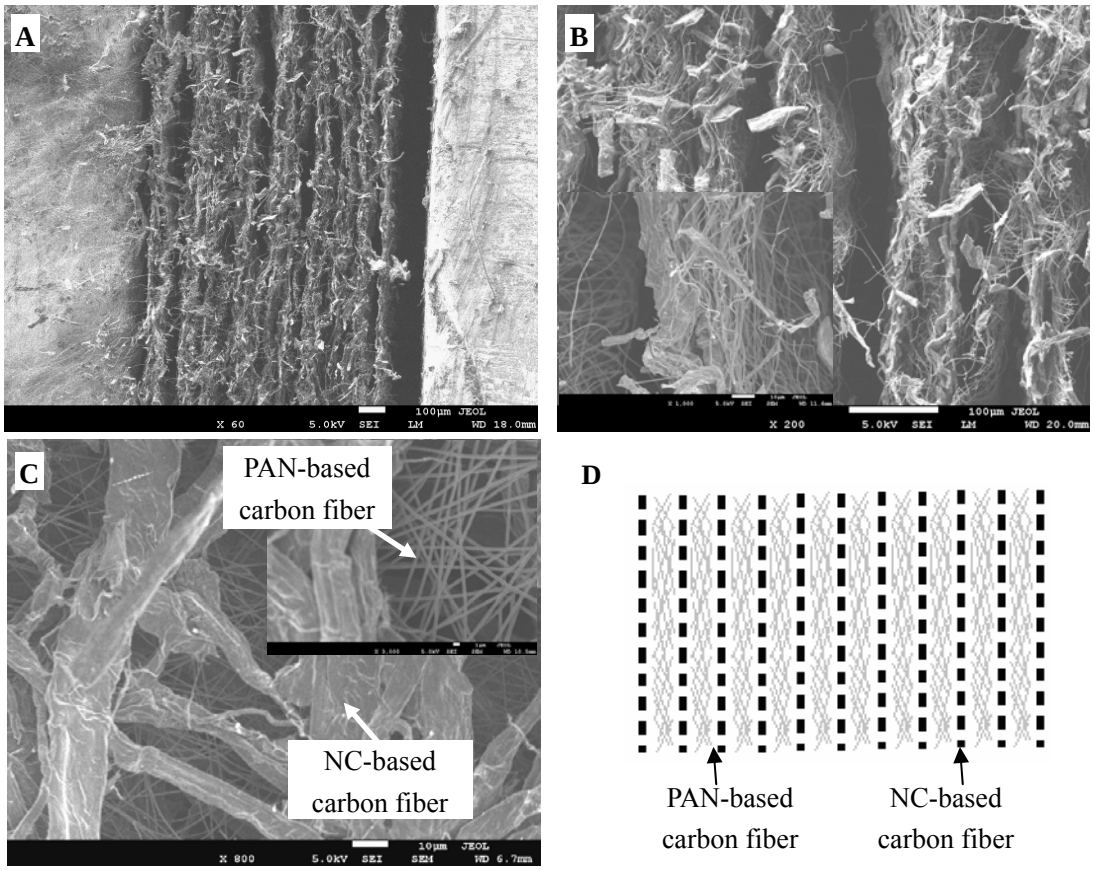

Fig 4.2.5 SEM images of layered 3D-ECFM (ten layers) by LBL electrospinning, A and B) cross-sectional view and C) top view, diameter of small fiber is about 500nm, scale bars of A and B are 100 μm, C is 10 μm, D) model of cross-sectional view of layered 3D carbon fiber mat

This roll paper was used as support to make layered 3D-ECFM. Steps for the preparation of 3D layered material are: 1) PAN fibers are LBL electrospun on roll paper layer to make 3D PAN/NC composite fiber mat; 2) then, the composite fiber mat was carbonized at 1000 ^{o}C under N_2 and converted into PAN/NC-based 3D carbon fiber mat, as shown in **Fig 4.2.4**. The properties of layered 3D-ECFM are

listed in **table 4.2.1**. As shown in SEM images of **Fig 4.2.5,** in this layered 3D material, small fibers with a diameter of about 500nm were assembled on the NC big fiber (10-30 μm) layers by LBL electrospinning. The layered 3D-ECFM shows high surface area and also high porosity of 98.5%, due to big distance of over 50 μm between layers and small diameter electrospun fibers (**Fig 4.2.5 B**). It would be enough for microorganisms passing through and growth of stable layered biofilm.

4.2.3 Anodic performance of 3D-ECFM in half-cell system

A potentiostat is employed to investigate the anodic performance in half-cell due to its resistance compensation function, which can eliminate the effects of anode resistance and other parameters. The microorganisms in sludge from wastewater plant were used for the inoculum in MFCs. Before inoculation, the microorganisms were firstly acclimated (following **Experimental 6.18**) to select the electrochemically active microorganisms which could generate high electricity[54]. Carbon fiber mats glued on the graphite foil served as working electrode. Artificial wastewater with sodium acetate substrate in which acclimated microorganisms were inoculated served as medium. The working electrode was potentiostatically poised at a potential of 0.2V (vs Ag/AgCl, sat. KCl, 0.195 V vs. SHE), which played the role of cathode. The biocatalytic current generation curves were recorded versus time, which originated from the oxidation of the substrate (acetate) catalyzed by microbial biofilms at the working electrode according to the following equation:

$$CH_3COO^- + 2H_2O \xrightarrow{\text{bioelectrocatalyse}} 2CO_2 + 7H^+ + 8e^-$$

For comparison, graphite felt (GF) (Weichfilz SIGRATHERM GFD, SGL Carbon GmbH Meitingen, Germany) with fiber diameter of 10μm serves as anode and was tested under the same condition.

4.2.3.1 Anodic performance of porous 3D-ECFM anode

The biocatalytic current generation curve of porous 3D-ECFM anode is shown in **Fig**

4.2.6B. About ten hours after the initial inoculation, the current density rises significantly, this indicates the formation of an electrochemically active biofilm. The geometric current density reaches a peak of over 3.0 $mA \cdot cm^{-2}$ about 110 h after inoculation. Then, it decreases due to the depletion of substrate. Refreshment of the medium after about 200 h, let the current density raise again, and reach over 3.0 $mA \cdot cm^{-2}$ again in relatively shorter time. It indicates that a stable electrochemically active biofilms have already formed in the porous 3D-ECFM during the first cycle. After refreshment of substrate, the microorganisms in the biofilms get sufficient nutrition and reach their full capacity of release of electrons (metabolism) quickly again. The maximum geometric current density of porous 3D-ECFM of 3.0 $mA \cdot cm^{-2}$ is nearly two times as that of GF which is about 1.6 $mA \cdot cm^{-2}$ (**Fig 4.2.6A**) at the same condition. It is, to our knowledge, the highest geometric current density achieved with electrochemically active microbial biofilms. The high geometric current density might be attributed to thick biofilms formed in the mat. And the thick biofilms are caused by higher surface area which is a result of small fiber diameter of about 1μm, big pore size and high porosity in the mat. Its corresponding weight current density of porous 3D-ECFM is very high, up to 714 $mA \cdot g^{-1}$, which is one order of magnitude higher than that of GF which generates weight current density of only about 48 $mA \cdot g^{-1}$. This super high weight current density is caused by extremely low density of the mat. Because, in comparison to commercial GF (100-180 $kg \cdot m^{-3}$), the density of porous 3D-ECFM (18 $kg \cdot m^{-3}$) decreases by 82-90 %. It lowers the amount of material to a minimum to obtain very high current.

Table 4.2.2 Anodic performance of carbon fiber mats

Sample	Geometric current den./ $mA \cdot cm^{-2}$	Weight current den./ $mA \cdot g^{-1}$	Cell density/$g \cdot m^{-3}$
Graphite felt	1.6	48	28.81
2D-ECFM	0.17	430	
Porous 3D-ECFM	3.0	714	72.55
Layered 3D-ECFM (10 layers)	2.0	294	

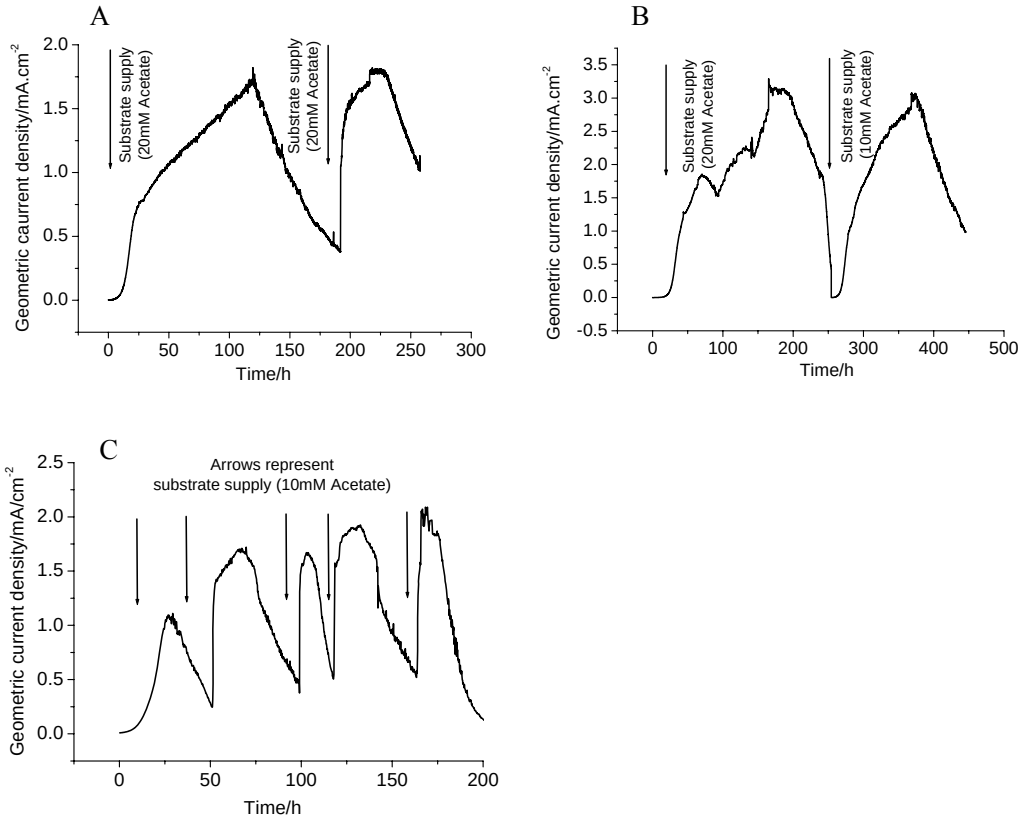

Fig 4.2.6 Biocatalytic current generation of electrodes in an exemplary semi-batch experiment A) Graphite felt, B) porous 3D-ECFM electrodes, C) layered 3D-ECFM.

4.2.3.2 Anodic performance of layered 3D -ECFM anode

The biocatalytic current generation of layered 3D-ECFM is also measured. As shown in **Fig 4.2.6C**, five cycles have been run for the layered 3D-ECFM. It generates a maximum geometric current density of 2.0 $mA \cdot cm^{-2}$, the corresponding weight current density is 294$mA \cdot g^{-1}$, both kinds of current density are much higher than that of GF, which might due to the layers of electrospun carbon fibers with smaller diameter and large space between layers, as well as due to the lower density of 76 $kg \cdot m^{-3}$.

4.2.4 Analysis of biofilms in 3D-ECFM

To confirm the anodic performance results above, biofilms in the fiber mats were investigated by scanning electron microscope (SEM) (JSM-7500F). All biofilm

samples were taken out from the MFCs medium after at least two cycle of electricity generation. After simple fixation and dehydration (see in **Experimental part 6.19**), these samples were coated with a layer of gold to increase conductivity and observed under SEM.

4.2.4.1 Biofilms in Graphite felt

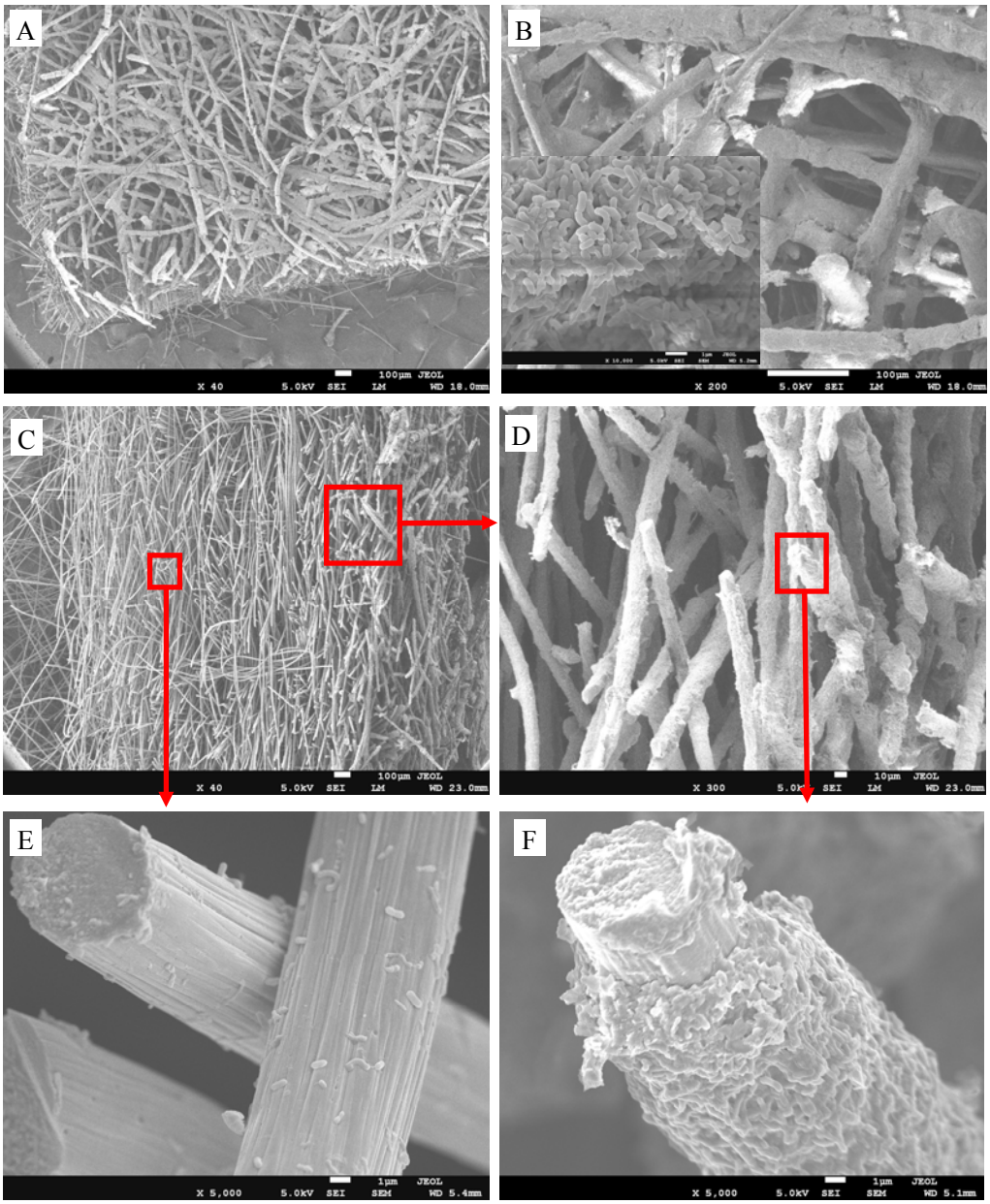

Fig 4.2.7 SEM images of biofilms in the graphite felt after electricity generation. A) and B) top views, C, D, E and F cross-sectional views. Scale bars of A, B, C are100 µm, D is 10 µm, E and F are 1 µm.

As shown in **Fig 4.2.7,** from the top view images we can see that a very thick biofilm was formed on the GF. Due to the big fiber diameter (10 μm), thick biofilms were formed from small microorganisms with size of around 0.2-1 μm and covered around each fiber. Though the mean pore size in GF is over 50 μm (**Fig 4.2.7B**) and absolutely enough for small microorganisms and nutrition penetration, thick biofilms were only able to be formed in the upper layer of the felt with a depth of about 500μm, there were very few microorganisms which could grow in deeper depth of the felt (**Fig 4.2.7E**). The thickness of biofilms in the mat decreased with increase in depth of the felt.

4.2.4.2 Biofilms in porous 3D-ECFM

SEM images of biofilms in the porous 3D-ECFM are shown in **Fig 4.2.8.** From the top view of SEM images (**Fig 4.2.8B, C and D**), we can see that almost all carbon fibers were covered by very thick and stable biofilms which were formed in porous 3D-ECFM and there were not any fibers are exposed. It is very surprising that though very thick biofilms covered the surface of the porous mat, still lots of holes were left for nutrition transportation. The cell density in the porous 3D-ECFM is up to 72.55 $g \cdot m^{-3}$(dried protein), which is 2.5 times more than that in GF (28.81 $g \cdot m^{-3}$).

But, similar to that in GF, as shown in **Fig 4.2.8E**, from the cross-sectional view of the SEM images we can see that the thick biofilms were grown in the upper layer of the carbon fiber mats, with depth of about 250 μm (**Fig 4.2.8E, F and H**). While in deeper depth of the mat, there grew few microorganisms, see in **Fig 4.2.8G**. Though the pore size in the mat is large (about 5.8 μm) enough for penetration of small microorganisms (about 0.2-1μm), the thick biofilms are only formed in the upper layer of the mat.

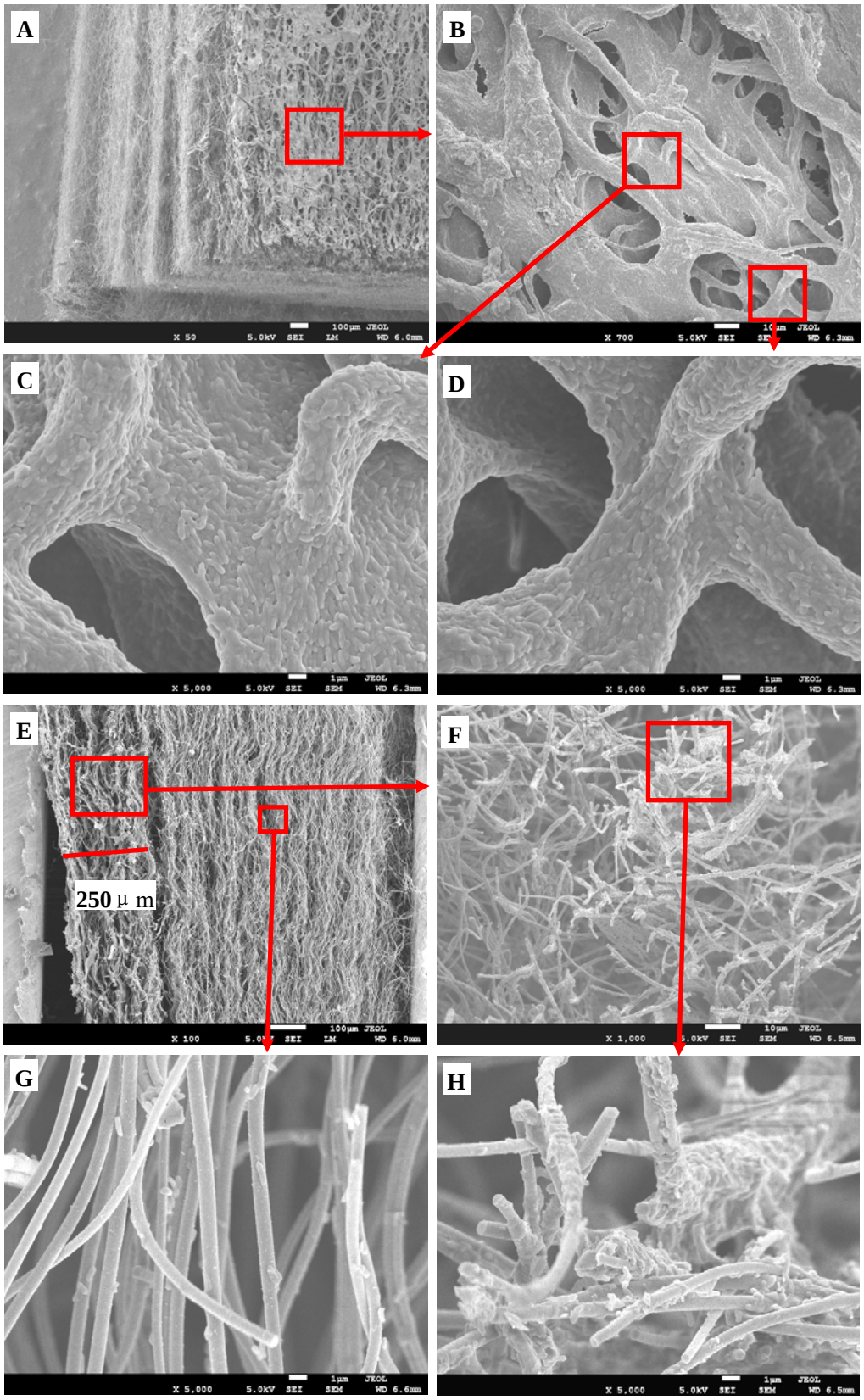

Fig 4.2.8 SEM images of biofilms in the porous 3D-ECFM after electricity generation, images of A, B, C and D are top views, E, F, G and H are cross-sectional views. Scale bars of A and E are 100μm, B and F are 10μm, C, D, G and H are 1μm.

4.2.4.3 Biofilms in layered 3D-ECFM

As shown in **Fig 4.2.9**, very thick biofilms were formed layer-by-layer in the layered 3D-ECFM which is in accordance with our expectation. The thickness of biofilms in the first layer is very thick, around 10μm (**Fig 4.2.9C**). The thickness of the biofilms becomes thinner in the deeper depth of fiber layers.

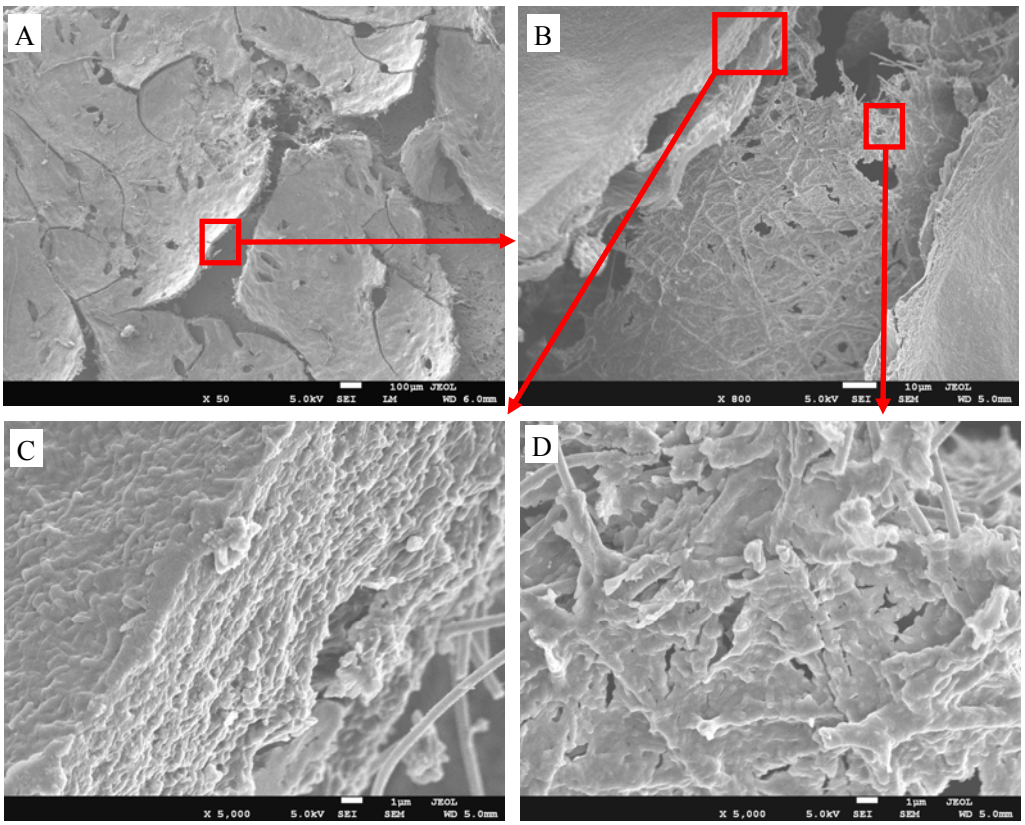

Fig 4.2.9 SEM images of biofilms in the layered 3D-ECFM after electricity generation. Scale bar of A is 100μm, B is 10μm, C and D are 1μm.

4.2.5 Discussion

Compared to the GF, the porous 3D-ECFM possesses similar 3D fiber architecture but ten times smaller fiber diameter. While compared to the 2D-ECFM, porous 3D-ECFM shows a highly porous architecture with an extremely high porosity of 99%. So, for the porous 3D-ECFM, the generation of higher geometric, especially super-high weight current density of 714 $mA \cdot g^{-1}$, might be attributed to:

1) Ten times higher surface area, which is the result of a ten times smaller fiber diameter (see Eq. 6.17-3 in **Experimental 6.17**). The higher surface area provides much more surface for growth of biofilms;

2) Small fiber diameter of around 1μm which favors the formation of thick and stable microbial biofilms in inter-fibers;

3) Super-high porosity of 99% and big pore size of 5.8 μm in porous 3D-ECFM favor the penetration of microorganisms and diffusion of nutrition;

4) Extremely low density of 18 $kg \cdot m^{-3}$ which is of utmost importance, since it not only lowers the amount of material to a minimum but also maximizes the penetration of microorganisms and the diffusion of substrate.

The layered 3D-ECFM generates high geometric and weight current density due to 1) the small electrospun fiber on each layer and 2) big space between fiber layers. The small fiber layers facilitate the formation of stable microbial biofilms, and the big space between fiber layers provides the channels for diffusion of nutrition and penetration of microorganisms and space for growth of the microorganisms.

However, the growth of thick biofilms in deeper depth of the 3D anodes is still difficult. Even in GF, as shown in **Fig 4.2.7,** the average pore size is over 50 μm, but the depth of the felt which biofilm could grow is no more than 500 μm. The possible reason is caused by poor diffusion of nutrition deep in the mats. Because microorganisms are apt to aggregate and form biofilms, and the thick biofilms formed in the upper layer cover most of small pores in the mats (**Fig 4.2.8B**), on one hand the formed biofilm in the upper of the mat on the one hand hindered the diffusion of nutrition, on the other hand gradually consume most of diffusional nutrition. That makes the nutrition transportation insides the mat difficult, so make biofilms grow deep depth of mat difficult.

If the porosity of mats is further increase of (over 99%), or large holes or channels (larger than 50 μm) which can not be covered by biofilm are made in porous 3D-ECFM and layered 3D-ECFM, as well as the continuously flow nutrition feeding is used, the nutrition transportation to inside of mat would be greatly facilitated and thick biofilms would grow in whole 3D mats. Then, the biofilm density in the mat

would greatly increase, and the geometric or weight current density would be increased further.

4.2.6 Performance of porous 3D-ECFM anode in Full-cell system

To investigate the power density of porous 3D-ECFM anode, a full-cell experiment was carried out in batch mode using a two-chamber cube MFC. [15] The two chambers were separated by ion-exchange membrane (fumasep FKE). The anode - porous 3D-ECFM with size of about 2×2.5 cm^2 and weight of about 0.017g - was fixed in a stainless steel needle plate, and both sides of mats were available for growth of biofilms and used for current density calculation, see **Experiment 6.13**. The anolyte was artificial wastewater which contained 10 mM sodium acetate as substrate. The ferricyanide was chosen as catholyte as it was easier to handle than an oxygen electrode. For practical operation the ferricyanide cathode will be replaced by oxygen cathode. The open circuit of the fuel cell is 774 mV. **Fig 4.2.10** shows the polarization and power density curves of the full-fuel system as a function of the measured steady current. The maximum geometric power output density is about 0.35 $mW.cm^{-2}$, which is corresponded to a current density of 0.96 $mA{\cdot}cm^{-2}$ and at a cell potential of 365 mV. The weight power density is 0.206 $W{\cdot}g^{-1}$ with corresponding weight current density of 0.565 $A{\cdot}g^{-1}$.

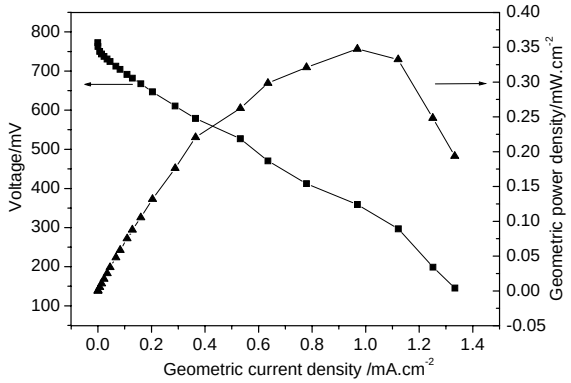

Fig 4.2.10 Power output and polarization curves of MFC with porous 3D-ECFM

4.3 Conclusions

The current density is greatly dependent on the biofilm density of the anode in MFCs. The 2D-ECFM which was prepared by normal electrospinning only allowed growth of microorganism on the surface with thin layer owing to the low porosity and small pore size in the mat. With the concept of increasing the power density of MFCs by increase of microorganism density in the anode, two novel 3D electrospun carbon fiber mats, *porous 3D-ECFM* and *layered 3D-ECFM*, were developed.

The porous 3D-ECFM made by GE-spinning shows a high specific surface area due to small fiber diameter of 1 μm, a stable highly porous structure with a porosity of 99%, big pore size of around 5.8 μm in the mat and very low density of 18 $kg \cdot m^{-3}$. The porous 3D-ECFM anode is very suitable for microbial biofilm growth and generates a very high geometric current density of 3.0 $mA \cdot cm^{-2}$, and a super-high weight current density of 714 $mA \cdot g^{-1}$.

The layered 3D-ECFM made by layer-by-layer electrospinning also shows a high porosity of 98.5% which mainly come from the void space between layers. This layered design is suitable for layer-by-layer growth of stable biofilm due to small electrospun carbon fiber on each layer. It generates a high geometric current density of 2.0 $mA \cdot cm^{-2}$ and weight current density of 294 $mA \cdot g^{-1}$.

Though the porosity and pore size in the mats are high enough for penetration of single small microorganism, the tendency of biofilms formation makes biofilm is unable to grow in whole mat but only in the upper layer about several hundreds micrometers or several layers, because the growth of biofilms is greatly limited by transportation of nutrition. Whereas, the transportation of nutrition to the inside mat is greatly hindered by the biofilms formed in the upper of mat. The current density of 3D-ECFM could be further improved by further increasing porosity and introducing big holes or channels in the mats for sufficient nutrition transportation to deeper depth of the mats.

5. Nanospring: a novel 3D porous architecture for anode in MFCs

1) **Shuiliang Chen**, Haoqing Hou, Ping Hu, Joachim H. Wendorff, Andreas Greiner, Seema Agarwal*, Polymeric Nanosprings by Bicomponent Electrospinning; *Macromol. Mater. Eng.,* **2009**, 294, 265–271.

2) **Shuiliang Chen**, Haoqing Hou, Ping Hu, Joachim H. Wendorff, Andreas Greiner, Seema Agarwal*, Effect of Different Bicomponent Electrospinning Techniques on the Formation of Polymeric Nanosprings, *Macromol. Mater. Eng.,* **2009**, *294*, 781–786

5.1 Introduction

As mentioned above, a stable 3D structure design with high porosity and big pore size are very important for the high performance anode in the MFCs, which allow the growth and penetration of the microorganisms, and make the nutrition transportation easy. But the growth of biofilms in whole 3D-ECFM is still limited, because the pores in mat are covered by biofilm formed in the upper mat. So, 3D fiber mat with higher porosity and pore size are required to solve this problem. It is well known that 3D crimp, curve or helix in fibers can lead to higher porosity than straight in the fiber mat, e.g. crimped wool fabrics, as shown in **Fig 5.2.1,** have a greater bulk than other textiles with straight fibers, which causes the product to retain heat. [206, 207]

In this part, a novel 3D porous architecture, polymeric nanosprings/helixes which were produced by bicomponent electrospinning, is designed as a potential anodic architecture in MFCs. Electrospinning yields fibers with diameters covering a range from a few micrometers down to a few nanometers. [5] The formed fibers can be smooth, porous, display branches or droplets dispersed along their length, may have circular cross-sections or are band-shaped depending upon the nature of the material and electrospinning parameters. A key phenomenon in electrospinning is the onset of a bending instability: a fluid jet ejecting from the tip of a die moves toward the

counter electrode in a linear fashion for only a short distance amounting typically to several centimeters. [132, 197-199] At the end of the straight path bending motions occur with growing amplitudes as the jet begins to follow a spiral and looping path in space. The curved fibers which result may have loops with diameter in the range of centimeters and more. But, the effect of such a curvature on elasticity will not be of great significance.

Fig 5.2.1 Digital picture of crimped wool

Curved structures with much smaller dimensions are known to result from buckling effects. Buckling is believed to result primarily from the presence of longitudinal compressive forces acting on fluid jets impinging on obstacles such as a planar substrate. [200, 201] Detailed investigations of the buckling phenomenon occurring in uncharged and charged jets impinging on motionless or laterally moving substrates have revealed a surprising richness of buckling pattern including sinusoidal trajectories, meandering, coiled structures, figure-of-eight structures double pattern, and many more. Furthermore the trajectories of the deposited nanofibers may result from a superposition of the looping motions due to bending instabilities and buckling. Such features certainly introduce some kind of elasticity into the fibers although such structures still do not correspond to ideal elastic elements.

More recently Kessick and Tepper [202] reported to have initiated the formation of helical structures approaching microscale helical coils from a composite of one

conducting polymer (poly(aniline sulfonic acid) and one non-conducting polymer (poly(ethylene oxide) by conventional electrospinning from a solution blend. The helical coils were claimed to form only on electrically conductive substrates, the helical diameters being in the range 5–20 mm. The authors suggested that the helical structures are formed due to viscoelastic contraction upon partial charge neutralization of the charged fibers. No indication on the internal structure of the bicomponent nanofibers was provided. More importantly it was argued later that this interpretation meets with contradictions and that the features described in the paper can be explained solely on the basis of buckling.[201]

A different concept was introduced by Lin et al.,[145] as they combined an elastomeric polymer (elastomeric polyurethane) with a thermoplastic one (polyacrylonitrile) in the so called side-by-side electrospinning: deposition of layers of one kind of nanofibers on top of a layer of a second kind of nanofibers. They were able to produce helical fibers obviously originating from the fact that the two components displayed different shrinkages after electrospinning. On the other hand Gupta and Wilkes [203] only achieved straight fibers when applying the side-by-side technique to the bi-component system poly(vinyl chloride) and segmented polyurethane (Estane).

The investigations reported so far convinced us that the parallel arrangement of an elastomeric and a thermoplastic polymer in electrospun nanofiber systems may have the potential to display buckling of the kind discussed above based on different shrinkage and the resulting longitudinal compressive forces but even more importantly to introduce tightly coiled nanosprings approaching ideal spring elements. The concept was to construct such a parallel arrangement within a nanofiber in terms of bi-component fibers.

In this work we introduced the formation of spring or helical nanofibers by coaxial electrospinning and analyzed the effect of different shrinkage of components in such core-shell fibers on spring formation. We tried to find out whether variations in the conductivity of the spinning solutions contribute to spring formation. The thermoplastic elastomer polyurethane (TPU) and the thermoplastic stiff polymers poly(m-phenylene isophthalamide) (Nomex®), polylactide (PLA), and

polysulfonamide (PSA) were chosen as model compounds. In addition, other two bi-component electrospinning techniques, off-centered electrospinning and side-by-side electrospinning were also presented to obtain high efficiency of nanosprings. The mechanical properties of aligned nanofiber mats containing spring or helical nanofibers were investigated.

5.2 Results and discussion

5.2.1 Conventional electrospinning of the model polymers

Table 5.2.1 Properties of elelctrospinning solutions

Solution / wt%	Viscosity / Pa·s (25 ℃) at 3000 $r \cdot s^{-1}$	Conductivity/$ms \cdot cm^{-1}$ (25 ℃)
18%TPU/DMF	1.620	0.0023
18%TPU/DMF/THF(3/1)	1.363	
18%TPU/DMF/4%LiCl	1.034	1.024
13.5% Nomex®/DMAc/4%LiCl	1.845	1.443
13%PSA/DMAc	0.683	0.0018
13%PSA/DMAc/1%LiCl	0.713	0.554
13%PSA/DMAc/2%LiCl	0.795	1.115
13%PSA/DMAc/4%LiCl	0.824	1.244

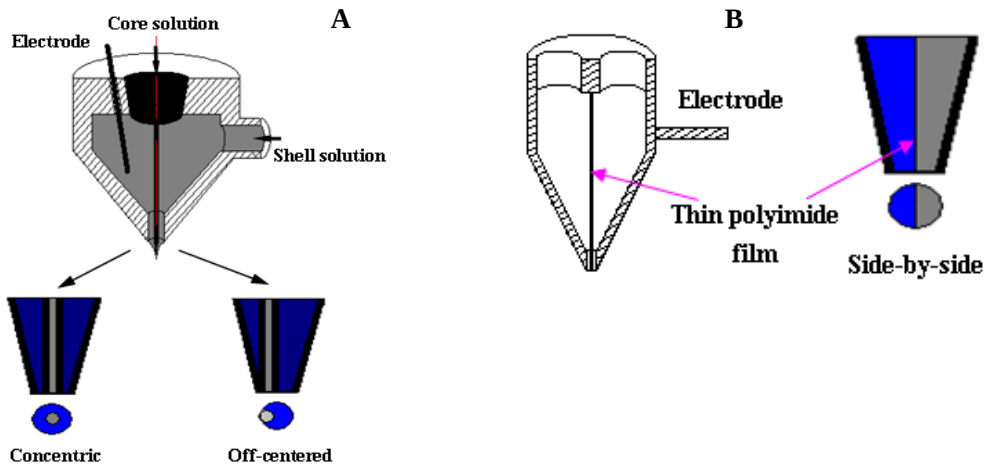

Fig 5.2.2 A) Coaxial, off-centered and B) side-by-side electrospinning spinnerets used in the work.

To start with, electrospinning was applied to the pure TPU and the rigid materials (Nomex®, PLA, and PSA) without and with addition of the salt to enhance the

conductivity of the spinning solutions. Electrospinning was carried out in all cases at 24 kV with 15 cm distance between the electrodes. Electrospinning of the rigid materials (Nomex®, PLA, and PSA) only gave straight fibers (**Fig 5.2.3**) even in the presence of 4wt % LiCl in their spinning solutions. The electrospinning of 18 wt% of TPU (flexible material) solution in DMF/THF (3:1, weight ratio) (**Fig 5.2.4A**) without LiCl also yielded nanofibers with diameter ranging from 250 to 500 nm which did not show any buckling or spring formation. However, the addition of 4 wt% of LiCl to the TPU solution gave indications of some buckling (**Fig 5.2.4B**). It is quite possible that both the proper mechanical properties of the materials which are electrospun and the conductivity of the spinning solutions may contribute to buckling spring formation.

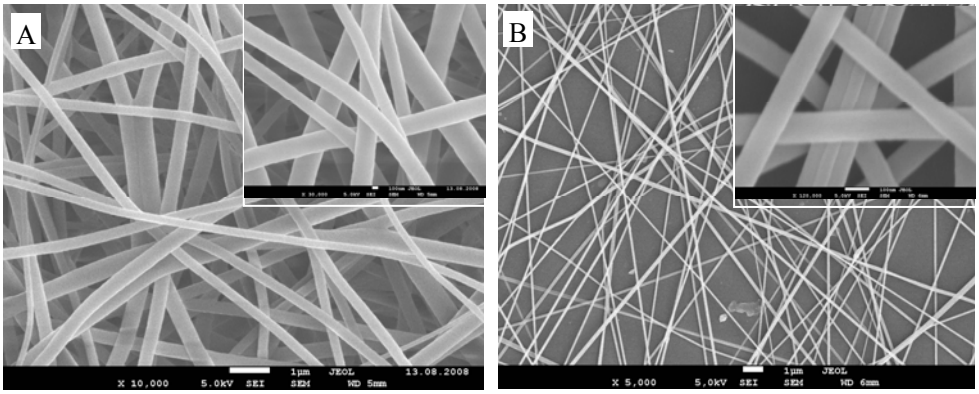

Fig 5.2.3 SEM images of A) PSA, B) Nomex® and from electrospinning of 13.5 wt% PSA/DMAc, 13.5 wt% Nomex/DMAc with 4 wt% of LiCl and 3.5 wt% PLA/chloroform, respectively. Scale bars of A and B are 1 µm (of inlets are 100 nm)

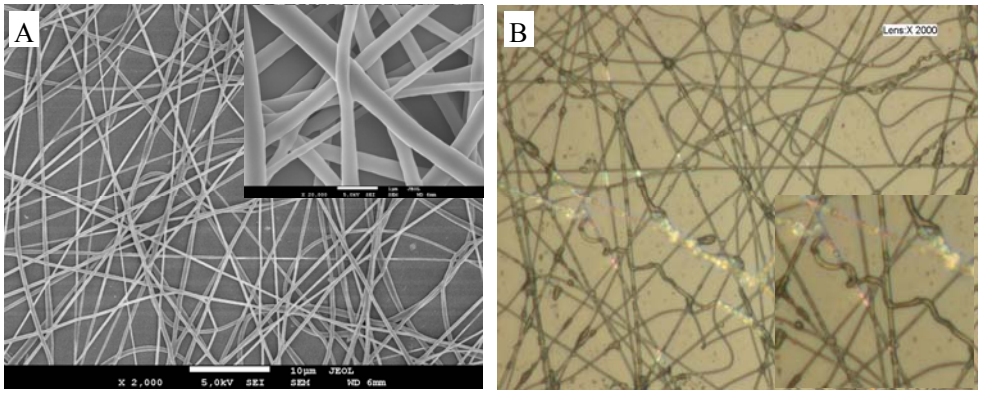

Fig 5.2.4 SEM and OPM images of TPU nanofibers A) without and B) with LiCl from electrospinning of 18 wt% TPU/DMF and 18 wt% TPU/DMF with 4 wt% of LiCl, respectively. Scale bar of A is 10 µm (inlet was 1 µm), magnification of B is 2000x

5.2.2 Formation of polymeric nanosprings by coaxial Electrospinning

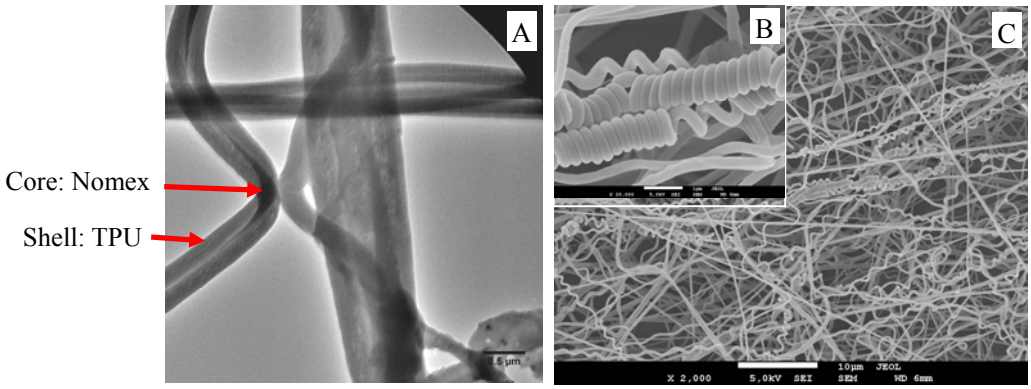

Fig 5.2.5 A) TEM and B) and C) SEM images of Nomex®/TPU core/shell nanofibers by coaxial electrospinning using 13.5 wt% of Nomex in DMAc with 4 wt% LiCl and 18 wt% of TPU in DMF/THF (3/1); The content of Nomex in the core/shell fibers was about 44%wt. Scale bars of A is 0.5 µm, B is 10 µm and C is 1 µm.

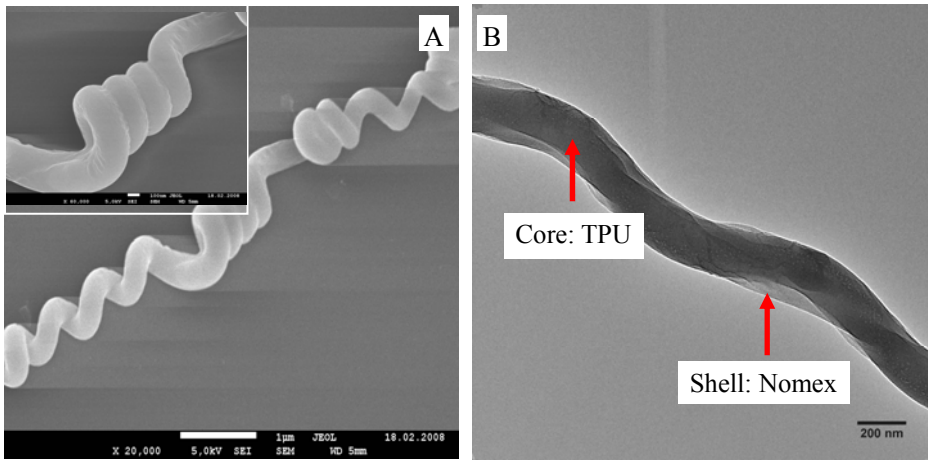

Fig 5.2.6 A) SEM and B) TEM images of TPU/Nomex® core/shell nanofibers by coaxial electrospinning using 13.5 wt% of Nomex® in DMAc with 4 wt% LiCl as core and 18 wt% of TPU in DMF/THF (3/1) as shell; The content of Nomex® in the core/shell fibers is about 44%wt. Scale bars of A is 1 µm (inlet was 100 nm) and B is 200 nm

In the following paragraphs characterization of nanofibers by a parallel arrangement of a rigid and an elastomeric compound was discussed. The setup for coaxial electrospinning is shown in **Fig 5.2.2A**. The fibers generated by coaxial

electrospinning of 13.5 wt% of Nomex® in DMAc with 4 wt% of LiCl as core and 18 wt% of TPU solution in DMF/THF of (3:1, weight ratio) (without LiCl) as shell are shown in **Fig 5.2.5**. Electrospinning was carried out at 24 kV with 15 cm distance between the electrodes. The TEM picture (**Fig 5.2.5A**) confirms the formation of a core-shell structure. The SEM pictures taken at different locations reveal helical or spring nanofibers formation although in a very non-homogeneous way. Many of the fibers are present in the form of tight nanosprings with an average fiber diameter around 250 nm (**Fig 5.2.5C**) and with spring coil diameters of about 750±10 nm. Some fibers show helical shape with a wavelength of 5–15 μm or more, which might be stretched from tight nanosprings. The same behavior was observed on exchanging the core and shell materials, i.e., using TPU as the core material and Nomex® as the shell material (**Fig 5.2.6**) using the same solutions and electrospinning conditions as described above.

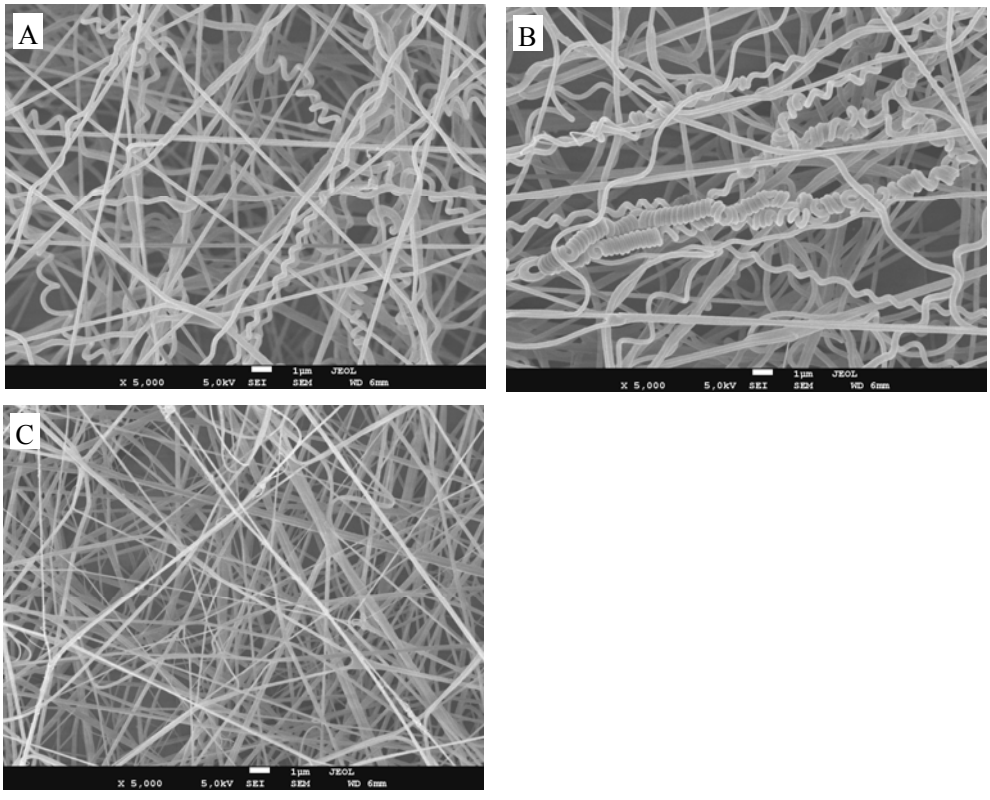

Fig 5.2.7 SEM images Nomex®/TPU core/shell nanofibers A) with 27 wt% Nomex, B) with 44wt% Nomex®, C) with 61 wt% Nomex® as core from coaxial electrospinning of 13.5 wt% Nomex in DMAc with 4 wt% LiCl and 18 wt% of TPU in DMF/THF(3/1). Scale bars are 1μm

To analyze the role of the relative amount of thermoplastic and stiff polymer components on helical or spring formation, fibers with average diameters of 130 nm (50–200 nm) were spun, for which the relative amounts of the core-shell materials were varied. Taking Nomex® as the core material, its amount relative to the shell material TPU was selected to be 0 wt% (pure TPU fiber), and 27, 44, and 61 wt% (**Fig 5.2.4A, Fig 5.2.7A–C**). Please note that in this case the relative radius of the stiff core (Nomex®) with respect to the total radii of the fibers R amounts to 0 and about 0.5, 0.66, and 0.79, respectively. Nanospring formation is absent for the 61 wt% Nomex® and TPU fibers and it is weak for the core-shell fiber with a rigid Nomex® core having a relative radius 0.79. Significant nanospring formation is observed for intermediate compositions, i.e., for relative Nomex® core radii of 0.66 and 0.5 respectively. These results clearly show that the combination of a thermoelastic polymer with a stiff polymer in core-shell fibers has a significant effect on nanospring formation as the pure materials gave none or only few nanosprings under otherwise comparable conditions. A different shrinkage behavior of the TPU and Nomex® quite obviously contributes significantly to the formation of nanosprings in bi-component fibers at least as long as both components are present in an appropriate ratio. The obvious interpretation is that a right balance has to exist between the longitudinal compressive forces arising from the shrinking thermoelastic components and the rigidity coming from the stiff component for nanospring formation.

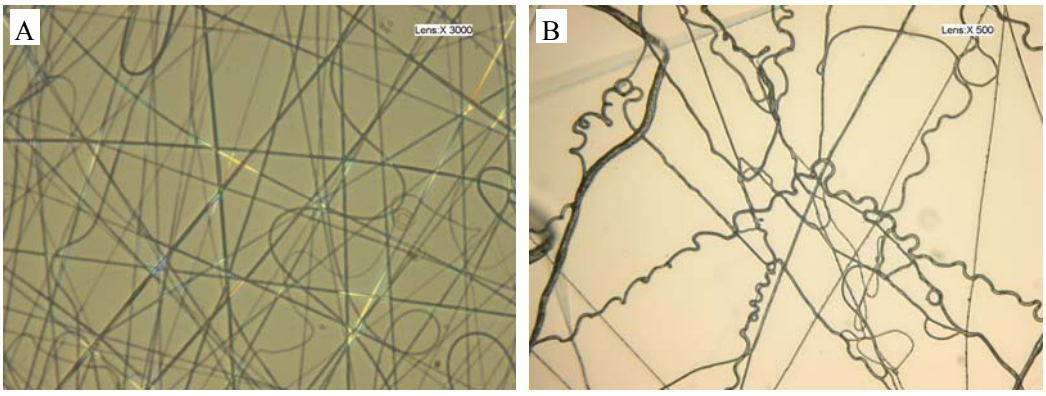

Fig 5.2.8 Optical microscope images of nanofibers by coaxial electrospinning of 4.5 wt% PLA/$CHCl_3$ as core with A) 18 wt% TPU/DMF, B) 18 wt%TPU/DMF/4 wt% LiCl as shell. The content of PLA in the core/shell fibers is about 10 wt%. Magnification of A is 3000x and B is 500x

Further, in order to find out if it is only the difference in mechanical properties of the two components combined in core-shell fibers or if the conductivity of the system also plays a significant role, coaxial electrospinning of various bi-component systems composed of a set of different rigid polymers, i.e., PLA, PSA, and TPU as flexible components were investigated with and without the addition of LiCl. Again we first investigated the electrospinning of PLA (from chloroform) and PSA (from DMAc) solution with and without LiCl, no buckling or spring formation was observed.

Bi-component electrospun fibers obtained by coaxial electrospinning of PLA or PSA solution without LiCl as core, and TPU solution without LiCl as shell yielded straight fibers as well, as shown in **Fig 5.2.8A and 5.2.9A.**

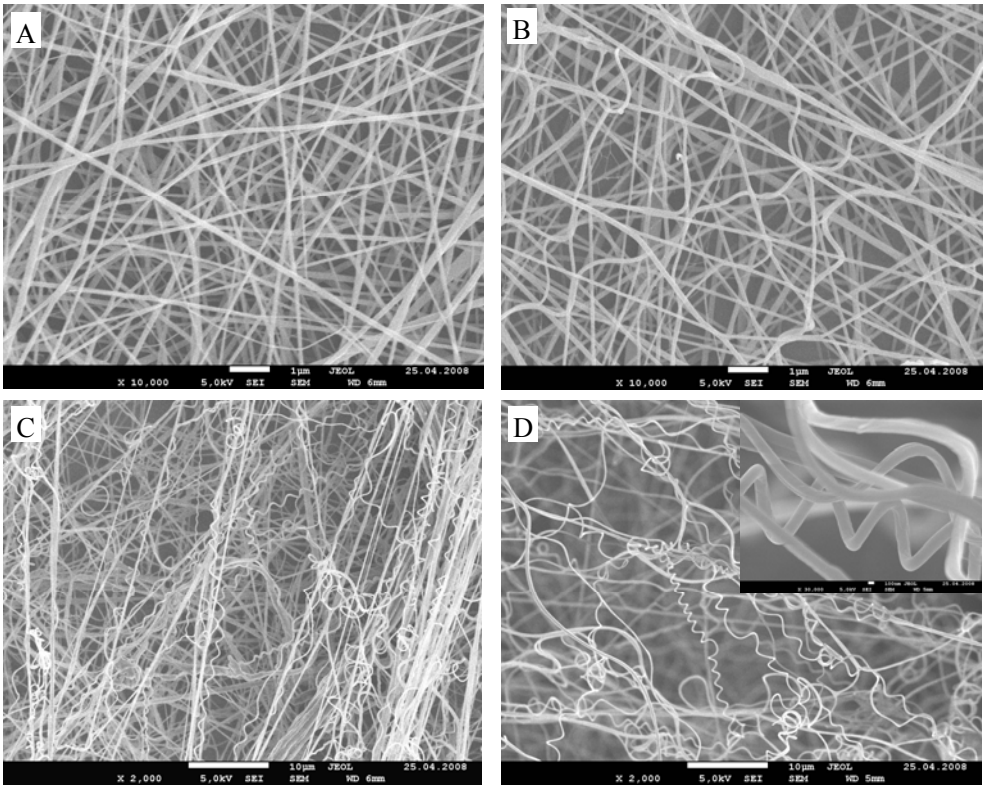

Fig 5.2.9 SEM images of core/shell nanofibers from coaxial electrospinning of 13.5 wt% PSA/DMAc with A) 0 wt%, B) 1 wt%, C) 2 wt%, D) 4 wt% LiCl content as core solution and 18 wt% TPU/DMF as shell solution. The PSA content in the core/shell fibers is about 27 wt%. Scale bars of A and B are1 µm, C and D are 10 µm (the inlet is 100 nm)

However, by addition of LiCl to the TPU component under otherwise same conditions, buckled fibers were obtained by coaxial electrospinning with PLA as core (**Fig**

5.2.8B). Similar results were obtained with PSA as a rigid component in the core and TPU as a soft shell material. Again, coaxial electrospinning TPU solution with LiCl and PSA solution without LiCl resulted in bi-component fibers with considerably stronger helical than the fibers from TPU -PLA under otherwise same conditions. The percentage of helical or spring fibers increases with increase in conductivity of solution, as shown in **Fig 5.2.9B**, **C** and **D**. That indicates that the electrical conductivity of solution plays a very important role on nanospring formation in coaxial electrospinning.

5.2.3 Formation of polymeric nanosprings by off-centered electrospinning and side-by-side electrospinning

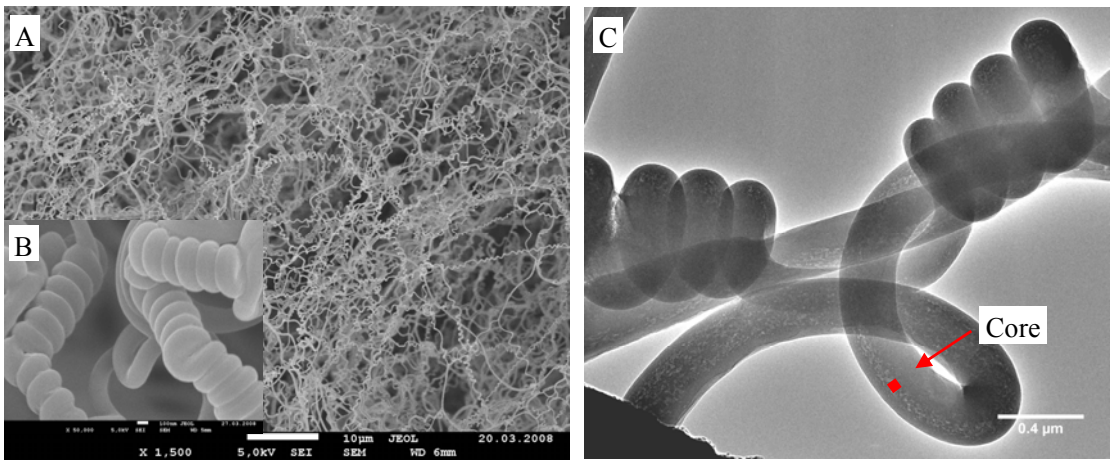

Fig 5.2.10 SEM and TEM images of Nomex®/TPU nanosprings prepared by off-centered electrospinning of 13.5 wt% of Nomex in DMAc with 4 wt% LiCl and 18 wt% of TPU in DMF, A) and B) SEM images, C) TEM image showing nanosprings from off-centered electrospinning also with core/shell structure. The weight ratio of Nomex® is about 44 wt%. Scale bar of A is 10 µm, B is 100 nm and C is 0.4 µm.

In order to further improve the efficiency of nanospring formation, off-centered electrospinning and side-by-side electrospinning were tried. Off-centered electrospinning, a slightly modified method from coaxial electrospinning with the inner tube put at one side. The setup of off-centered electrospinning is shown in **Fig 5.2.2A**. The fibers generated by off-centered electrospinning of 13.5 wt% Nomex® in

DMAc with 4 wt% LiCl as core and 18 wt% TPU solution in DMF (without LiCl) as shell are shown in the **Fig 5.2.10**. The efficiency of nanospring formation is drastically improved and visibly almost all electrospun fibers are spring or helical shape with fiber diameters around 180 ± 10 nm and spring diameter around 460 ± 10 nm. The TEM image given in **Fig 5.2.10C** shows the fiber is core/shell structure with obscure edge due to the identical solvents are used in both core and shell solutions.

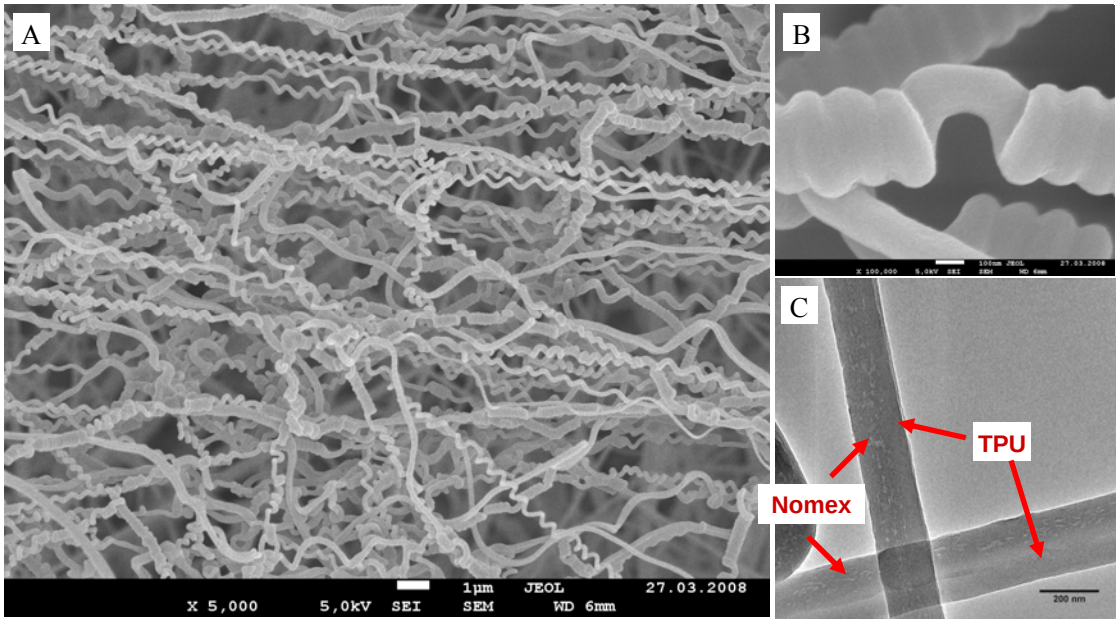

Fig 5.2.11 A) and B) SEM, C) TEM images of spring-nanofibers prepared by side-by-side electrospinning of 13.5 wt% of Nomex® in DMAc with 4 wt% LiCl and 18 wt% of TPU in DMF. The weight ratio of Nomex® is about 44 wt%. Scale bars of A is 1 µm, B is 100 nm, C is 200 nm

The side-by-side electrospinning of different polymer solutions was first reported by Gupta et al. [203], they only achieved straight fibers when applying the side-by-side technique to the bi-component system poly(vinyl chloride) and segmented polyurethane (Estane). Later, Lin et al. [145] showed the existence of a laminar structure during side-by-side electrospinning using polymer solutions of two different colors. The side-by-side electrospinning of 13.5 wt% Nomex® in DMAc with 4 wt% LiCl and 18 wt% TPU solution in DMF (without LiCl) was carried out using the apparatus shown in **Fig 5.2.2B**. The SEM images of electrospun fibers from side-by-side electrospinning are shown in **Fig 5.2.11**. The process of nanospring

formation is very efficient with almost all fibers present in SEM image are nanosprings. The fibers are thin (fiber diameter 160 ± 10 nm) with small spring diameter (380 ± 10 nm). The TEM image given as **Fig 5.2.11C** clearly shows the fibers are side-by-side structure. Switching over from conventional coaxial electrospinning to off-centered electrospinning or side-by-side electrospinning increases the efficiency of formation of nanosprings.

5.2.4 Mechanism of forming polymeric nanosprings

Buckling is common phenomena in electrospinning, it is believed to result primarily from the presence of longitudinal compressive forces acting on fluid jets, [200, 201] and high extent buckling can arouse helical, even tight spring. The longitudinal compressive forces in the bicomponent electrospinning of this work are from different shrinkage of two components. As shown in schematic diagram (**Fig 5.2.12**), coaxial electrospinning can not form spring or helical fiber at normal condition, because the elastic forces are completely offset and the longitudinal forces are nearly zero. But, the longitudinal compressive forces can be aroused by increase of electrical conductivity of solutions (core or shell), also certain content of elastic component TPU is existed to provide enough elastic forces for spring formation, as described above in **Fig 5.2.7 and Fig 5.2.9**.

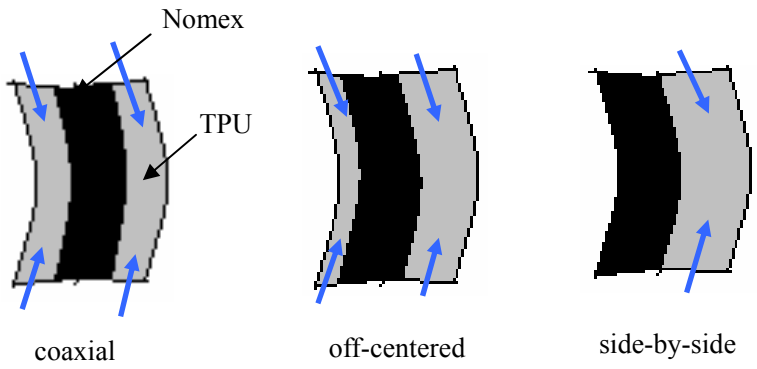

Fig 5.2.12 Schematic diagram of elastic forces of TPU component on the helical jets or nanofibers

The longitudinal compressive forces, which are applied on jets/nanofibers during different bicomponent electrospinning techniques, are side-by-side > off-centered > coaxial, due to increase of lopsided elastic forces from TPU component. The higher longitudinal compressive forces in off-centered and side-by-side structure generated more helical and tight spring fibers and kept them form destroying, as shown in SEM images of **Fig 5.2.5B, 5.2.10A and 5.2.11A**. The off-centered and side-by-side electrospinning are able to produce nearly 100% spring or helical nanofibers. Moreover, the formed spring nanofibers in off-centered and side-by-side electrospinning are more stable and most of them can be preserved by longitudinal compressive forces which are contributed by elastic force; while in coaxial electrospinning, because low longitudinal compressive forces which come from offset of elastic forces are applied on the spring nanofibers, plenty of them are stretched to straight on the way of moving to collector.

5.2.5 Mechanical properties of polymeric nanosprings

Table 5.2.2 Mechanical properties of aligned nanofiber mats with and without nanosprings

Sample	Collecting speed/ $m \cdot s^{-1}$	Tensile mechanical properties		Maximum storage modulus / GPa
		Tensile strength / MPa	Elongation / %	
Nanofiber mats with nanosprings	2	151.2	93.5	6.70
Nanofiber mats without nanosprings	16	201.9	32.5	5.15

An attempt was made to determine the mechanical properties of spring or helical nanofibers. Two kinds of aligned nanofiber mats were electrospun by side-by-side electrospinning and collected at different winding speed. One is aligned nanofibers mat which was collected at low winding speed of 2 $m \cdot s^{-1}$, which contained more than 50% aligned helical or spring nanofibers (**Fig 5.2.13A**). Due to the high conductivity of solution (4 wt% LiCl), the electrospinning jets self-bundled and highly aligned nanofiber was collected at very low winding speed, which was in accordance with the report in ref. [92] In that case, lots of spring of helical fibers retain and align in one

direction. Another case is a highly aligned nanofiber mat which was collected at high winding speed of 16 $m \cdot s^{-1}$, only composed of straight fibers (**Fig 5.2.13B**) which were stretched from spring fibers at high speed. The mechanical properties of two nanofiber mats are tabulated in **Table 5.2.2**. The stress-strain curves are shown in **Fig 5.2.13C**. Although, the tensile strength of composite aligned nanofiber mats which were collected at low winding speed of 2 $m \cdot s^{-1}$ is lower (about 151 MPa) than that collected at high speed of 16 $m \cdot s^{-1}$ (about 202 MPa), the possible reasons are attributed to loose spring or helical fibers and lack of connection between fibers. This mat displays very high elongations of around 97% due to plenty of spring or helical fibers are preserved at low winding speed, is nearly three times as that of mats from 16 $m \cdot s^{-1}$ (of 32.5%).

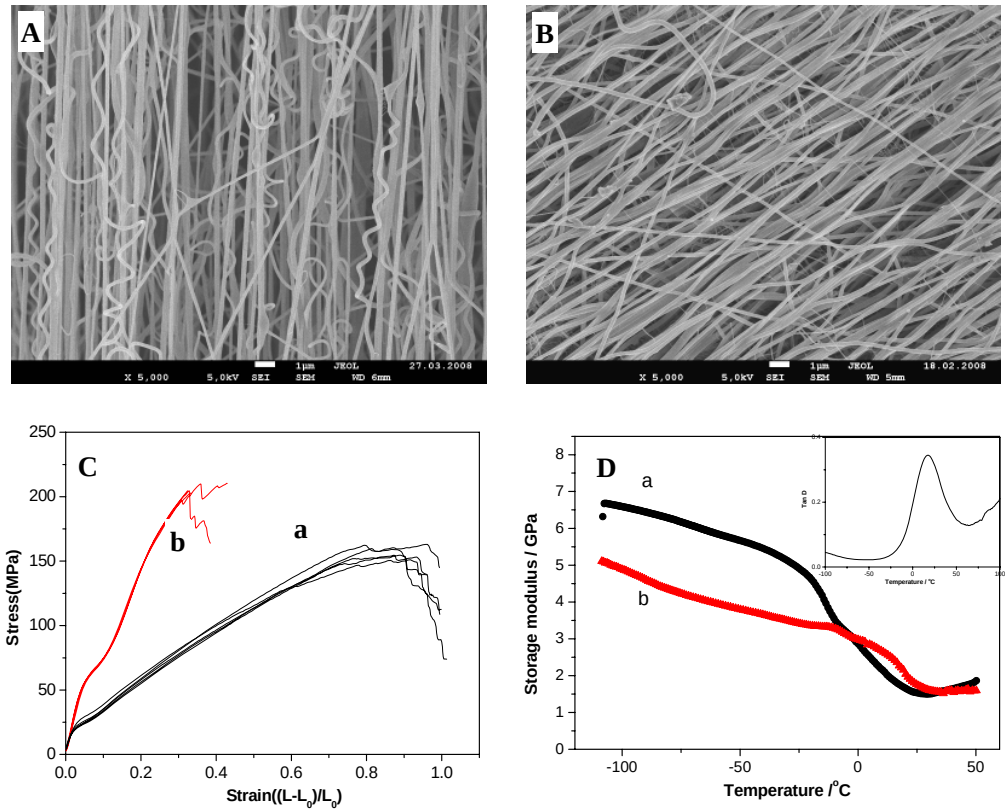

Fig 5.2.13 Upper: SEM images of Nomex®/TPU composite nanofibers prepared by side-by-side electrospinning and collected at A) 2 m/s with spring nanofibers inside and B) 16 $m \cdot s^{-1}$ without spring nanofibers; scale bars are 1 μm. Down: C) Stress-strain curve of samples A and B; D) Storage modulus-temperature curve of samples A and B, inlet is tangent curve of TPU aligned nanofiber mat.

The dynamic mechanical properties of aligned nanofiber mats with and without spring fibers are also investigated by using a Perkin-Elmer Pyris diamond analyzer, carried out under temperature ranging from -100 to 50 ℃. The aligned nanofiber mat with spring or helical fibers shows higher storage modulus than the mat that without (**Fig 5.2.13D**) below glass transition temperature T_g (about 17 ℃, as shown in **inlet of Fig 5.2.13D**).

5.3 Conclusions

With concept of curve or helix in fibers can lead to higher porosity in the fiber mat, a novel 3D porous architecture, nanospring, was designed for high performance anode structure in future MFC. Polymeric nanosprings were prepared by bicomponent electrospinning. The reasons for the formation of polymeric nanosprings were investigated by coaxial electrospinning of bicomponent rigid i.e. Nomex® or PSA (rigid) and flexible polymers i.e. TPU (flexible). The results indicated that the nanospring formation is attributed to longitudinal compressive forces which are resulted from the different shrinkages of the rigid and flexible two polymer components and a good electrical conductivity of one of the polymer solutions in coaxial electrospinning system. The modified electrospinning i.e. off-centered electrospinning and side-by-side electrospinning are much more effective than the coaxial electrospinning for generating polymer spring or helical structures, because of the higher longitudinal compressive forces which derived from the lopsided elastic forces. The aligned nanofiber mat with high percent of nanospring shows higher elongation and higher storage modulus below T_g compared to that of straight fibers. The nanospring or helical shape fibers preserves much void-space in the mat. It would be a potential architecture design for highly efficient anode in future MFCs.

6 Experimental

6.1 Materials

Name	Abbreviation	Type and Company
Poly(m-phenylene isophthalamide) chopped fibers	Nomex	Sigma-Aldrich
N,N,-dimethylacetamide	DMAc	Sigma-Aldrich
N,N,-dimethylformamide	DMF	Sigma-Aldrich
Anhydrous lithium chloride	LiCl	Sigma-Aldrich
tetrahydrofuran	THF	Sigma-Aldrich
Polylactide	PLA	Reseomer L210, Boehringer
Polyamide B24	PA	BASF
Thermal elastomer polyurethane	TPU	Desmopan DP 2590A, Bayer
Aniline		Sigma-Aldrich, purified before use
Polysulfonamide	PSA	Shanghai Synthetic Fibre Research Institute of China
Polyacrylonitrile	PAN	M_w = 210K, Dolon GmbH
Glutaric dialdehyde		25wt % in water, Sigma-Aldrich
Ethanol		Sigma-Aldrich
Sodium dihydrogen diphosphate monohydrate	$NaH_2PO_4.H_2O$	Sigma-Aldrich
Disodium hydrogen phosphate	Na_2HPO_4	Sigma-Aldrich
Ammonium chloride	NH_4Cl	Sigma-Aldrich
Potassium chloride	KCl	Sigma-Aldrich
Sodium acetate	CH_3COONa	Sigma-Aldrich
Graphite felt	GF	Weichfilz SIGRATHERM GFD, SGL Carbon GmbH Meitingen
Potassium ferricyanide	K_3 [Fe(CN)$_6$]	Sigma-Aldrich
Ammonium peroxysulfate	APS	Sigma-Aldrich
37% hydrochloric acid	37% HCl	Sigma-Aldrich
Roll paper		**ja!** Tissue Toilettenpapier, obtained from supermarket
Ion-exchange membrane		fumasep FKE, FuMA-Tech GmbH
Poly(acrylonitrile-co-itaconic acid-co-butylacrylate) (monomer ratio: 46/3/1)	PANIB	Obtained from Prof. Hou's group
Dimethylsulfoxide	DMSO	Shanghai Jinwei Chem. Corp.

6.2 Preparation of solutions for electrospinning

1) 13.5 wt% of Nomex® solution was prepared by dissolving Nomex® chopped fibers in the mixture of DMAc with 4 wt% of LiCl, stirred for 6 h at 100 ℃.
2) 18 wt% of TPU solution was prepared by dissolving TPU particles in DMF and DMF/THF (3/1, weight ratio), and was stirred for 6 h at room temperature.
3) 13 wt% of PSA solutions with different content of LiCl were prepared by dissolving PSA chopped fibers and LiCl in DMAc, and was stirred for 6 h at room temperature.
4) 4.5 wt% of PLA solution was prepared by dissolving PLA particles in $CHCl_3$, and was stirred for 6 h at room temperature.
5) 20 wt% of PA solution was prepared by dissolving Polyamide B24 in CH_3COOH/HCOOH (weight ratio of 2/1) mixed solvents, and was stirred for 6h to form a uniform solution.
6) 10 wt% of PAN solution was prepared by dissolve PAN powder (M_w=210 k) in DMF, and was stirred for 6 h at 80 ℃ to form a uniform solution.
7) 11 wt% of PANIB solution ($[\eta]_{25°C}$=2.4 $dL \cdot g^{-1}$) was prepared by mixing as-prepared 20wt % PANIB in DMSO (*from Prof. Haoqing Hou in the department of chemistry at Jiangxi Normal University*) with DMF and acetone with weight ratio of 16/15/5, and mechanically stirred for 6 h at room temperature.

6.3 Electrospinning

6.3.1 Conventional electrospinning

The electrospinning of Nomex®, TPU, PSA, PLA, PANi and PA were carried out under high voltage electrical field of 166 $kV \cdot m^{-1}$ from a positive voltage of +25 kV and negative voltage of 0 kV with distance of 15 cm. The flow rate of solution was controlled by an ejector jet pump.

6.3.2 Bicomponent electrospinning

Bicomponent electrospinning, coaxial electrospinning, off-centered electrospinning, side-by-side electrospinning, were carried out predominantly with Nomex® and TPU solutions. The setups of coaxial, off-centered and side-by-side electrospinning are shown in **Fig 6.3.1**. The nozzle for coaxial electrospinning is composed of two concentrically aligned tubes. The core tube is a stainless-steel syringe with inner and outer diameters of 0.25 mm and 0.45 mm, respectively. The shell tube is also stainless steel with inner diameter of 0.7 mm. The nozzle for off-centered electrospinning was derived from coaxial electrospinning by changing the inner tube from center to one side. The side-by-side electrospinning nozzle is composed of two side-by-side parts, separated by a very thin polyimide film as show in **Fig 6.3.B**. The electrospinning process was performed using electric fields of the order of 170 $kV \cdot m^{-1}$, from a 24 kV (+23,-1 kV) electrical potential applied to a 14 cm gap between a nozzle and collector. The two solutions were controlled by two ejector jet pumps, respectively.

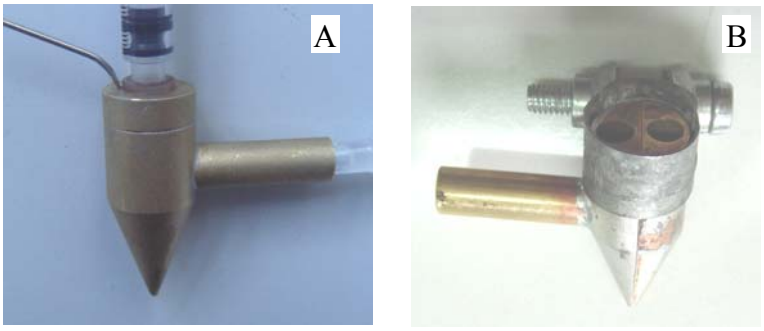

Fig 6.3.1 Setups for A) coaxial or gas assistant electrospinning and B) side-by-side electrospinning

6.3.3 Gas-assisted electrospinning

The precursor ultrafine fibers were made by using home-made gas-assisted electrospinning (GE-spinning) spinneret. *(H.Q. Hou; S.L. Chen; C.Y. Cheng; P. Hu, High-speed air-blowing static spinning composite preparation method and device for ultra-fine polymer fiber, Chinese patent CN20071009595 20070925).* The electric field used for the GE-spinning was of the order of 40 $kV \cdot m^{-1}$: a 40 kV electrical

potential was applied across a 100 cm gap between the spinneret and the collector. The airflow speed at the outlet of the nozzle was about 100 $m \cdot s^{-1}$ supplied by using an air-compressor with a power of 260 $L \cdot min^{-1}$. The fibers were collected by a drum with low rotating speed of about 1 $m \cdot s^{-1}$.

6.3.4 Layer-by-layer electrospinning

Roll papers (made from natural cellulose) were divided into separated layer. 10% polyacrylonitrile (PAN) solution in DMF was layer-by-layer electrospun on separated roll paper layer one-by-one, under electric filed of the order of 60 $kV \cdot m^{-1}$ from a 10kV (+10, 0kV) electrical potential applied to a 20 cm gap between a nozzle and collector. Each PAN fiber layer was electrospun for about 5 min. Three-dimensional PAN/NC composite fiber mats with ten layers were prepared. All mat samples were dried in vacuum at temperature of 60 ℃ to remove residual solvent for further investigation.

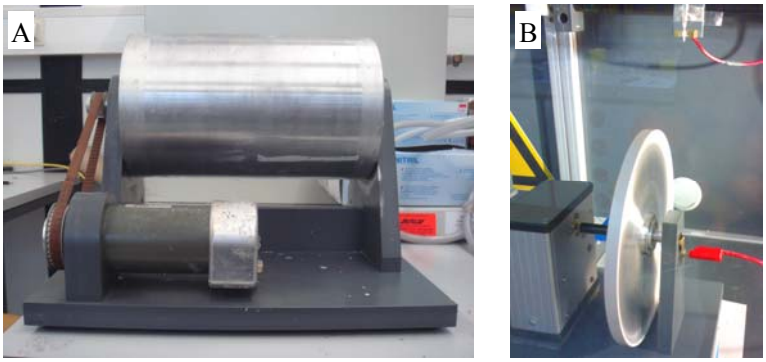

Fig 6.3.2 Digital pictures of fiber collecting setups of A) rotating drum for non-aligned fiber mats and B) rotating disc for highly aligned fiber belts

6.3.5 Fiber Collection

Non-aligned nanofiber mats were collected as by a drum (**Fig 6.3.2A**) at low rotating speed of 0.5 $m \cdot s^{-1}$, which can transitionally move, and of highly aligned belts by a disc (**Fig 6.3.2B**) with diameter of 0.2 m and rim of 10 mm at high collecting speed of 15 $m \cdot s^{-1}$. All electrospun fiber samples were dried in vacuum at temperature of 60 ℃ to remove residual solvents for further investigation.

6.4 Carbonization of electrospun PAN and PANIB fiber

The stabilization and carbonization of PAN and PANIB electrospun fibers were conducted in a tubular stainless steel reactor (with interior diameter 50 mm and effective heating length 500 mm)

The stabilization and carbonization of PAN electrospun fiber mat was following steps: 1) In air atmosphere, heating up to 230 ℃ from room temperature at a rate of 1 ℃·min^{-1}, and annealing for 3 h to finish the stabilization process; 2) In N_2 atmosphere, heating up to 500 ℃ at rate of 2 ℃·min^{-1}, and annealing for 1h, then heating up to 900 ℃ at rate of 5 ℃·min^{-1} and annealing for 1h.

The stabilization and carbonization process of PANIB porous fiber mesh was performed in a high-temperature furnace using the following protocol: 1) heating up to 230 ℃ at a rate of 20 ℃·min^{-1} in air and annealing for 2h for a stabilization process of the precursor ultra-fine fibers; 2) heating up to 350 ℃ at a rate of 5-10 ℃·min^{-1} in nitrogen atmosphere and annealing at 350 ℃ for 20 min; 3) heating up to 750 ℃ at a rate of 3-5 ℃ /min in nitrogen atmosphere and annealing at 750 ℃ for 20 min; 4) heating up to 1000 ℃ at a rate of 3-5 ℃·min^{-1} in nitrogen atmosphere and annealing at 1000 ℃ for 1 h to complete the carbonization process.

6.5 Electron microscopic characterization

SEM images were obtained from JSM-7500F scanning electronic microscope, with a voltage of 5 kV. The dried electrospun nanofiber mats were directly stuck on a holder with conductive tape. Non-conducting samples were coated with a layer of gold to increase conductivity, while conducting samples such as carbon and polyaniline, were directly observed without coating with gold.

TEM images were taken from JEM-3010 transmission electronic microscope, under acceleration voltage of 300 kV. The fiber samples were directly electrospun on copper grids. All samples were dried at 50 ℃ under vacuum before observation.

6.6 Thermal analysis

The Thermal stability was determined by using a Mettler thermal analyzer 851 Thermogravimeter in air and nitrogen atmosphere (flow rate was 50 $mL \cdot min^{-1}$) in the temperature range of 25-800 ℃ at heating rate of 10 $℃ \cdot min^{-1}$, sample weight of about 10 mg was used in each experiment.

6.7 X-ray diffraction analysis

The X-ray diffraction analysis (XRD) spectra of was performed under SIEMENS Diffraktometer D5000, the scattering angle (2θ) was varied from 5^o to 40^o, average measuring time was set to be 24 h. Samples of highly aligned fibers mats were held by aluminum plate.

6.8 Determination of thickness of nanofiber mats

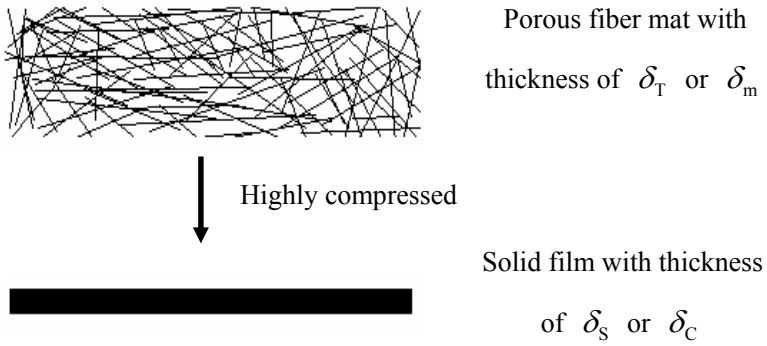

Fig 6.3.3 Schematic diagram of calculating thickness of fiber mat

For porous electrospun fiber mat sample, the measurement of thickness was a big challenge. The measured thickness δ_m or total thickness δ_T, which was measured by micrometer, SEM, or thickness meter. But this thickness was not the real thickness of mat, and it would be varied with change of porosity in the mat, because the mat was composed of nanofibers and containing high content of void-space. Herein, another thickness determining method, calculated thickness δ_C, was introduced to evaluate

the thickness of electrospun nanofiber mat. This thickness was calculated according to the weight and density following the ref [97], which was

$$\delta_C = \frac{V_S}{S} = \frac{m}{\rho \cdot S} \tag{6.8-1}$$

where V_S is the solid volume, ρ is the density of material, S and m are the area and mass of the sample, respectively. The δ_C was same as the thickness of a "film", which was highly compressed from the mat, without any void-space, it also can be called solid thickness δ_S, see in **Fig 6.3.3**.

For the Nomex®/TPU composite fiber mats, the weight of sample is taken by subtracting the weight of LiCl. The density of sample ρ_a is the average density of the Nomex® and TPU with corresponding ratio, which can be defined as:

$$\rho_a = \varphi_N \rho_N + \varphi_T \rho_T \tag{6.8-2}$$

where φ_N and φ_T were the weight percent of solid Nomex® and TPU in the composite nanofiber, respectively. φ is equal to the product of the weight of solution M and its mass concentration C, that can be defined as,

$$\varphi = M \cdot C \tag{6.8-3}$$

Because the densities of Nomex®/DMAc and TPU/DMF solutions are close to 1, the difference between the mass and volume of solution is small. So, the mass of solution M could be replaced by its volume V. So, the Eq. 6.8-2 becomes:

$$\rho_a = \frac{C_N V_N \rho_N + C_T V_T \rho_T}{C_N V_N + C_T V_T} \tag{6.8-4}$$

The volume of solution was determined by the flow rate, which is controlled by pump. The densities of Nomex® and TPU are 1.38 g·cm^{-3} and 1.205 g·cm^{-3}, respectively. If the actual weight of sample with area of S is m, then the final equation for the thickness $\delta_{Nomex/TPU}$ of samples is

$$\delta_{Nomex/TPU} = \frac{m}{S \cdot \rho_a} = m \Big/ \left(S \cdot \frac{C_N V_N \rho_N + C_T V_T \rho_T}{C_N V_N + C_T V_T} \right) \quad (6.8\text{-}5)$$

For the PA/PANi composite nanofiber mats, the thickness calculation was

$$\delta_{PA/PANi} = \frac{m}{S \cdot \rho_a} = \frac{m}{S \cdot \left(\varphi_{PANi} \rho_{PANi} + \varphi_{PA} \rho_{PA} \right)} \quad (6.8\text{-}6)$$

where φ_{PANi} and φ_{PA} are the weight percentage of PANi and PA, respectively.

6.9 Mechanical properties measurement

The tensile strength and modulus of the electrospun nanofiber were measured using a Zwick/Roll with stretching model. The samples for tensile test were prepared with dimensions of 8 mm wide and 60 mm long. The sample was directly mounted to the sample clamps and stretched at a speed of 20 mm·min^{-1}. The curves of stress versus strain were recorded. An average value was got from five times measurements of every sample for final results. The thickness of samples was measured by calculating according to Eq. 6.8-5 and 6.8-6 in **Experimental part 6.8**. All tensile test measurements were performed at 25 ℃.

The dynamic mechanical analysis (DMA) of aligned fiber belts was performed by Ping Hu in the Group of Prof. Haoqing Hou at the department of chemistry in Jiangxi Normal University, using a Perkin-Elmer Pyris diamond analyzer with a heating rate of 3 ℃·min^{-1} in nitrogen atmosphere. The applied frequency and amplitude were 1 Hz and 20 μm, respectively. The storage modulus (E'), loss modulus (E''), and loss tangent (tan δ) of aligned fiber mats were recorded in the temperature range from -100 to 50 ℃.

6.10 Electrical conductivity measurement

The electrical conductivities of non-aligned composite nanofiber mats were calculated from their resistances which were measured by four-probe method using Keithley 2000 multimeter at room temperature, as shown in **Fig 6.3.4A**. The thickness of mat

was calculated from weight and density following Eq. 6.8-6 in **Experimental part 6.8**. Carrying out the integration between the inner probe tips (where the voltage is measured), see in **Fig 6.3.4B.**

$$R = \int_{x_1}^{x_2} \varepsilon \cdot \frac{dx}{2\pi x \delta} = \int_{s}^{3s} \frac{\varepsilon}{2\pi\delta} \cdot \frac{dx}{x} = \frac{\varepsilon}{2\pi\delta} \cdot \ln(x) \Big|_{s}^{3s} = \frac{\varepsilon}{2\pi\delta} \cdot \ln 3 \qquad (6.10\text{-}1)$$

where δ is the thickness of sheet, ε is electric resistivity,

So, the resistivity is

$$\varepsilon = \frac{2\pi R\delta}{\ln 3} \qquad (6.10\text{-}2)$$

And the conductivity is

$$\sigma = \frac{1}{\varepsilon} = \frac{\ln 3}{2\pi R\delta} = \frac{0.17485}{R\delta} \qquad (6.10\text{-}3)$$

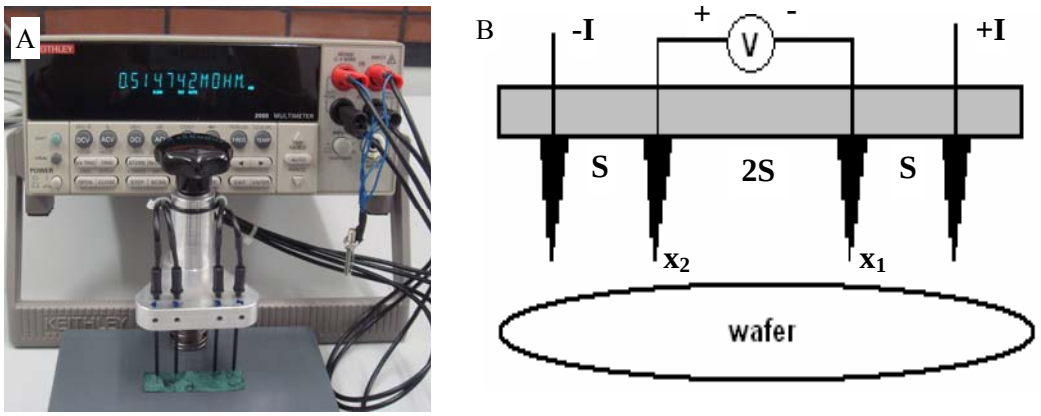

Fig 6.3.4 A) setup and B) schematic diagram for electrical conductivity measurement of fiber mats

6.11 Bacteria compatibility test

Bacteria compatibility of PA/PANi composite nanofiber mat was tested by qualitative and quantitative ways. In qualitative way, a piece of PA/PANi fiber mat was put on agar plate with Tryptic Soy Broth (TSB) nutrition, then inoculated with *Escherichia coli (E.coli)* and incubated at 37 ℃ for 16-20 h. In a quantitative way, two bottles of standard TSB solution (30 $g.L^{-1}$) with the same volume were prepared, same volume of overnight *E.coli* culture which had been incubated in standard TSB solution at 37

℃ was inoculated in both bottles. A piece of PA/PANi fiber mat was put into one of the bottles. Then, the two bottles were incubated at 37 ℃, and sampled the solutions at different time to check the optical density (OD) using spectrophotometer at 578 nm. The OD values from the two solutions were compared to evaluate the bacteria compatibility of PA/PANi composite nanofiber mat.

6.12 Growth of nano-fibrillar PANi on electrospun polyamide nanofibers by rapidly mixing polymerization

Reactions were carried out in 80 ml beaker. Typically, an aqueous solution of aniline in 20 ml of 1M HCl doping acid and another solution of ammonium peroxysulfate in 20 ml and same doping acid as oxidant were prepared. Rapidly mixed the two solutions by pouring them together and immediately stirred or shook to ensure sufficient mixing before polymerization begins. The molar ratio of aniline/oxidant was 4/1. Then stopped stirring or shaking and nanofiber mats were put into the mixed solution swiftly. After reacting for about 12 h, the nanofiber mats were washed three times by using distilled water and dried under vacuum at 50 ℃ for further characterization.

6.13 Electrode connection

For the electrodes in half-cell experiments, 2D-CFM, 3D-CFM or commercial graphite felt (Weichfilz, SIGRATHERM, SGL Carbon GmbH, Meitningen, Germany) was cut into pieces of 1 × 2 cm^2 and glued onto graphite foil paddles - which served as inert electrode backbone material - using a three-component resin (Expoydharz L, Harter S and carbon black with ratio of 10/4/1) mixed with carbon black, which one side was available for growth of biofilms and for current density calculation. The graphite foil paddles were connected with a piece of stainless steel wire to the outer circuit.

For the electrodes in full-cell experiments, the anode - porous 3D-ECFM with size of

about 2×2.5 cm^2 and weight of about 0.017 g - was fixed in a stainless steel needle plate, both sides of mat were available for growth of biofilms and used for current density calculation.

6.14 Half-cell and full-cell experiments

All half-cell electrochemical experiments were carried out under potentiostatic control in one chamber cell, using a three-electrode arrangement consisting of working electrode, an Ag/AgCl reference electrode (sat. KCl, 0.195 V vs. SHE, Sensortechnik, Meinsberg, Germany) and a graphite plate counter electrode (size of 4×5 cm^2). The experiments were conducted under control of a potentiostat (Autolab PGSTAT30, Ecochemie, Netherlands). The potentiostat was equipped with five additional array modules which allowing the simultaneous investigation of up to six working electrodes in connection with counter electrode and one reference electrode. All electrodes were put in one chamber, 0.2 V (vs. Ag/AgCl) was applied on working electrode by potentiostat (Autolab), recorded the current in real time (see in **Fig 6.3.4A**).

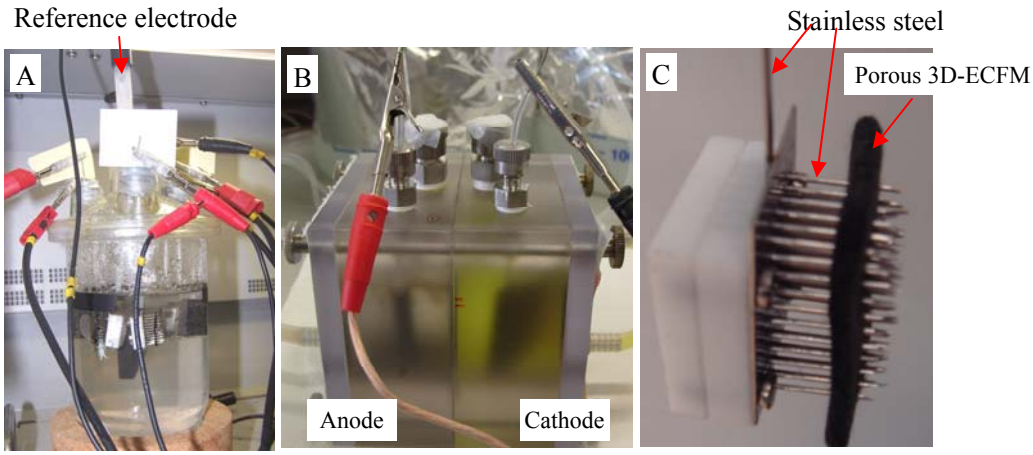

Fig 6.3.5 Setups of A) half-cell controlled by potentiostat with three-electrode electrochemical system, B) full-cell system and C) electrode connection in full-cell system.

All fuel-cell experiments were carried out in batch mode using two-chamber cube MFCs,[15] see in **Fig 6.3.5B**. The two chambers were separated by an ion-exchange

membrane (fumasep FKE). The anode was porous 3D-ECFM with size of 2×2.5 cm^2 and two sides were available. Inoculated artificial wastewater with 10 mM sodium acetate as substrate served as medium in the anode. The cathode was graphite plate with size of 4×5 cm^2 (both size available) and 100 mM ferricyanide in 50 mM phosphate buffer solution (PH=7.0) served as catholyte.

All experiments were conducted at 35 ℃ with magnetic stirring.

6.15 Density and porosity of fiber mats

The density of fiber mat ρ_{T} is calculated from the mass and total volume V_T of fiber mat.

$$\rho_{\mathrm{T}} = \frac{m}{V_T} = \frac{m}{S \cdot \delta_T} \tag{6.15-1}$$

where *m* and *S* are mass and area fiber mat, respectively, δ_T is measuring thickness of fiber mat.

Porosity is a measure of the void spaces in a material, and is a fraction of the volume of voids over the total volume, between 0–1, or as a percentage between 0–100%. The term is used in multiple fields including pharmaceutics, ceramics, metallurgy, materials, manufacturing, earth sciences and construction. The porosity of a porous medium (such as rock or sediment) describes the fraction of void space in the material, where the void may contain, for example, air or water. It is defined by the ratio:

$$\phi = \frac{V_V}{V_T} = \frac{V_T - V_S}{V_T} = 1 - \frac{V_S}{V_T} \tag{6.15-2}$$

where V_V is the volume of void-space, V_S is volume of solid, V_T is the total or bulk volume of material which including the solid and void volume. For a piece of nanofiber mesh with area of S ,

Because

$$V = S \cdot \delta \tag{6.15-3}$$

So

$$\phi = 1 - \frac{V_S}{V_T} = 1 - \frac{S \cdot \delta_S}{S \cdot \delta_T} = 1 - \frac{\delta_S}{\delta_T} \tag{6.15-4}$$

where δ_S is solid thickness of nanofiber mesh (**Experimental part 6.8**), δ_T is total thickness of nanofiber mesh (solid and void), which can be measured by micrometer or microscope. But for super high porosity materials (>95%), it is difficult to distinguish the porous property by the porosity value.

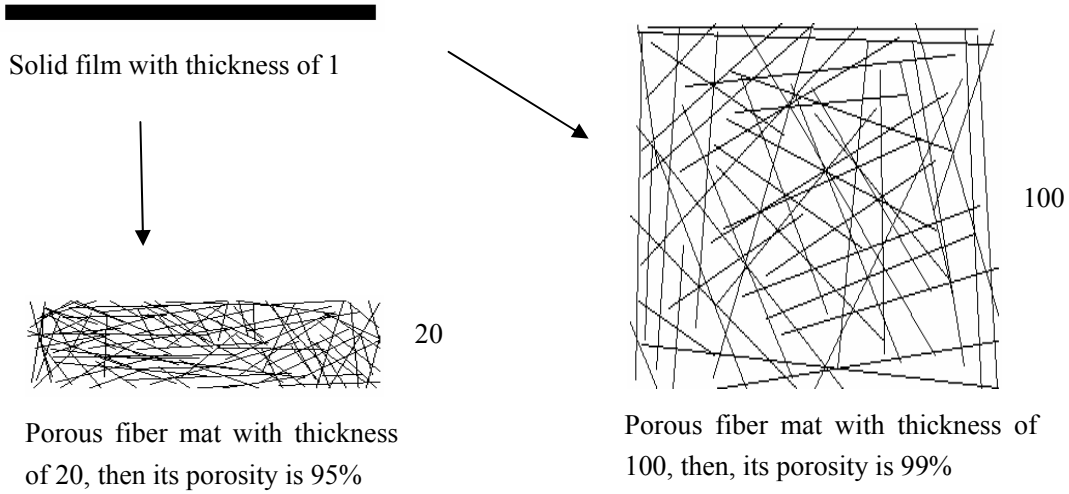

Fig 6.3.6 Schematic diagram porous index of fiber mat

So, we define porous index PI as ratio of $\frac{V_T}{V_S}$ or $\frac{\delta_T}{\delta_S}$. The PI of material with porosity of 95% is 20, while the PI of material with porosity 99% is 100. That means that, as shown in **Fig 6.3.6**, if a piece of solid film with area of *S*, and thickness of 1, then this film is used to make electrospun fiber mat with same area of *S*. When the thickness of fiber mat is 20, it contains 95% porosity, similarly, when the thickness of fiber mat is 100, it contains 99% porosity. The porosity value of 95% and 99% differs not so much, but the thickness of these materials with such porosity differs five times,

see in **Table 6.15.** And if the porosities of materials are 99% and 99.5%, only the 0.5% difference in porosity value, but their porous indexes are 100 and 200, shows great difference.

Table 6.15 Comparison table of porosity and porous index PI

Porosity	Porous index (*PI*)
80%	5
90%	10
95%	20
98%	50
99%	100
99.5%	200
99.8%	500
99.9%	1000

6.16 Pore size measurement

The pore size in the electrospun fiber mats was measured by a Capillary Flow Porometer (PMI, CFT-1200AEXL) using Dry Up/Wet Up method. A wetting liquid is allowed to spontaneously fill with the pores in the sample and a non-reacting gas is allowed to displace liquid from the pores. The gas pressure and the flow rates through wet and dry samples are accurately measured. The gas pressure which is required to remove liquid from the pores and cause to flow is given by:

$$D = 4\gamma \cos\theta / p \qquad (6.16\text{-}1)$$

where D is the pore diameter, γ is the surface tension of liquid, θ is the contact angle of liquid, and p is the differential gas pressure. From measured gas pressure and flow rates, the pore throat diameter, pore size distribution, and gas permeability are calculated.

6.17 Measurement of surface area

The specific surface area of PA/PANi composite PCNMs were measured by BET

method with N_2 as absorption. The BET measurement was carried out on Gemini V2.00 (Micromeritics Instument Corp.) with sample weight of bout 0.017g.

The surface area of porous 3D-ECFM was calculated from fiber diameter and material density. Because in MFCs, the small pores on the fiber surface (smaller than 200 nm, the size of microorganisms) will be clogged and can not be used by microorganisms. So, the specific surface area measured by BET makes no sense to the electricity generation in MFCs. We define a projected specific surface area S_P which is the surface area of fiber with ideal smooth surface. It can be calculated from fiber diameter, mass and density of material. Two fibers with different diameter of d_1 and d_2, and length of l_1 and l_2, are made from same material with same volume V and density ρ ,

$$V = \frac{\pi}{4} d_1^2 l_1 = \frac{\pi}{4} d_2^2 l_2 \qquad (6.17\text{-}1)$$

$$V = \frac{m}{\rho} \qquad (6.17\text{-}2)$$

The surface area ratio of the two fibers is

$$\frac{S_1}{S_2} = \frac{\pi d_1 l_1}{\pi d_2 l_2} \qquad (6.17\text{-}3)$$

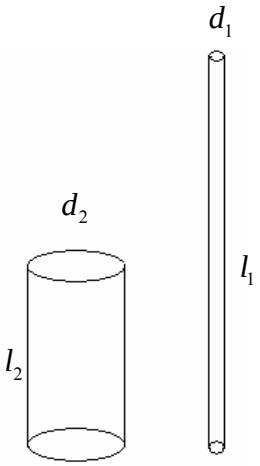

Combined Eq. 6.17-1 and Eq. 6.17-3

$$\frac{S_1}{S_2} = \frac{l_2}{l_1} \qquad (6.17\text{-}4)$$

Eq. (6.17-4) means that the surface area ratio is inversely proportional to the fiber diameter ratio. The diameter of fibers in graphite felt is about 10 μm, S_P is about 0.2 $m^2 \cdot g^{-1}$, whereas in the porous ECFM is around 1μm, S_P is 2 $m^2 \cdot g^{-1}$. So, the S_P of the porous ECFM is about 10 times than that in graphite felt.

6.18 Microorganism acclimation procedure

5 ml sludge (Braunschweig wastewater plant) was added to 160 ml artificial waste

water; and the solution served as anolyte in a full fuel cell, loaded 1000 Ω between anode and cathode. The anolyte was refreshed every 48 h. After about 4 days acclimation, this MFC served as the microorganism source for the following measurements. In each experiment, 10ml of old medium (with microorganism) was taken from above MFC and added in fresh medium. The components of the artificial waste water are: $NaH_2PO_4.H_2O$ (2.69 $g \cdot L^{-1}$), Na_2HPO_4 (4.33 $g \cdot L^{-1}$), NH_4Cl (0.31 $g \cdot L^{-1}$), KCl (0.13 $g \cdot L^{-1}$), CH_3COONa (10 mM), 12.5 ml trace metal and 12.5 ml vitamin solution.[204] [205]

6.19 Biofilm fixation and dehydration

The fixation and drying of biofilm samples were prepared as follows: firstly samples were fixed by 5 wt% glutaric aldehyde in 0.05 M phosphate buffer solution (PH=7.0); then samples were dehydrated in a graded series of aqueous ethanol solution (10%, 25%, 40%, 55%, 70%, 80%, 90% and 100%), stored in each for about 1 h, and then taken out and let naturally dry at room temperature. Finally the samples were coated with a layer of gold and examined under JSM-7500F scanning electron microscope.

6.20 Fiber diameter measurement

The fiber diameter was measured from the SEM images. The average fiber diameter was calculated from diameters values of at least 50 fibers.

Zusammenfassung

Eine neuartige poröse leitfähige Nanofasermatte mit Polyanilin auf der Faseroberfläche wurde durch einfache oxidative Polymerisation erfolgreich hergestellt. Das Kompositmaterial zeigte eine Kern-Schale-Struktur mit einer sehr hohen Oberflächenrauigkeit. Sowohl die Zusammensetzung als auch die Dicke der Polyanilinschicht konnten durch Variation der Anilinkonzentration und der Temperatur kontrolliert eingestellt werden. Die Kombination der Vorteile sowohl des Elektrospinn-Verfahrens als auch des Nano-Polyanilins führte dazu, dass das Kompositmaterial aus Polyamid und Polyanilin mehr als fünf gute Eigenschaften besitzt. Dazu gehören eine hohe Leitfähigkeit von 6.759 $S \cdot m^{-1}$, eine hohe spezifische Oberfläche von 160 $m^2 \cdot g^{-1}$, eine Zugfestigkeit von 82.88 MPa für eine unorientierte Fasermatte bzw. 161.75 MPa für orientierte Fasern, gute thermische Eigenschaften, ein Massenverlust von 5% wird erst bei einer Temperatur von 415 °C beobchtet. Das material zeigt außerdemeine exyellente Biokopatibilität. In dem Kompositmaterial aus Polyamid/Polyanilin ist das Polyanilin die einzige leitfähige Komponente, die in trockenem Zustand gemessene Leitfähigkeit von 6.759 $S \cdot m^{-1}$ ist nicht ausreichend für eine Anwendung als Elektrode in mikrobiellen Brennstoffzellen (MFC). Zusätzlich nimmt die Leitfähigkeit in pH- neutraler Umgebung aufgrund von Deprotonierung ab. Dennoch ermöglicht die Methode des spontanen Aufwachsens von nanostrukturiertem Polyanilin auf elektrogesponnenen Fasern die Herstellung elektrisch leitfähiger poröser Fasermatten. Die Kombination der Vorteile von elektrogesponnenen Fasern mit nanostrukturiertem Polyanilin erweitert die Anwendungsmöglichkeiten auf weitere Gebiete, wie Chemo- oder Biosensoren, Aktuatoren, Katalyse, elektromagnetische Abschirmungen, Korrosionsschutz, Trennungsmembranen, elektro-optische Bauteile, elektrochrome Bauteile, Gewebezüchtung und viele andere.

Aufgrund der für die Anwendung in mikrobiologischen Brennstoffzellen nicht

ausreichenden Leitfähigkeit der Polyamid/Polyanilin-Komposite wurden in der Folge elektrogesponnene Kohlenstoffasern mit hoher Leitfähigkeit und Umweltstabilität untersucht. Die erreichbare Stromdichte in mikrobiologischen Brennstoffzellen hängt wesentlich von der Besiedelungsdichte der Mikroorganismen an der Anode ab. Es wurden zweidimensionale elektrogesponnene Kohlenstoffasermatten hergestellt, die aber aufgrund der geringen Porengröße und geringen Porosität nur ein Wachstum der Mikroorganismen in einer dünnen Lage auf der Oberfläche ermöglichten. Um nun die Leistungsdichte durch Erhöhung der Bewuchsdichte auf der Fasermatte zu vergrößern, wurden zwei verschiedene Ansätze zur Herstellung einer dreidimensionalen Faserstruktur entwickelt: Faserkonstrukte mit einer größeren Porosität und mehrlagige Systeme.

Die durch druckluftunterstütztes Elektrospinnen hergestellten Faserkonstrukte zeigten einen Faserdurchmesser von ca 1 µm, eine stabile hochporöse Struktur mit einer Porosität von 99%, eine Porengröße von ca. 5,8 µm innerhalb der Matte sowie eine sehr geringe Dichte von 18 $kg \cdot m^{-3}$. Die daraus hergestellte dreidimensionale Anode erwies sich als sehr geeignet für das Aufwachsen von mikrobiellen Biofilmen und ergab eine hohe geometrische Stromdichte von 3.0 $mA \cdot cm^{-2}$, sowie eine sehr hohe massenbezogene Stromdichte von 714 $mA \cdot g^{-1}$. Die durch Layer-by-Layer-Elektrospinnen hergestellten Systeme zeigten eine Porosität von 98.5 %, die vorwiegend durch die Hohlräume zwischen den einzelnen Lagen verursacht wird, sowie eine große Oberfläche aufgrund der dünnen elektrogesponnenen Kohlenstoffasern in jeder Schicht. Dieser Aufbau ist geeignet zum schichtweisen Aufwachsen von Biofilmen und ergab eine geometrische Stromdichte von 2.0 $mA \cdot cm^{-2}$ und eine massenbezogene Stromdichte von 294 $mA \cdot g^{-1}$.

Obwohl sowohl die Porosität als auch die Porengröße ausreichend groß sind, um eine Durchlässigkeit für einzelne Mikroorganismen zu ermöglichen, führt die Tendenz zur Bildung von Biofilmen und die neben anderen Faktoren dadurch verringerte Durchlässigkeit z.B. für Nährstoffe dazu, das ein Wachstum nur innerhalb einer Schicht von einigen hundert Mikrometern und nicht innerhalb der gesamten Struktur erfolgt. Die hier erhaltende Stromdichte an der Anode könnte durch weitere

Verbesserungen wie Erhöhung der Porosität oder den Einbau von Kanälen für eine ausreichende Nährstoffversorgung innerhalb der Struktur noch erhöht werden.
Aus den oben beschriebenen Ergebnissen wird deutlich, das die Porengröße und die Porosität der als Trägermaterial verwendeten Fasermatte von größter Bedeutung für ihre Leistungsfähigkeit als Anode in mikrobiellen Brennstoffzellen sind. Um diese zu verbessern, wurde ein Ansatz gewählt, bei der eine höhere Porosität der Strukturen durch die Verwendung helicaler bzw. federartiger Faserstrukturen erreicht wurde, diese könnten in zukünftigen mikrobiellen Brennstoffzellen zur Anwendung kommen.

Die helicalen Faserstrukturen wurden durch Zweikomponenten-Elektrospinnen hergestellt. Der Prozess wurde mittles unterschiedlicher Polymerzusammensetzungen genauer untersucht. Hierzu wurde ein starres Polymer wie Nomex® oder PSA mit einem flexiblen Polymer wie TPU koaxial versponnen. Die Ergebnisse zeigten, das die Bildung der helicalen Faserstrukturen auf kompressiven Kräften beruht, die aus der unterschiedlichen Schrumpfung der beiden Polymerkomponenten herrühren, sowie auf einer guten elektrischen Leitfähigkeit einer der Polymerlösungen im koaxialen Spinnprozess. Durch eine Veränderung des Spinnaufbaus, beispielsweise eine nicht zentrische Anordnung der Spinndüsen oder durch direkt nebeneinander angeordnete Düsen, konnten helicale oder federartige Strukturen wesentlich effektiver erhalten werden. Dies lässt sich durch größere longitudinale Kompressionskräfte erklären, die durch einseitige Elastizität verursacht werden. Orientierte Fasermatten mit einem hohen Anteil an Nanofedern zeigten im Vergleich zu Fasermatten ohne diese eine größere Dehnbarkeit und ein höheres Speichermodul unterhalb der Glastemperatur. Die helicalen oder federartigen Faserstrukturen lassen viel Freiraum innerhalb der Fasermatte, was sie für eine Anwendung als Anode in zukünftigen mikrobiellen Brennstoffzellen interessant macht.

Summary

A novel porous conducting nanofiber mat (PCNM) with nanostructured polyaniline (nanoPANi) on the fiber surface was successfully prepared by simple oxidative polymerization. The composite PCNM displayed a core/shell structure with highly rough surface. The thickness and the morphology of PANi layer on the electrospun polyamide (PA) fiber surface could be controlled by varying aniline concentration and temperature. The combination of the advantages of electrospinning technique and nanostructured PANi, let the PA/PANi composite PCNM possess more than five good properties, i.e. high conductivity of 6.759 $S \cdot m^{-1}$, high specific surface area of 160 $m^2 \cdot g^{-1}$, good strength of 82.88 MPa for mat and 161.75 MPa for highly aligned belts, good thermal properties with 5% weight loss temperature up to 415 ^oC and excellent biocompatibility. In the PA/PANi composite PCNM, PANi is the only conducting component, its conductivity of 6.759 $S \cdot m^{-1}$ which is measured in dry-state, is not enough for electrode. Moreover, the conductivity decreases in neutral pH environment due to the de-doping of proton. However, the method of spontaneous growth of nanostructured PANi on electrospun fiber mats provides an effective method to produce porous electrically conducting electrospun fiber mats. The combination advantages of nanostructured PANi with the electrospun fiber mats, extends the applications of PANi and electrospun nanofibers, such as chemical- and bio-sensors, actuators, catalysis, electromagnetic shielding, corrosion protection, separation membranes, electro-optic devices, electrochromic devices, tissue engineering and many others.

The electrical conductivity of electrospun PCNM with PANi as the only conducting component is too low for application of as anode in microbial fuel cells (MFCs). So, we turn to electrospun carbon fiber due to its high electrical conductivity and environmental stability. The current density is greatly dependent on the microorganism density of anode in MFCs. While the two-dimensional electrospun

carbon fiber mat (2D-ECFM) which was prepared by normal electrospinning only allows growth of microorganism on the surface with thin layer owing to the low porosity and small pore size in the mat. With the concept of increasing the power density of MFCs by increase of microorganism density in the anode, two novel 3D electrospun carbon fiber mats, porous three-dimensional electrospun carbon fiber mat (3D-ECFM) and layered 3D-ECFM, were developed. The porous 3D-ECFM made by GE-spinning shows high specific surface area due to small fiber diameter of about 1μm, stable highly porous structure with high porosity of 99%, big pore size of around 5.8 μm in the mat and very low density of 18 $kg \cdot m^{-3}$. The porous 3D-ECFM anode is very suitable for microbial biofilms growth and generates very high geometric current density of 3.0 $mA \cdot cm^{-2}$, and super-high weight current density of 714 $mA \cdot g^{-1}$. The layered 3D-ECFM made by layer-by-layer electrospinning also shows high porosity of 98.5% which mainly come from the void-space between layers, and high specific area due to small electrospun carbon fibers on each layer. This layered design is suitable for layer-by-layer growth of biofilm and generates geometric current density of 2.0 $mA \cdot cm^{-2}$ and weight current density of 294 $mA \cdot g^{-1}$. Though the porosity and pore size in the mats are high enough for penetration single small microorganism, the tendency of biofilms formation makes the biofilm is unable to be grown in whole mat but only in the upper layer about several hundreds micrometers. Because the growth of biofilm is affected by multiple factors, e.g nutrition transfer, but they are greatly hindered by the biofilm formed in the upper layer. The current density of 3D-ECFM anode could be further improved by further increasing porosity and introducing large holes or channels in the mats for sufficient nutrition transportation to inside the mats.

According to the results of above, the porosity and the pore size in the fiber mat are utmost important for the performance of anode in MFCs. With concept of curve or helix in fibers can lead to higher porosity in the fiber mat, a novel 3D porous architecture, nanospring, was designed for high performance anode structure in future MFC. Polymeric nanospring was prepared by bicomponent electrospinning. The

reasons for the formation of polymeric nanosprings were investigated by coaxial electrospinning of bicomponent rigid i.e. Nomex® or polysulfonamide (PSA) (rigid) and flexible polymers i.e. thermoplastic polyurethane (TPU) (flexible). The results indicated that the nanospring formation is attributed to longitudinal compressive forces which are resulted from the different shrinkages of the rigid and flexible two polymer components and a good electrical conductivity of one of the polymer solutions in coaxial electrospinning system. The modified electrospinning i.e. off-centered electrospinning and side-by-side electrospinning are much more effective than the coaxial electrospinning for generating polymer spring or helical structures, because of the higher longitudinal compressive forces which derived from the lopsided elastic forces. The aligned nanofiber mat with high percent of nanospring shows higher elongation and higher storage modulus below transition glass temperature (T_g) compared to that with straight fibers. The nanospring or helical shape preserves much void-space in the mat. It would be a potential architecture for highly efficient anode in future MFCs.

References

[1] M. Rosenbaum, F. Zhao, U. Schröder, F. Scholz, *Angew Chem Int Edit* **2006**, *45*, 6658.

[2] B. E. Logan, *Microbial fuel cells* **2008**, *John Wiley & Sons, Inc*.

[3] B. E. Logan, *Nature Reviews Microbiology* **2009**, *7*, 375.

[4] B. E. L. a. J. M. Regan, *Trends Microbiol* **2006**.

[5] Andreas Greiner*, J. H. Wendorff*, *Angew Chem Int Edit* **2007**, *46*, 5670

[6] U. Schröder, *Phys Chem Chem Phys* **2007**, *9*, 2619.

[7] R. K. Thauer, K. Jungermann, K. Decker, *Bacteriol Rev* **1977**, *41*, 100.

[8] K. Rabaey, W. Verstraete, *Trends Biotechnol* **2005**, *23* 291.

[9] B. E. Logan, J. M. Regan, *Environ Sci Technol* **2006**, *40*, 5172.

[10] Z. W. Du, H. R. Li, T. Y. Gu, *Biotechnol Adv* **2007**, *25*, 464.

[11] U. Schröder, J. Niessen, F. Scholz, *Angew Chem Int Edit* **2003**, *42*, 2880.

[12] F. Zhao, F. Harnisch, U. Schröder, F. Scholz, P. Bogdanoff, I. Herrmann, *Electrochem Commun* **2005**, *7*, 1405.

[13] Z. He, L. T. Angenent, *Electroanal* **2006**, *18*, 2009.

[14] Hamid Rismani-Yazdia, Sarah M. Carverb, Ann D. Christya, Olli H. Tuovinenb,c, *J Power Sources* **2008,** *180*, 683.

[15] J. R. Kim, S. Cheng, S. E. Oh, B. E. Logan, *Environ Sci Technol* **2007**, *41*, 1004.

[16] B. E. Logan, J. M. Regan, *Trends Microbiol* **2006**, *14*, 512.

[17] T. Narihiro, Y. Sekiguchi, *Curr Opin Biotech* **2007**, *18*, 273.

[18] S. Agarwal, A. Greiner, J. H. Wendorff, *Adv Funct Mater* **2009**, *19*, 2863.

[19] S. Agarwal, J. H. Wendorff, A. Greiner, *Adv Mater* **2009**, *21*, 3343.

[20] K. Yoon, B. S. Hsiao, B. Chu, *J Mater Chem* **2008**, *18*, 5326.

[21] M. C. Potter, *Proceedings of the Royal Society of London Series B-Containing Papers of a Biological Character* **1911**, *84*, 260.

[22] D. R. Bond, D. E. Holmes, L. M. Tender, D. R. Lovley, *Science* **2002**, *295*, 483.

[23] K. Rabaey, W. Verstraete, *Trends Biotechnol* **2005**, *23*, 291.

[24] B. E. Logan, B. Hamelers, R. A. Rozendal, U. Schrorder, J. Keller, S. Freguia, P.

Aelterman, W. Verstraete, K. Rabaey, *Environ Sci Technol* **2006**, *40*, 5181.

[25] I. Roche, K. Katuri, K. Scott, *J Appl Electrochem* **2010**, *40*, 13.

[26] H. P. Bennetto, J. L. Stirling, K. Tanaka, C. A. Vega, *Biotechnol Bioeng* **1983**, *25*, 559.

[27] K. Tanaka, C. A. Vega, R. Tamamushi, *Bioelectroch Bioener* **1983**, *11*, 135.

[28] G. M. Delaney, H. P. Bennetto, J. R. Mason, S. D. Roller, J. L. Stirling, C. F. Thurston, *J Chem Tech Biot B* **1984**, *34*, 13.

[29] H. P. Bennetto, G. M. Delaney, J. R. Mason, S. D. Roller, J. L. Stirling, C. F. Thurston, *Biotechnol Lett* **1985**, *7*, 699.

[30] D. R. Lovley, *Ann Rev Microbiol* **1993**, *47*, 263.

[31] D. R. Lovley, *Trends in Ecol Evol* **1993**, *8*, 213.

[32] B. H. Kim, H. J. Kim, M. S. Hyun, D. H. Park, *J Microbiol Biotechn* **1999**, *9*, 127.

[33] S. K. Chaudhuri, D. R. Lovley, *Nat Biotechnol* **2003**, *21*, 1229.

[34] H. J. Kim, H. S. Park, M. S. Hyun, I. S. Chang, M. Kim, B. H. Kim, *Enzyme Microb Tech* **2002**, *30*, 145.

[35] D. R. Bond, D. R. Lovley, *Appl Environ Microb* **2003**, *69*, 1548.

[36] B. Min, J. R. Kim, S. E. Oh, J. M. Regan, B. E. Logan, *Water Res* **2005**, *39*, 4961.

[37] F. Scholz, U. Schröder, *Nat Biotechnol* **2003**, *21*, 1151.

[38] H. Liu, S. A. Cheng, B. E. Logan, *Environ Sci Technol* **2005**, *39*, 658.

[39] K. Rabaey, N. Boon, M. Hofte, W. Verstraete, *Environ Sci Technol* **2005**, *39*, 3401.

[40] D. R. Bond, D. R. Lovley, *Appl Environ Microb* **2005**, *71*, 2186.

[41] G. Reguera, K. D. McCarthy, T. Mehta, J. S. Nicoll, M. T. Tuominen, D. R. Lovley, *Nature* **2005**, *435*, 1098.

[42] G. Reguera, K. P. Nevin, J. S. Nicoll, S. F. Covalla, T. L. Woodard, D. R. Lovley, *Appl Environ Microb* **2006**, *72*, 7345.

[43] S. D. Roller, H. P. Bennetto, G. M. Delaney, J. R. Mason, J. L. Stirling, C. F. Thurston, *J Chem Tech Biot B* **1984**, *34*, 3.

[44] D. H. Park, J. G. Zeikus, *Appl Environ Microb* **2000**, *66*, 1292.

[45] J. L. Stirling, H. P. Bennetto, G. M. Delaney, J. R. Mason, S. D. Roller, K. Tanaka, C. F. Thurston, *Biochem Soc T* **1983**, *11*, 451.

[46] R. A. Bullen, T. C. Arnot, J. B. Lakeman, F. C. Walsh, *Biosens Bioelectron* **2006**, *21*, 2015.

[47] F. A. M. d. B. Alfons J. M. Stams, M. H. A. v. E. Caroline M. Plugge, Jan Dolfing and Gosse Schraa, *Environ Microbiol* **2006**, *8*, 371.

[48] K. Rabaey, N. Boon, S. D. Siciliano, M. Verhaege, W. Verstraete, *Appl Environ Microb* **2004**, *70*, 5373.

[49] K. Rabaey, P. Clauwaert, P. Aelterman, W. Verstraete, *Environ Sci Technol* **2005**, *39*, 8077.

[50] J. Niessen, U. Schröder, M. Rosenbaum, F. Scholz, *Electrochem Commun* **2004**, *6*, 571.

[51] J. Niessen, U. Schröder, F. Scholz, *Electrochem Commun* **2004**, *6*, 955.

[52] J. Niessen, U. Schröder, F. Harnisch, F. Scholz, *Lett Appl Microbiol* **2005**, *41*, 286.

[53] H. Liu, S. Grot, B. E. Logan, *Environ Sci Technol* **2005**, *39*, 4317.

[54] Y. Liu, F. Harnisch, K. Fricke, R. Sietmann, U. Schröder, *Biosens Bioelectron* **2008**, *24*, 1006.

[55] H. Moon, I. S. Chang, B. H. Kim, *Bioresource Technol* **2006**, *97*, 621.

[56] Z. He, S. D. Minteer, L. T. Angenent, *Environ Sci Technol* **2005**, *39*, 5262.

[57] H. Liu, R. Ramnarayanan, B. E. Logan, *Environ Sci Technol* **2004**, *38*, 2281.

[58] S. E. Oh, J. Kim, B. Min, B. E. Logan, *Abstr Pap Am Chem S* **2005**, *230*, U1691.

[59] Y. Zuo, P. C. Maness, B. E. Logan, *Energ Fuel* **2006**, *20*, 1716.

[60] J. R. Kim, B. Min, B. E. Logan, *Appl Microbiol Biot* **2005**, *68*, 23.

[61] E. Lalaurette, S. Thammannagowda, A. Mohagheghi, P. C. Maness, B. E. Logan, *Int J Hydrogen Energ* **2009**, *34*, 6201.

[62] R. A. Rozendal, H. V. M. Hamelers, G. J. W. Euverink, S. J. Metz, C. J. N. Buisman, *Int J Hydrogen Energ* **2006**, *31*, 1632.

[63] K. Rabaey, G. Lissens, S. D. Siciliano, W. Verstraete, *Biotechnol Lett* **2003**, *25*, 1531.

[64] M. Rosenbaum, U. Schröder, F. Scholz, *J Solid State Electr* **2006**, *10*, 872.

[65] I. S. Chang, J. K. Jang, G. C. Gil, M. Kim, H. J. Kim, B. W. Cho, B. H. Kim, *Biosens Bioelectron* **2004**, *19*, 607.

[66] I. S. Chang, H. Moon, J. K. Jang, B. H. Kim, *Biosens Bioelectron* **2005**, *20*, 1856.

[67] B. H. Kim, I. S. Chang, G. C. Gil, H. S. Park, H. J. Kim, *Biotechnol Lett* **2003**, *25*, 541.

[68] H. Moon, I. S. Chang, K. H. Kang, J. K. Jang, B. H. Kim, *Biotechnol Lett* **2004**, *26*, 1717.

[69] A. Bergel, D. Feron, A. Mollica, *Electrochem Commun* **2005**, *7*, 900.

[70] K. B. Gregory, D. R. Lovley, *Environ Sci Technol* **2005**, *39*, 8943.

[71] K. B. Gregory, D. Bond, D. R. Lovley, *Abstr Pap Am Chem S* **2004**, *228*, U638.

[72] L. M. Tender, C. E. Reimers, H. A. Stecher, D. E. Holmes, D. R. Bond, D. A. Lowy, K. Pilobello, S. J. Fertig, D. R. Lovley, *Nat Biotechnol* **2002**, *20*, 821.

[73] C. E. Reimers, P. Girguis, H. A. Stecher, L. M. Tender, N. Ryckelynck, P. Whaling, *Geobiology* **2006**, *4*, 123.

[74] C. B. Huang, S. L. Chen, C. L. Lai, D. H. Reneker, H. Qiu, Y. Ye, H. Q. Hou, *Nanotechnology* **2006**, *17*, 1558.

[75] Zheng-Ming Huang, Y.-Z. Zhang, M. Kotakic, S. Ramakrishnab, *Compos Sci Technol* **2003**, *63*, 2223.

[76] B. S. H. Christian Burger, and Benjamin Chu, *Annu Rev Mater Res* **2006**, *36*, 333.

[77] S. Agarwal, J. H. Wendorff, A. Greiner, *Polymer* **2008**, *49*, 5603.

[78] F. Ko, Y. Gogotsi, A. Ali, N. Naguib, H. H. Ye, G. L. Yang, C. Li, P. Willis, *Adv Mater* **2003**, *15*, 1161.

[79] H. S. K. Jun Hee Sung, Hyoung-Joon Jin,* Hyoung Jin Choi, and In-Joo Chin, *Macromolecules* **2004**, *37*, 9899.

[80] J. J. Ge, H. Q. Hou, Q. Li, M. J. Graham, A. Greiner, D. H. Reneker, F. W. Harris, S. Z. D. Cheng, *J Am Chem Soc* **2004**, *126*, 15754.

[81] W. Salalha, J. Kuhn, Y. Dror, E. Zussman, *Nanotechnology* **2006**, *17*, 4675.

[82] M. Gensheimer, M. Becker, A. Brandis-Heep, J. H. Wendorff, R. K. Thauer, A.

Greiner, *Adv Mater* **2007**, *19*, 2480.

[83] S. W. Lee, A. M. Belcher, *Nano Letters* **2004**, *4*, 387.

[84] S. V. F. J. H. Yu, G. C. Rutledge, *Adv Mater* **2004**, *16*, 1562

[85] M. Wang, J. H. Yu, D. L. Kaplan, G. C. Rutledge, *Macromolecules* **2006**, *39*, 1102.

[86] Dan Li, Yuliang Wang, Y. Xia*, *Nano Lett* **2003**, *3*, 1167.

[87] M. B. Michael Bognitzki, Martin Graeser, Werner Massa, Joachim H. Wendorff,, D. W. Andreas Schaper, Andre Beyer, Armin Gölzhäuser, and Andreas Greiner*, *Adv Mater* **2006**, *18*, 2384.

[88] Dan Li, Y. Xia*, *Nano Lett* **2003**, *3*, 555.

[89] A. L. Y. Eyal Zussman, Alexander V. Bazilevsky, Ron Avrahami, Michael Feldman, *Adv Mater* **2006**, *18*, 348.

[90] Dan Li, Y. Xia*, *Nano Lett* **2004**, *4*, 933.

[91] E. Smit, U. Buttner, R. D. Sanderson, *Polymer* **2005**, *46*, 2419.

[92] X. F. Wang, K. Zhang, M. F. Zhu, H. Yu, Z. Zhou, Y. M. Chen, B. S. Hsiao, *Polymer* **2008**, *49*, 2755.

[93] M. S. Khil, S. R. Bhattarai, H. Y. Kim, S. Z. Kim, K. H. Lee, *J Biomed Mater Res B* **2005**, *72B*, 117.

[94] J. Rafique, J. Yu, J. Yu, G. Fang, K. W. Wong, Z. Zheng, H. C. Ong, W. M. Lau, *Appl Phys Lett* **2007**, *91*, 063126.

[95] J. A. Matthews, G. E. Wnek, D. G. Simpson, G. L. Bowlin, *Biomacromolecules* **2002**, *3*, 232.

[96] P. Katta, M. Alessandro, R. D. Ramsier, G. G. Chase, *Nano Letters* **2004**, *4*, 2215.

[97] C. B. Huang, S. L. Chen, D. H. Reneker, C. L. Lai, H. Q. Hou, *Adv Mater* **2006**, *18*, 668.

[98] S. L. Chen, P. Hu, A. Greiner, C. Y. Cheng, H. F. Cheng, F. F. Chen, H. Q. Hou, *Nanotechnology* **2008**, *19*.

[99] D. Li, Y. L. Wang, Y. N. Xia, *Adv Mater* **2004**, *16*, 361.

[100] D. Y. Yang, B. Lu, Y. Zhao, X. Y. Jiang, *Adv Mater* **2007**, *19*, 3702.

[101] D. M. Zhang, J. Chang, *Adv Mater* **2007**, *19*, 3664.

[102] J. Stitzel, L. Liu, S. J. Lee, M. Komura, J. Berry, S. Soker, G. Lim, M. Van Dyke, R. Czerw, J. J. Yoo, A. Atala, *Biomaterials* **2006**, *27*, 1088.

[103] W. E. Teo, M. Kotaki, X. M. Mo, S. Ramakrishna, *Nanotechnology* **2005**, *16*, 918.

[104] J. W. Xie, X. R. Li, Y. N. Xia, *Macromol Rapid Commun* **2008**, *29*, 1775.

[105] V. Thavasi, G. Singh, S. Ramakrishna, *Energ Environ Sci* **2008**, *1*, 205.

[106] K. Yoon, K. Kim, X. F. Wang, D. F. Fang, B. S. Hsiao, B. Chu, *Polymer* **2006**, *47*, 2434.

[107] R. Gopal, S. Kaur, Z. W. Ma, C. Chan, S. Ramakrishna, T. Matsuura, *J Membrane Sci* **2006**, *281*, 581.

[108] K. P. Rajesh, T. S. Natarajan, *J Nanosci Nanotechnol* **2009**, *9*, 5402.

[109] I. D. Kim, J. M. Hong, B. H. Lee, D. Y. Kim, E. K. Jeon, D. K. Choi, D. J. Yang, *Appl Phys Lett* **2007**, *91*.

[110] R. Jose, A. Kumar, V. Thavasi, S. Ramakrishna, *Nanotechnology* **2008**, *19*.

[111] K. Mukherjee, T. H. Teng, R. Jose, S. Ramakrishna, *Appl Phys Lett* **2009**, *95*.

[112] H. J. Kim, Y. S. Kim, M. H. Seo, S. M. Choi, W. B. Kim, *Electrochem Commun* **2009**, *11*, 446.

[113] C. Kim, K. S. Yang, M. Kojima, K. Yoshida, Y. J. Kim, Y. A. Kim, M. Endo, *Adv Funct Mater* **2006**, *16*, 2393.

[114] Y. Yu, L. Gu, C. B. Zhu, P. A. van Aken, J. Maier, *J Am Chem Soc* **2009**, *131*, 15984.

[115] L. W. Ji, X. W. Zhang, *Nanotechnology* **2009**, *20*.

[116] C. Kim, K. S. Yang, W. J. Lee, *Electrochem Solid St* **2004**, *7*, A397.

[117] C. Kim, K. S. Yang, *Appl Phys Lett* **2003**, *83*, 1216.

[118] C. Kim, J. S. Kim, S. J. Kim, W. J. Lee, K. S. Yang, *J Electrochem Soc* **2004**, *151*, A769.

[119] C. Kim, B. T. N. Ngoc, K. S. Yang, M. Kojima, Y. A. Kim, Y. J. Kim, M. Endo, S. C. Yang, *Adv Mater* **2007**, *19*, 2341.

[120] D. K. Kim, S. H. Park, B. C. Kim, B. D. Chin, S. M. Jo, D. Y. Kim, *Macromol Res* **2005**, *13*, 521.

[121] J. S. Im, S. J. Park, T. Kim, Y. S. Lee, *Int J Hydrogen Energ* **2009**, *34*, 3382.

[122] H. W. Tong, M. Wang, *J Nanosci Nanotechnol* **2007**, *7*, 3834.

[123] A. J. Meinel, K. E. Kubow, E. Klotzsch, M. Garcia-Fuentes, M. L. Smith, V. Vogel, H. P. Merkle, L. Meinel, *Biomaterials* **2009**, *30*, 3058.

[124] F. Spano, M. Liley, C. Hinderling, H. Sigrist, *Tissue Engineering Part A* **2008**, *14*, 922.

[125] L. A. Smith, X. H. Liu, P. X. Ma, *Soft Matter* **2008**, *4*, 2144.

[126] Z. Jing, X. Y. Xu, X. S. Chen, Q. Z. Liang, X. C. Bian, L. X. Yang, X. B. Jing, *J Control Release* **2003**, *92*, 227.

[127] G. Verreck, I. Chun, J. Rosenblatt, J. Peeters, A. Van Dijck, J. Mensch, M. Noppe, M. E. Brewster, *J Control Release* **2003**, *92*, 349.

[128] M. R. Abidian, D. H. Kim, D. C. Martin, *Adv Mater* **2006**, *18*, 405.

[129] P. Taepaiboon, U. Rungsardthong, P. Supaphol, *Nanotechnology* **2006**, *17*, 2317.

[130] O. Hartman, C. Zhang, E. L. Adams, M. C. Farach-Carson, N. J. Petrelli, B. D. Chase, J. F. Rabolt, *Biomacromolecules* **2009**, *10*, 2019.

[131] M. M. H. Y. M. Shin, M. P. Brenner, G. C. Rutledgea, *Appl. Phys. Lett.* **2001**, *78*, 1149.

[132] D. H. Reneker, A. L. Yarin, H. F. a. S. Koombhongse, *J. Appl. Phys.* **2000**, *87*, 4531.

[133] S. K. a. D. H. R. A. L. Yarin, *J Appl Phys* **2001**, *89*, 3018.

[134] S. N. Reznik, A. L. Yarin, E. Zussman, L. Bercovici, *Phys Fluids* **2006**, *18*, 062101

[135] W. S. Y. Dror, R. Avrahami, E. Zussman,* A. L. Yarin, R. Dersch, A. Greiner, and J. H. Wendorff, *Small* **2007**, *3*, 1064.

[136] Z. Sun, E. Zussman, A. L. Yarin, J. H. Wedorff, and A. Greiner, *Adv. Mater.* **2003**, *15*, 1929.

[137] R. V.-O. Gustavo Larsen, Kevin Minchow, Antonio Barrero, Ignacio G. Loscertales*, *J Am Chem Soc* **2003**, *125*, 1154.

[138] Dan Li, Jesse T. McCann, a. Y. Xia*, *Small* **2005**, *1*, 83

[139] N. J. Miao Wang, Chin B. Su, and Jun Kameokaa┌, C.-K. C. a. M.-C. Hung,

K.-A. Chang, *Appl Phys Lett* **2006**, *88*, 033106.

[140] S. R. a. V.-O. R. Larsen G, *Adv Mater* **2004**, *16*, 166.

[141] D. F. In Chul Um, Benjamin S. Hsiao, Akio Okamoto, and Benjamin Chu*, *Biomacromolecules* **2004**, *5*, *1428*.

[142] Xuefen Wanga, In Chul Uma, Dufei Fang, Akio Okamoto, Benjamin S. Hsiao, B. Chu*, *Polymer* **2005**, *46*, 4853.

[143] H. Hou, S. Chen, C. Cheng, P. Hu., *Chinese patent* CN20071009595 20070925

[144] S. Madhugiri, A. Dalton, J. Gutierrez, J. P. Ferraris, K. J. Balkus, *J Am Chem Soc* **2003**, *125*, 14531.

[145] H. W. Tong Lin, and Xungai Wang, *Adv Mater* **2005**, *17*, 2699.

[146] S. L. Chen, H. Q. Hou, P. Hu, J. H. Wendorff, A. Greiner, S. Agarwal, *Macromol Mater Eng* **2009**, *294*, 781.

[147] M. Lallave, J. Bedia, R. Ruiz-Rosas, J. Rodriguez-Mirasol, T. Cordero, J. C. Otero, M. Marquez, A. Barrero, I. G. Loscertales, *Adv Mater* **2007**, *19*, 4292.

[148] X. C. Yong Zhao, and Lei Jiang*, *J Am Chem Soc* **2007**, *129*, 764

[149] S. A. Theron, A. L. Yarin, E. Zussman, E. Kroll, *Polymer* **2005**, *46*, 2889.

[150] A.L. Yarin*, E. Zussman, *Polymer* **2004**, *45*, 2977.

[151] O. O. Dosunmu, G.G. Chase, WKataphinan, a. D. H. Reneker, *Nanotechnology* **2006**, *17*, 1123.

[152] Yanzhong Zhang, Zheng-Ming Huang, Xiaojing Xu, Chwee Teck Lim, a. S. Ramakrishna, *Chem Mater* **2004**, *16*, 3406.

[153] Y. Zhao, X. Y. Cao, L. Jiang, *J Am Chem Soc* **2007**, *129*, 764.

[154] G. Kim, Y. S. Cho, W. D. Kim, *Eur Polym J* **2006**, *42*, 2031.

[155] H. Y. Mi, X. G. Zhang, S. D. Yang, X. G. Ye, J. M. Luo, *Mater Chem Phys* **2008**, *112*, 127.

[156] L. Z. Fan, Y. S. Hu, J. Maier, P. Adelhelm, B. Smarsly, M. Antonietti, *Adv Funct Mater* **2007**, *17*, 3083.

[157] J. X. Huang, S. Virji, B. H. Weiller, R. B. Kaner, *J Am Chem Soc* **2003**, *125*, 314.

[158] S. Virji, J. X. Huang, R. B. Kaner, B. H. Weiller, *Nano Lett* **2004**, *4*, 491.

[159] J. Huang. D. Li, R. B. Kaner, *Accounts Chem Res* **2008**, *42*, 135.

[160] E. Smela, *Adv Mater* **2003**, *15*, 481.

[161] G. Inzelt, *Conducting polymers* **2008**, *p 225* Springer

[162] M. Y. Li, Y. Guo, Y. Wei, A. G. MacDiarmid, P. I. Lelkes, *Biomaterials* **2006**, *27*, 2705.

[163] G. Wang, Z. K. Tan, X. Q. Liu, S. Chawda, J. S. Koo, V. Samuilov, M. Dudley, *Nanotechnology* **2006**, *17*, 5829.

[164] I. S. Chronakis, S. Grapenson, A. Jakob, *Polymer* **2006**, *47*, 1597.

[165] M. K. Shin, Y. J. Kim, S. I. Kim, S. K. Kim, H. Lee, G. M. Spinks, S. J. Kim, *Sensors Actuat B-Chem* **2008**, *134*, 122.

[166] M. Kang, H. J. Jin, *Colloid Polym Sci* **2007**, *285*, 1163.

[167] S. Nair, E. Hsiao, S. H. Kim, *J Mater Chem* **2008**, *18*, 5155.

[168] E. T. Kang, K. G. Neoh, K. L. Tan, *Prog Polym Sci* **1998**, *23*, 277.

[169] X. Y. Zhang, W. J. Goux, S. K. Manohar, *J Am Chem Soc* **2004**, *126*, 4502.

[170] W. G. Li, H. L. Wang, *J Am Chem Soc* **2004**, *126*, 2278.

[171] X. Y. Zhang, S. K. Manohar, *Chem Commun* **2004**, 2360.

[172] J. X. Huang, R. B. Kaner, *Chem Commun* **2006**, 367.

[173] M. X. Wan, *Adv Mater* **2008**, *20*, 2926.

[174] H. K. Chaudhari, D. S. Kelkar, *J Appl Polym Sci* **1996**, *62*, 15.

[175] L. Liang, J. Liu, C. F. Windisch, G. J. Exarhos, Y. H. Lin, *Angew Chem Int Edit* **2002**, *41*, 3665.

[176] J. X. Huang, R. B. Kaner, *Angew Chem Int Edit* **2004**, *43*, 5817.

[177] H. J. Ding, M. X. Wan, Y. Wei, *Adv Mater* **2007**, *19*, 465.

[178] N. R. Chiou, A. J. Epstein, *Adv Mater* **2005**, *17*, 1679.

[179] N.-R. Chiou, C. Lu, J Guan, L. J. Lee, A. J. Epstein, *Nat Nanotechnol,* **2007**, *2*, 354.

[180] Y. Qiao, S. J. Bao, C. M. Li, X. Q. Cui, Z. S. Lu, J. Guo, *Acs Nano* **2008**, *2*, 113.

[181] P. Stoodley, K. Sauer, D. G. Davies, J. W. Costerton, *Ann Rev Microbiol* **2002**, *56*, 187.

[182] K. R. Stefano Freguia 1, Zhiguo Yuan 3, J¨urg Keller, *Electrochim Acta* **2007**,

53 , 598–603 (2007).

[183] D. R. Lovley, *Nat Rev Microbiol* **2006**, *4*, 497.

[184] Y. A. Gorby, S. Yanina, J. S. McLean, K. M. Rosso, D. Moyles, A. Dohnalkova, T. J. Beveridge, I. S. Chang, B. H. Kim, K. S. Kim, D. E. Culley, S. B. Reed, M. F. Romine, D. A. Saffarini, E. A. Hill, L. Shi, D. A. Elias, D. W. Kennedy, G. Pinchuk, K. Watanabe, S. i. Ishii, B. Logan, K. H. Nealson, J. K. Fredrickson, *PNAS* **2006**, *103*, 11358.

[185] B. E. Logan, *Nat Rev Microbiol* **2009**, *7*, 375.381.

[186] C. I. Torres, A. K. Marcus, H. S. Lee, P. Parameswaran, R. Krajmalnik-Brown, B. E. Rittmann, *Fems Microbiol Rev* **2010**, *34*, 3.

[187] C. E. Reimers, L. M. Tender, S. Fertig, W. Wang, *Environ Sci Technol* **2001**, *35*, 192.

[188] C. Donovan, A. Dewan, D. Heo, H. Beyenal, *Environ Sci Technol* **2008**, *42*, 8591.

[189] U. Schroder, *Chemsuschem* **2008**, *1*, 281.

[190] J. Ditzig, H. Liu, B. E. Logan, *Int J Hydrogen Energ* **2007**, *32*, 2296.

[191] M. Adachi, T. Shimomura, M. Komatsu, H. Yakuwa, A. Miya, *Chem Commun* **2008**, 2055.

[192] T. Zhang, Y. L. Zeng, S. L. Chen, X. P. Ai, H. X. Yang, *Electrochem Commun* **2007**, *9*, 349.

[193] Y. Qiao, C. M. Li, S. J. Bao, Q. L. Bao, *J Power Sources* **2007**, *170*, 79.

[194] C. I. Torres, A. K. Marcus, H. S. Lee, R. Krajmalnik-Brown, B. E. Rittmann, *FEMS Microbiol Rev* **2010**, *34*, 3.

[195] B. Logan, S. Cheng, V. Watson, G. Estadt, *Environ Sci Technol* **2007**, *41*, 3341.

[196] M. Rosenbaum, F. Zhao, U. Schröder, F. Scholz, *Angew Chem Int Ed* **2006** *45*, 6658.

[197] R. Dersch, T. Q. Liu, A. K. Schaper, A. Greiner, J. H. Wendorff, *J Polym Sci Polym Chem* **2003**, *41*, 545.

[198] M. M. Hohman, M. Shin, G. Rutledge, M. P. Brennera), *Phys Fluids* **2001**, *13*, 2201.

[199] M. M. Hohman, M. Shin, G. Rutledge, M. P. Brennera, *Phys Fluids* **2001**, *13*, 2221.

[200] S. CHIU-WEBSTER, J. R. LISTER, *J Fluid Mech* **2006**, *569*.

[201] Tao Han , Darrell H. Reneker, A. L. Y. b, *Polymer* **2007**, *48*, 6064.

[202] G. T. Royal Kessick, *Appl Phys Lett* **2004**, *84*, 4807.

[203] P. Gupta, G. L. Wilkes, *Polymer* **2003**, *44*, 6353.

[204] D. R. Lovley, R. C. Greening, J. G. Ferry, *Appl Environ Microb* **1984**, *48*, 81.

[205] W. E. Balch, G. E. Fox, L. J. Magrum, C. R. Woese, R. S. Wolfe, *Microbiol Rev* **1979**, *43*, 260.

[206] D'Arcy, J.B., Sheep and Wool Technology, *NSW University Press*, Kensington, **1986**

[207] http://en.wikipedia.org/wiki/Wool

Acknowledgements

First and foremost, I would like to express my sincere gratitude to my direct supervisor Prof. Dr. Andreas Greiner for support my doctor study and giving me interesting topic. Under his constant encouragement and guidance, I can finish my work smoothly.

I would also like to thank PD Dr. Seema Agarwal for her enlightening lectures and giving so much good advice on my work.

I want to give thanks to Porf. Dr. Haoqing Hou in the Department of Chemistry of Jiangxi Normal University, thanks for recommending me to Prof. Dr. Andreas Greiner and close cooperation on 3D electrospun fiber mats and his constructive advice.

I am deeply grateful for Prof. Dr. Uwe Schröder, for his close cooperation and so much good advice on MFCs research. And I also want to give thanks to his group members, especially, Dr. Falk Harnisch, Sunil Patil and Alessandro Alfredo Carmona-Martinez, for giving me so much help during the stay in Braunschweig and helping me measuring the performance of anode materials.

I would like to thank Prof. Dr. Joachim H. Wendorff for providing the working place in the first year and so many good instruments for my work. And also thank his group members for the friendly working atmosphere.

I also appreciate Fei Chen, Rimpu Kumar and Dr. Roland Dersch for helping me correct my Ph.D thesis patiently and giving constructive suggestions on my thesis.

I owe much to our group members for giving me help during my doctor work.

First thanks go to Ana Bier for her kindly ordering and searching chemicals for me, as well as Martina Gerlach and Uwe Justus.

I am very grateful for secretary of our group Mrs Schmidt for helping a lot on documents.

Very thankful for Marco Gensheimer for giving helps on handling and culture of bacteria and giving advice on bacterial compatibility measurements.

Thanks Carsten Sinkel for solving the computer and network problems

Thank Michael Hellwig and Dr. Andreas Schaper for helping me the electron microscope measurements.

My sincere thanks are also given to the members of two mechanical workshops, and electronic workshop for processing so many nice equipments for my work.

Last but not the least, my gratitude also extends to my family who have been assisting, supporting and caring for me, especially my wife who sacrifices so much for my doctor work, and my son who brings us so much happiness.

Erklärung

ich versichere, daß ich meine Dissertation

selbständig, ohne unerlaubte Hilfe angefertigt und mich dabei keiner anderen als der von mir ausdrücklich bezeichneten Quellen und Hilfen bedient habe.

Die Dissertation wurde in der jetzigen order einer ähnlichen Form noch bei keiner anderen Hochschule eingereicht und hat noch keinen sonstigen Prüfungszwecken gedient.

(ort/Datum) (Unterschrift mit Vor- und Zuname)